2014

Semiconductor nanocrystals for novel optical applications

Jong-Sik Moon

Department: Chemistry

SEMICONDUCTOR NANOCRYSTALS

FOR NOVEL OPTICAL APPLICATIONS

by

JONG-SIK MOON

A DISSERTATION

Presented to the Graduate Faculty of the

MISSOURI UNIVERSITY OF SCIENCE AND TECHNOLOGY

In Partial Fulfillment of the Requirements for the Degree

DOCTOR OF PHILOSOPHY

in

CHEMISTRY

2014

Approved by:

Jeffrey G. Winiarz, Advisor
Yue-wern Huang
Yinfa Ma
Manashi Nath
Klaus Woelk

PUBLICATION DISSERTATION OPTION

This dissertation has been prepared in the style utilized of the following five articles that have been published, or submitted for publication as follows:

Pages 35-66 submitted in Journal of Chemical Physics, 2014.

Pages 67-108 will be submitted for publication in Journal of American Chemical Society.

Pages 109–126 will be submitted for publication in Journal of Physical Chemistry, Part B.

Pages 127-157 published in Colloids and Surfaces B: Biointerfaces, 2013, 111, 162–170.

Pages 158-184 published in BioMedical Research International, 2014, 2014.

ABSTRACT

Inspired by the promise of enhanced spectral response, photorefractive polymeric composites photosensitized with semiconductor nanocrystals have emerged as an important class of materials. Here, we report on the photosensitization of photorefractive polymeric composites at visible wavelengths through the inclusion of narrow band-gap semiconductor nanocrystals composed of PbS. Through this approach, internal diffraction efficiencies in excess of 82%, two-beam-coupling gain coefficients in excess of 211 cm^{-1}, and response times 34 ms have been observed, representing some of the best figures-of-merit reported on this class of materials. In addition to providing efficient photosensitization, however, extensive studies of these hybrid composites have indicated that the inclusion of nanocrystals also provides an enhancement in the charge-carrier mobility and subsequent reduction in the photorefractive response time. Through this approach with PbS as charge-carrier, unprecedented response times of 399 μs were observed, opening the door for video and other high-speed applications. It is further demonstrated that this improvement in response time occurs with little sacrifice in photorefractive efficiency and with internal diffraction efficiencies of 72% and two-beam-coupling gain coefficients of 500 cm^{-1} being measured. A thorough analysis of the experimental data is presented, supporting the hypothesized mechanism of the enhanced charge mobility without the accompaniment of superfluous traps. Finally, water soluble InP/ZnS and CdSe/ZnS quantum dots interacted with CPP and Herceptin to apply them as a bio-maker. Both of quantum dots showed the excellent potential for use in biomedical imaging and drug delivery applications. It is anticipated that these approaches can play a significant role in the eventual commercialization of these classes of materials.

ACKNOWLEDGMENTS

This dissertation would never have been completed without support, guidance, and encouragement from my advisor, Dr. Jeffrey G. Winiarz. He was not only the best adviser but also the best friend. He was a mentor and a guardian for my new life in United States. There are no words to express my sincere appreciation for him**.**

I would also like to thank my committee members, Dr. Yinfa Ma, Dr. Manashi Nath, Dr. Klaus Woelk, and Dr. Yue-wern Huang for their advice. I'm grateful for the financial support from the Materials Research Center, Department of Chemistry and Missouri University of Science and Technology. Moreover, I truly appreciate the people at Sandia National Laboratory, Tyler E. Stevens, Dr. Todd C. Monson, and Dr. Dale L. Huber in New Mexico for providing PbS Q-dots for this research.

I truly value the cooperation of my former and present fellow graduate students, Naveen Lingam, Yichen Liang, and Tyler Fears for their kind help and support. My gratitude extends to all undergraduate students, Kelsey Bass, Jessica Walker, Weston Bowen, Sonia Franz, Banjamin D. Mahala, and Patrick A. Martin who worked with me.

Finally, I really appreciate the support, encouragement and endless love given by my family. My wife Hyojung's love, unlimited support and encouragement always guided me in my success. I also thank my parents, sister, brothers-in-law, and mother-in-law for their love, encouragement, and sacrifices, without their support what I have achieved so far would not be possible.

TABLE OF CONTENTS

LIST OF ILLUSTRATIONS

Figure Page

LIST OF TABLES

SECTION

1. INTRODUCTION

1.1. PHOTOCONDUCTIVITY

Photoconductive (PC) materials become more electrically conductive upon absorption of electromagnetic radiation [1]. When a PC material such as a semiconductor (silica, selenium, or lead sulfide) absorbs a photon with sufficient energy to excite an electron from the valence band to the conduction band, or in other words, overcome the band-gap energy, E_g, an increase in electrical conductivity will occur [2]. Therefore the spectral sensitivity of PC material depends on the E_g of the material. For example, some of the semiconductor quantum-dots (Q-dots) used in this study, composed of PbS, had E_g ~1.02 eV corresponding a wavelength of ~1200 nm.

Polymeric PC materials are of interest due to their ease and flexibility of fabrication as well as the possibility of modifying their optical properties. The vast majority of organic PC materials described in literature use poly(*N*-vinylcarbazole) (PVK), shown in Fig. 1.1, due to its efficient hole-transporting capability [3]. More recently, triphenyldiamine (TPD), as well as its derivations, also shown in Fig. 1.1, have recently come into prevalence due their improved PCs [4-8].

Most organic PC materials have low absorption in the visible and NIR and therefore it is customary to dope the material with a photosensitizing species for the purposes of photo-charge generation. The most widely used photosensitizer is C_{60}, also known as

buckminsterfullerene, and shown in Fig. 1.1. C_{60} is an efficient charge generator because of its excellent electron accepting properties [9-12].

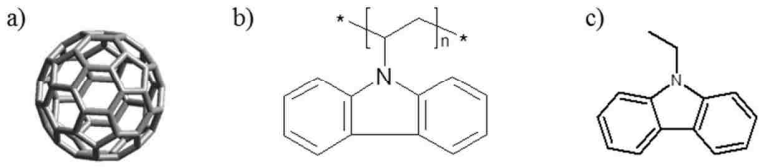

Figure 1.1. Structure of a) C_{60}, b) PVK, and c) ECZ.

Figure 1.2 schematically depicts the charge generation process. Here, the absorption of a photon initiates the process by exciting an electron from the highest occupied molecular orbital (HOMO) to the lowest unoccupied molecular orbital (LUMO) of the photosensitizer. Subsequently, the photosensitizer is reduced by the transfer of an electron from the HOMO of the charge-transporting PC matrix to the HOMO of the photosensitizer. The hole which now resides in the HOMO of the charge-transporting PC matrix may contribute to the photo-current.

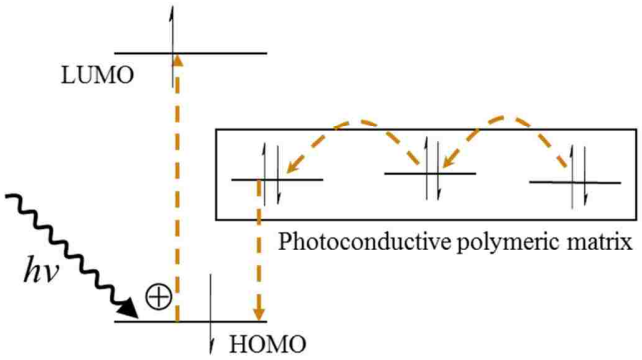

Figure 1.2. Charge-generation and subsequent transfer to charge-transport matrix.

Despite the promising aspects associated with C_{60}, several limitations persist. The loading content of C_{60} is constrained by the propensity for phase separation. Moreover, the lack of tunability in operating wavelength of C_{60} also limits further application. In an effort to overcome these limitations, Q-dots such as CdS, HgS, PbS, and CdSe have been investigated for their function as photosensitizers [13-16]. Photosensitizing with Q-dots has numerous advantages, perhaps the most appealing is the ability to readily manipulate the spectral features of Q-dots through quantum confinement effects, and therefore the operational wavelength, λ, of the composite into which they are doped [16-19]. Control over the optical and electrical properties of the Q-dots originates from the inverse correlation between the E_g and the physical dimension of the Q-dots. This inverse relationship translates into a blue-shift in the absorption spectrum of a given material as its proportions are decreased beyond the dimensions of the average distance from electron to proton (generally in hydrogen atom, Bohr radius) by quantum confinement effect. In addition, Q-dots are considerably smaller than the wavelengths associated with visible light; and as such, their inclusion does not adversely affect the optical quality of the PR composite [20].

1.2. PHOTOREFRACTIVITY

In 1990, PC materials found their first usage in the application of photorefractivity (PR). The PR effect is especially interesting in polymeric systems for applications including optical data storage, optical amplification, and dynamic image processing [1, 2, 21-23].

1.2.1. Photorefractive Theory. The PR effect is a spatial modulation of the refractive index, *n*, induced by non-uniform illumination followed by the formation of the space-charge field, E_{SC} [1, 24]. PR holograms are dynamic, which means they can be erased by uniform illumination, or rewritten by changing the illumination pattern. This dynamic nature distinguishes PR holography from the other holographic techniques [1]. The PR effect depends on two distinct processes, the formation of the internal E_{SC} and the modulation of the *n* [3].

The formation of the E_{SC} can be further sub-divided into three processes; 1) photocharge generation, 2) charge transport and 3) charge trapping. In PR composites, the photocharge generation is typically accomplished through the inclusion of the photosensitizer which is responsive at the wavelength of interest. Charge transport is accomplished through the inclusion of the photoconducting polymer or molecular species. Here, photogenerated charges are transported by a drift dominated mechanism within the externally applied electric field, *E* [2]. Charge trapping is usually accomplished without any additive, relying on oxidative impurities as well as imperfections in the sample.

Modulation of the *n* is typically accomplished through the inclusion of the nonlinear optical (NLO) chromophore or dye (named as such due to their typically deeply colored nature). The nonlinearity may be the result of linear Pockels effect but the birefringence of the chromophore is typically provides a more significant contribution. Therefore, the resulting E_{SC} modulates the *n* via the linear Pockels effect and/or birefringence and creates a holographic diffraction grating. It is notable that because each functionality is fulfilled through a separate constituent, the PR composite can be easily tailored to suit a particular application [1, 2, 21-23].

In addition to the essential components already mentioned, plasticizers may be included in PR composites in order to lower the glass transition temperature, T_g of the composite, thus enhancing the orientational mobility of the chromophore. The electro optic (EO) effect, when originating from the Pockels effect, depends on the removal of the centrosymmetric nature of the material through the electric field poling. The high T_g of PVK (over 200 °C) dictates the need for the inclusion of the plasticizer such as *N*-ethylcarbazole (ECZ), depicted in Fig. 2, so that the NLO dye may reorient within the established E_{SC} at ambient temperatures. Plasticization usually involves the inclusion of the comparatively inert which does not significantly contribute to any of the essential processes required for the PR effect.

The non-local nature of the PR effect distinguishes it from the other local mechanisms which can modulate the *n* such as photochromism, thermochromism, thermorefraction, and so forth [18]. In a PR material, the E_{SC} is phase shifted related to the illumination pattern. This phase shift can lead to the asymmetric transfer of energy between two incident beams in the PR material and is commonly referred to as asymmetric two-beam-coupling (TBC). When TBC is sufficiently strong, the energy gain exceeds losses, attributable to absorption and reflection, and consequently optical amplification can occur [25, 26].

1.2.2. History. The first observation of the PR effect was in $LiNbO_3$ crystals in 1966 [27], however the beam decollimation was attributed to damage of optical components. In 1967, similar effects were observed in a $KTa_xNb_{1-x}O_3$ (KTN) ferroelectric crystal and recognized as the PR effect [28]. Inorganic PR crystals, however, are difficult and expensive to synthesize, and their spectral response depends on their intrinsic absorption

characteristics. In limited cases the absorption characteristics can be manipulated by doping, however, severe shortcomings are often encountered, such as the dopant being expelled during crystal preparation [29]. In contrast, organic PR materials provide an easy and flexible fabrication process, providing a potential improvement in performance [30].

The first PR activity in an organic material was in the NLO crystal 2-cyclooctylamino -5-nitropyridine (COANP) doped with 7,7,8,8-tetracyanoquinodimethane (TCNQ) reported in 1990. Utilization of this material was hindered by instability of the dopant [29, 31]. On the other hand, doping of polymeric or molecular PR materials can be relatively easy. Indeed, the flexibility in processing is one of the most significant merits associated with these materials. Polymeric PR materials can be easily formed into thin-films of various thicknesses depending on the specific requirements. The first polymeric PR material was formulated in 1991 and was composed of the NLO epoxy polymer, poly(bisphenol-A-diglycidyl ether 4-nitro-1,2-phenylenediamine) (bisA-NPDA), doped with 30 wt% of the hole transporting agent, diethylaminobenzaldehyde diphenylhydrazone (DEH) [32].

Recent progress in nano-technology has made it possible to photosensitize PR polymer composites by doping them with Q-dots. The first such example involved the photosensitization of a PVK-based composite with CdS Q-dots in 1999 [13]. Subsequently, photosensitization of PR polymeric composites with Q-dots focused on CdSe and CdS for use at visible wavelengths, and PbSe and PbS for use at near IR wavelengths [14, 15, 33].

1.2.3. Photorefractive Mechanism. Figure 1.3 shows the microscopic mechanism of the PR effect: a) Photosensitizer generates free charge carriers by illumination. b) The photo-generated hole is transferred to the charge-transport material where it can then migrate under the influence of E into the dark fringes of the illumination pattern. c) Charge-carriers become tapped in dark fringes. d) The resulting E_{SC} modulates the n through the addition of a NLO dye.

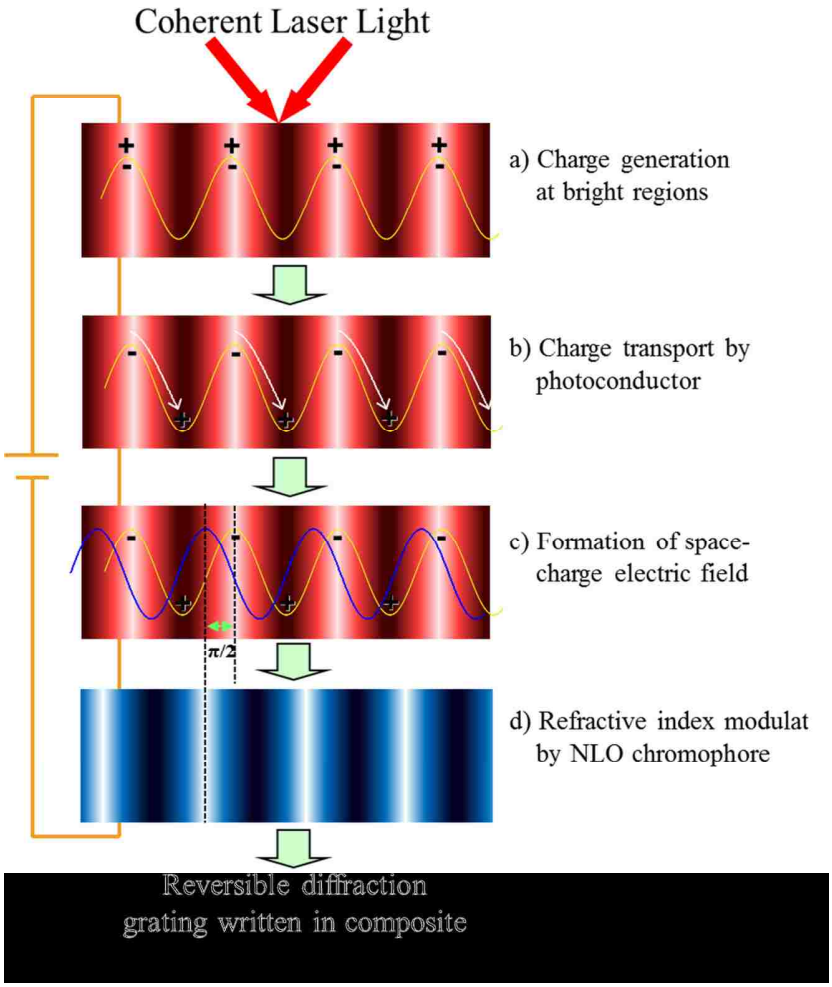

Figure 1.3. Microscopic mechanism of the PR effect.

1.2.3.1. Photosensitization. The first process required in the PR effect is the generation of free charge-carriers and is accomplished by inclusion within the PR composite of a species capable of optical absorption at the wavelength of interest. Because of the limitations associated with C_{60} and other organic photosensitizers, Q-dots have been the subject of recent studies with regard to potential photosensitization of PR composites [13-16]. While this new class of inorganic-organic hybrid polymeric composites shows enormous promises, the technology is still in its infancy, and further investigation is required to exploit its full potential. Operational voltages, diffraction efficiencies, and τ of inorganic-organic PR composites do not equal that of their all-organic counterparts and must be improved to meet the requirements of projected applications [32, 33]. In order to attend to these concerns, the fundamental mechanisms involved in photocharge generation and charge transport need to be elucidated and innovative methods devised, allowing the PR performance to be optimized for a specified application. This optimization can be accomplished through variation of the constituents' stoichiometric ratio and careful choice of the Q-dot's properties.

Perhaps the most attractive aspect of using Q-dots as photosensitizers concerns the tunability in operating wavelength. This tunability originates from the inverse correlation between the optical band-gap and the physical dimension of the Q-dots, known as quantum confinement, and results in a blue-shift in the absorption spectrum of the given material as its proportions are decreased beyond the dimensions of the associated Bohr radius [34-36]. In CdS, the quantum confinement effect arises when the particle size is smaller than ~6 nm [13]. Fig. 1.4 depicts the absorption spectra of QPbS of various sizes. Evident in the figure is the blue-shift associated with quantum

confinement. Fig. 1.5 depicts QCdSe in toluene. This figure also demonstrated quantum confinement as the color of the QCdSe shifts from dark brown to yellow. Because Q-dots are considerably smaller than the wavelengths associated with visible light, their inclusion does not adversely affect the optical quality of the PR composite.

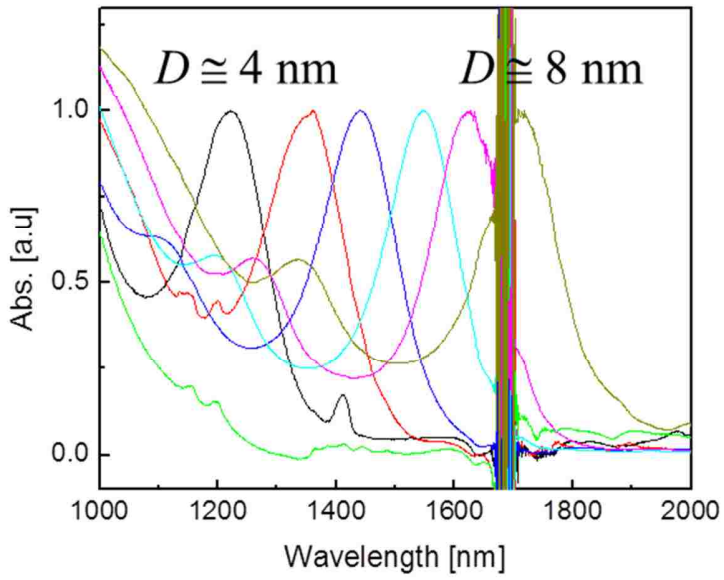

Figure 1.4. Absorption spectrum of PbS Q-dots in hexane ranging in size from 4 nm to 8nm.

Figure 1.5. Color distribution of CdSe Q-dots in toluene by different sizes.

Although Q-dots were originally intended for purposes of photosensitization, through the course of their study, it was observed that composites containing Q-dots also possessed other desirable characteristics. Most notably is the observed increase in charge carrier mobility, μ, which is associated with a faster PR τ. In addition to this increase in τ, the inclusion of Q-dots has also been associated with the unfortunate decrease in diffraction efficiencies, and has been attributed to the propensity of Q-dots to act as charge traps. However, recent studies have demonstrated that this detrimental effect can be minimized through the use of relatively narrow band-gap semiconductors, optimizing both efficiencies as well as τ. This is demonstrated in Fig. 1.6 where, in a representative PR composite, the exchange of the relatively wide band-gap, QCdSe, with QCdTe, which possesses a comparatively narrower band-gap, an improvement in the fast time constant, τ_f, usually ascribed to the formation of the E_{SC}, was realized [33].

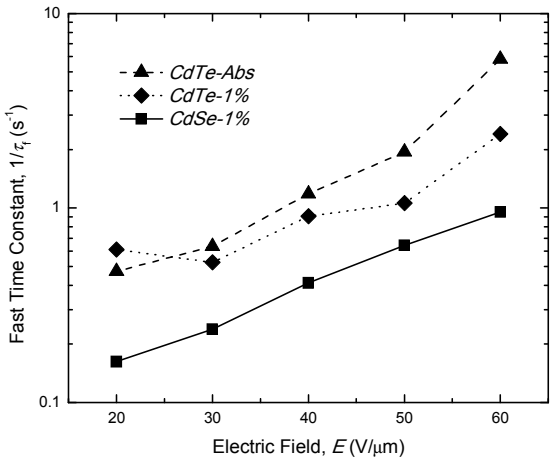

Figure 1.6. Electric field dependence of the fast time constants, τ_f, of the grating growth for *CdSe-1%* (squares), *CdTe-Abs* (triangles), and *CdTe-1%* (diamonds) at $\lambda = 633$ nm. The lines are guides for the eye.

When using Q-dots as a photosensitizer in PR composites they are usually carefully synthesized such the energy associated with their first exciton (or more generally, the E_g), evidenced by a peak in the absorption spectrum, coincides with the intended experimental wavelength. However, as demonstrated herein, PbS Q-dots with a first exciton occurring at ~1200 nm has been used to photosensitize a PR composite at 633 nm. Although the peak of the first exciton does not occur at 633 nm, the PbS Q-dots possess a very large absorption cross-section at 633 nm [13-15, 33]. The need to synthesize Q-dots with a specific size, and therefore a specific band-gap, can be significantly loosen by this "off-resonance" approach.

1.2.3.2. Charge transport. The second process of the PR effect is the transport of the photogenerated charges [30]. Because the holes are associated with the charge transporting matrix, they are the mobile species. By contrast, the electrons are associated with the photosensitizer, which do not form a continuous matrix. Therefore the electron is an immobile species in this type of PR composite, though it is possible to fabricate composites in which the role of the electron and the hole are reversed [39]. Since the μ of holes and electrons are different, an internal space-charge distribution may arise. Charge transport in organic materials is dominated by drift within an electric field. Charge carrier μ is highly dependent on electric field, E, and temperature, T, as

$$\mu = a_0 \rho^2 \exp(-2\rho/\rho_0) \exp\left(\frac{-\Delta}{kT}\right) \exp\left[\beta\sqrt{E}\left(\frac{1}{kT} - \frac{1}{kT_0}\right)\right], \qquad 1)$$

where a_0 is a constant, β and T_0 are parameters fit to the data, ρ is the calculated mean distance between dopant molecules, k is Boltzmann's constant, ρ_0 is the wave function decay length, and Δ is the zero-electric field activation energy [24, 25].

While photosensitization was the primary motivation for the incorporation of Q-dots into otherwise all-organic PR composites, a number of experimental data, particularly those from time-of-flight (TOF) characterizations, indicate that in addition to acting a photosensitizer, the included Q-dots increase the charge-carrier μ within the composite [37]. This enhancement in μ is primarily attributed to the ability of the free charge-carriers to enter, and subsequently be transported through the included Q-dots, where they experience a faster μ relative to that attributed to the conventional organic charge-transporting species. The enhancement in the μ subsequently drives a reduction in the PR τ [20, 33, 38]. In spite of this progress, until recently, $\tau >$ 100 ms represented the best PR τ reported for an organic composite photosensitized with Q-dots [33, 38]. This τ is nearly two orders of magnitude larger than those reported for PR composites photosensitized with organic photosensitizers such as C_{60} [4-6, 19, 39-42]. A recent study investigated the photosensitization of the PR composite at λ = 633 nm through the inclusion of QPbS where the QPbS exhibited a significant, but off-resonance, absorption, resulting in $\tau <$ 40 ms and diffraction efficiencies comparable to those observed in all-organic PR composites. In addition, as mentioned before, Q-dots which possess a narrower band-gap also experience an improvement in τ [33]. The historical progress in τ is shown in Table 1.1.

Table 1.1. Comparison of response time in different PR materials. BBP refers butyl benzyl phthalate as a plasticizer. * Compositions used in paper I.

Composition	**Year**	**Response Time, τ**
$LiNbO_3$ [7]	1966	300 *s*
QCdS/PVK/TCP/NPP [26]	1999	7.3 *s*
QCdTe/PVK/AODCST/ECZ [46]	2007	117 *ms*
PbS/PVK/AODCST/ECZ *	2014	40 *ms*
C_{60}/PVK/7-DCST/BBP [60]	1998	5 *ms*
C_{60}/PTPDAE/EHDNB [7]	2002	1 *ms*

It is largely the charge-transporting species which governs the τ in a PR composite. Recent research indicates that the substitution of PVK with TPD-based species results in a superior PR performance. This can be attributed to several factors, including the higher μ associated with TPD. In addition, as depicted in Fig. 1.7, TPD is more easily ionized than is PVK since the HOMO of TPD lies higher in energy at approximately − 5.43 eV, than that of PVK which occurs at − 5.92 eV. Furthermore, when PVK is used in conjunction with certain NLO dyes, such as 4-azacycloheptylbenzylidene-malononitrile (7-DCST) (see Fig. 1.8) which has a HOMO occurring at − 5.92 eV, it is energetically favorable for the positively charged holes to become trapped at a 7-DCST molecule, whereas in the case of TPD this issue is avoided [14, 43].

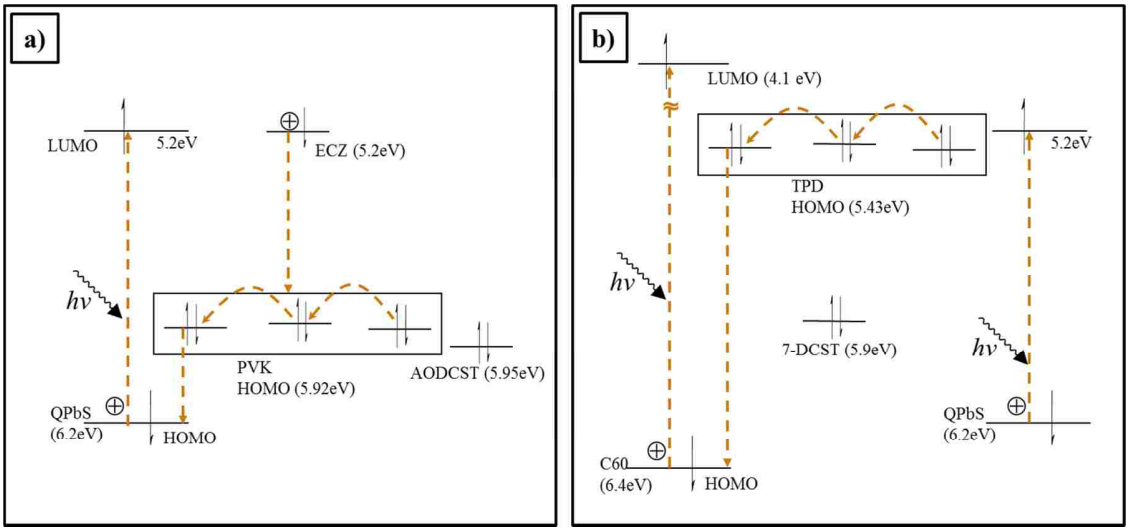

Figure 1.7. Electronic states of (a) PVK and (b) TPD-based composites. AODCST and 7-DCST as NLO chromophores and C_{60} and/or QPbS as sensitizer/charge transport agent [44]. The figure is not to scale.

Due to the enhanced charge-carrier μ associated with TPD based PR materials in conjunction with a valence-band lower in energy than that associated with PVK, greater efficiencies and faster τ have been reported [37, 44]. Because TPD and its molecular derivatives have a high propensity to phase separate and ultimately crystalize in a solid solution with low T_g, lessening the optical quality of the PR device, polymerized forms of TPD, such as poly(acrylic tetraphenyldiaminobiphenyl) (PATPD), have commonly been employed for this application. In the PATPD, the TPD moiety is in a pendant geometry, attached to an inert backbone as well as an inert pendant linkage, thus decreasing the efficiency of the PR composite through the adding of an ineffectual volume [45]. However, as shown herein, N,N-Bis(3-methylphenyl)-N,N-bis(phenyl)benzidine (DMTPD), depicted in Fig. 1.8, in conjunction with the appropriately chosen co-

components, mixed in the proper ratio, forms a stable PR composite where a molecular form of TPD acts as the primary charge-transport species. Through this approach, the inert backbone as well as the pendant linkage associated with polymerized forms of TPD can be eliminated, greatly increasing the loading content of the active components and thereby improving the PR performance. This approach also affords a composite which does not require the addition of the inert plasticizer to lead to the desired birefringence associated with the reorientation of the NLO dye within the soft matrix. This also allows a greater loading of active components.

1.2.3.3. Charge trapping. The photo-generated charges migrate under the influence of *E* into the darker regions of the illumination pattern by a drift dominated mechanism. Charge trapping is usually accomplished without any additive, relying on oxidative impurities as well as imperfections in the sample, where transporting of the generated charge is prohibited during some period time [46-49]. This process results in the establishment of the E_{SC} expressed as

$$\left|E_{\mathrm{SC}}\right| = m \cdot E_{\mathrm{q}} \cdot \left[\frac{E_0^2 + E_{\mathrm{d}}^2}{E_0^2 + \left(E_{\mathrm{d}} + E_{\mathrm{q}}\right)^2}\right]^{1/2} \cdot \frac{1}{1 + \sigma_{\mathrm{d}}/\sigma_{\mathrm{p}}}. \qquad 2)$$

Where *m* is the depth of modulation, E_0 is the component of *E* which coincides with the grating vector, E_{q} is the magnitude of the trap-density-limited E_{SC}, and E_{d} is that of the diffusion field [50]. The σ_{p} and σ_{d} are the photoconductivity and dark conductivity, respectively, and calculated by

$$\sigma = J/E\,, \qquad 3)$$

where J is the experimentally determined current density.

1.2.3.4. Modulation of refractive index. The final process associated with the PR effect involves the modulation of n within the established E_{SC}. This is accomplished through the addition of a second-order NLO dye, possessing a large ground state dipole moment, strong birefringence, and often capable of exhibiting a significant Pockels effect due to a large first hyperpolarizability [51], such as 2-[4-bis(2-methoxyethyl)amino]-benzylidenemalononitrile (AODCST), depicted in Fig. 1.8 and 7-DCST. The dipolar chromophores are able to orient within E as well as the internal E_{SC}. This modulation in orientation translates into a modulation of the bulk n. The magnitude of the modulation of the n is given by the equation

$$\Delta n = -\frac{n^3 r_{eff} E_{SC}}{2}\,, \qquad 4)$$

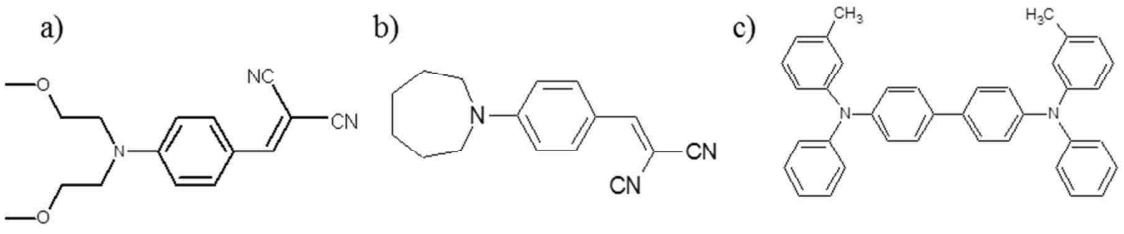

Figure 1.8. Structure of a) AODCST, b) 7-DCST, and c) DMTPD.

where r_{eff} is the effective EO coefficient. The sinusoidally varying E_{SC} ideally results in a sinusoidally varying modulation of n [32]. This modulation of n constitutes a PR grating or hologram. Because the phase between the illumination pattern and modulation of n is nonzero, the grating is nonlocal in nature and leads to an asymmetric energy transfer in the TBC experiment [51]. The orientation of chromophore within E and E_{SC} is shown in Fig. 1.9.

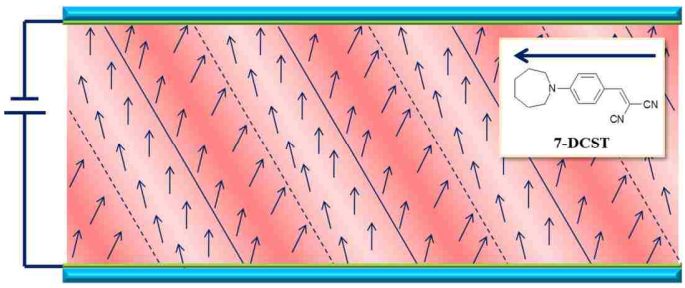

Figure 1.9. Orientation of the NLO chromophore via E and E_{SC}.

PR holograms can be made quasi-permanent when the material has a T_g higher than ambient T. Here, the sample is first heated above its T_g and then the hologram is written. While the writing beams are still present, the sample is cooled to below its T_g, "freezing" the chromophores in place. For the dynamic nature of the PR effect to be observed the T_g of the material must be below the ambient T. As discussed before, composites based on the molecular form of TPD have a T_g below the ambient T. Moreover, issues such as phase separation and crystalization can be suppressed by judicious choice of co-constituents.

1.3. EXPERIMENTAL TECHNIQUES

1.3.1. Synthesis and Sample Preparation. The Q-dots were synthesized through a well-established high-temperature approach utilizing 1-octadecene (ODE) as the reaction solvent. Also oleic acid (OA) was used as a passivating group, providing solubility in organic environments, and preventing aggregation during device processing [40]. Briefly, a reaction flask was charged with lead(II) oxide (PbO) and OA. In a separate flask, hexamethyldisilathiane (TMS) was dissolved in ODE. The temperature of the previously prepared lead oleate solution was raised and the TMS/ODE solution was injected into the reaction flask. The reaction was observed to turn brown to black, at which time it was quenched with an ice bath. The QPbS was stored in this solution until used in the fabrication of PR devices. For PR composites, the product was purified with successive precipitations with methanol in toluene, [40]. The synthetic procedure resulted in QPbS with a diameter of 3.62 ± 0.58 nm corresponding to a band-gap of ~ 1.02 eV, relatively narrow in comparison to λ = 633 nm (1.96 eV).

In the work included in Paper II, 7-DCST was chosen over AODCST due to its superior τ and lower absorption coefficient, α [57]. In the synthesis of 7-DCST hexamethyleneimine, fluoro benzaldehyde, and sodium carbonate were dissolved in dimethyl sulfoxide (DMSO). After heating, the solution was washed in a separatory funnel using trichloro ethane and water. After being dried under vacuum, the product was dissolved in propanol with malononitrile and piperidene. 7-DCST was obtained after several recrystallizations.

1.3.2 Photoconductivity Measurement. σ_p, characterizations were made using a simple dc-photocurrent technique with a Keithley electrometer used to measure the current passing through the sample as a function of *E* under illumination. Fig. 1.10 shows a schematic of the experimental geometry. The σ_d can be measured with this technique also. To measure the σ_d, an *E* was applied and the current was allowed to reach a steady state [13].

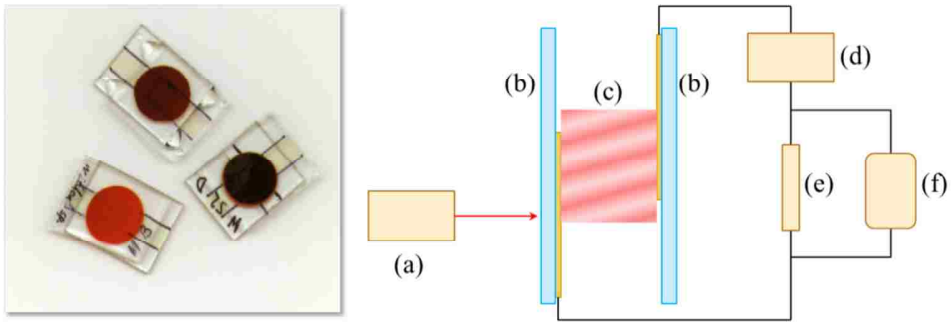

Figure 1.10. Picture of actual samples, and the PC measurement setup; a) laser source, b) ITO glass, c) sample, d) high voltage source, e) load resister, f) electrometer.

To measure the σ_p the sample was initially illuminated for several minutes followed by the application of the *E* and the current was allowed to achieve a steady state. These data were calculated using Eq. 3. From the σ_p data it is possible to determine the internal charge-generation quantum efficiencies, Φ, of the photosensitizer using the equation [13, 14]

$$\Phi = \frac{N_{cc}}{N_{ph}} = \frac{\sigma_p hcE}{Ie\lambda\alpha_\lambda d}. \quad 5)$$

Where N_{cc} is the number of charge-carriers generated per unit volume, N_{ph} is the number of photons absorbed per unit volume, h is Plank's constant, c is the speed of light, d is the sample thickness, I is the intensity, and e is the fundamental unit charge.

1.3.3. Two-Beam Coupling (TBC). The asymmetric transfer of energy between two incident beams in the TBC experiment is one essential technique to investigate the PR performance of a new material [52]. Fig 1.11 shows schematic geometry of TBC and four-wave-mixing experiment. Fig. 1.11a shows the geometry of the TBC experiment. The polymer composite is in between two indium tin oxide (ITO) glasses which are conductive and transparent. The thickness of polymer film is typically on the order of 100 μm.

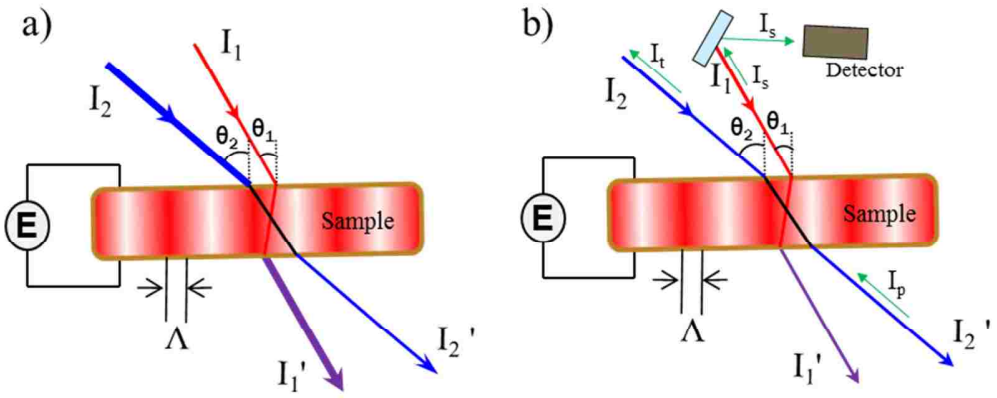

Figure 1.11. Experimental geometry used in a) two-beam coupling, b) time resolved degenerate-four-wave mixing.

Optical beams I_1 and I_2 interfere within the PR composite and create a nonlocal diffraction grating. This phenomenon is entirely unique to PR gratings due to their nonlocal characteristics, expressed as a nonzero phase shift between the optical interference pattern and the grating. Due to the nonzero phase shift, the diffracted beams, I_1 and I_2 interfere constructively or destructively each other. As a result, one beam gains energy at the expense of the other [12]. The TBC gain coefficients, Γ, is given in terms of the experimentally measured quantities $\gamma$and β, as

$$\Gamma = \left[\ln(\gamma\beta) - \ln(\beta + 1 - \gamma)\right]/L, \quad 6)$$

where β is the ratio of the writing beam intensities before the sample, and $\gamma$is the ratio of the intensity of the beam experiencing gain with and without the pump beam and L is the interaction length, given by

$$L = \frac{d}{cos\theta}. \quad 7)$$

Here d is the thickness of the sample and θ is the internal angle of the beam experiencing gain. The TBC coefficient is also expressed as

$$\Gamma = \Gamma_0 \sin \Phi_{ps}, \quad 8)$$

where Φ_{ps} is the phase shift between the E_{SC} and the illumination pattern, and

$$\Gamma_0 = \frac{4\pi\Delta n}{\lambda m_d}. \quad 9)$$

Here m_d is the modulation depth of the interference pattern, and is expressed as

$$m_d = \frac{2\sqrt{\beta}}{1+\beta}. \quad 10)$$

From equation 8, it can be drawn that when the phase shift is $\pi/2$, asymmetric transfer of energy between two incident beams will be maximized. In other words, when $\Phi = 0$, the hologram is in phase with the interference pattern and there is no asymmetric transfer of energy between the two incident beams [13, 14].

1.3.4. Time Resolved Degenerate-Four-Wave-Mixing (DFWM). As shown in Fig. 1.11b, the DFWM technique is quite similar to that of TBC with the exception that the writing beams are *p*-polarized for TBC and *s*-polarized in DFWM. It is well known that *p*-polarized beams interact with PR diffraction gratings more efficiently than *s*-polarized beams [51]. As such, there is less energy transfer between the *s*-polarized writing beams than those of *p*-polarization writing beam in the TBC thus minimizing the distortion of the grating [51]. Another difference involves the presence of a *p*-polarized probe (reading) beam in the DFWM experiment which counter-propagates to one of the writing beams and is partially diffracted from the grating created by two writing beams. The DFWM is used in quantifying the diffraction efficiency, η, of a PR material. Because the probe beam is easily monitored by a photo-detector, the diffracted beam intensity can

be measured as a function of time, applied electric field, and so on. The internal diffraction efficiency, η_{int}, can be expressed as

$$\eta_{ext} = \frac{I_S}{I_p}. \quad 11)$$

Here I_s is intensity of the signal beam and I_p is intensity of the probe beam. And the internal diffraction efficiency, η_{int}, can be expressed as

$$\eta_{int} = \frac{I_S}{I_{p'}}, \quad 12)$$

where, $I_{p'}$ is the transmitted portion of the probe beam without the E.

With Γ and η_{int} for the series of PR devices, it is possible to calculate the magnitude of Φ_{ps} according to the equation [53]

$$\Phi_{ps} = \sin^{-1}\left\{\Gamma L \Big/ \left[(\cos\theta_1 + \cos\theta_2)\sin^{-1}\sqrt{\eta_{\text{int}}}\right]\right\}. \quad 13)$$

Since Φ_{ps} pertains to the distance free charge-carriers traveled prior to becoming trapped, it also provides insight into the occurrence of traps which are sufficiently deep to immobilize the charges.

1.4. APPLICATION OF QDOTS IN BIOLOGY

Some metal nanoclusters such as those composed of Au and Ag show similar properties to Q-dots with regard to their fluorescence and/or tunability. The wavelength of Au nanoclusters can be tunable from 20 nm to 2 nm in size of nanoclusters. However, the limited knowledge of their optical physics as well as their removal from *body* still need to be studied [54]. In addition, diamonds containing nitrogen -vacancies (the most common impurity in natural diamond, type Ia) exhibit relatively strong green fluorescence. Nitrogen vacancies can be artificially prepared by irradiation of the diamonds with a proton beam generated from a particle accelerator, followed by thermal annealing. Notwithstanding the excellent biocompatibility and optical properties, the difficulties in preparation and functionalization are a significant obstacle [55]. Using paramagnetic iron oxide nanoparticles as a magnetic resonance imaging (MRI) contrast agent is another field of interest in biology. Iron oxide nanoparticles have been functionalized with various kinds of ligands, especially those relevant in cancer treatments. MRI can only detect hydrogen atoms in the body without any contrast agent. The specific tumor targeting contrast agent is necessary to improve the resolution of the image [56].

The development of nontoxic Q-dots as luminescence probes in biological research is of recent interest due to their unique optical and chemical properties, such as a size-dependent tunable fluorescence, a sharp and symmetrical fluorescence peak, strong and stable emission, higher quantum yield, brightness, and photo stability [57-61]. In addition, relative to traditional dyes and fluorescent proteins, Q-dots carry advantages such as tunable emission wavelengths, broader excitation spectra, and high resistance to photo

bleaching [62, 63]. On the other hand, the potential applications of Q-dots in biology and medicine are still limited because of their toxicity [64]. Due to the significant toxicity of PbS and CdSe, some of the most common Q-dots, it is challenging to apply Q-dots in biology [65].

Recently, a number of techniques, such as gold outer shells, targeted ligand-like peptide, proteins, and polymer coatings have been developed to minimize the toxicity of Q-dots [66-71]. Q-dots can be functionalized using covalent conjugation to link desired probe materials to the surface of the Q-dot. The organic capping layer on the surface of the Q-dot may possess reactive groups that interact with target molecules in a covalent or noncovalent manner. Q-dots have been linked covalently with biorecognition molecules, such as biotin, oleic acid, peptides, bovine serum albumin, transferrin, antibodies, and DNA [60-63, 72-75].

Several cell-penetrating peptides (CPPs) and monoclonal antibody, trastuzumap, so called Herceptin, were used as surface materials on Q-dots to tracklung and breast cancer cells. The CPPs comprised of basic amino acid-rich sequences are able to penetrate the cell membrane and deliver molecular cargo into living cells [68-71]. Herceptin is monoclonal antibody that interferes with the HER2 receptor. The HER2 receptor is major receptor associated with a certain type of breast cancer; therefore, Herceptin is widely used for the targeted treatment of this type of breast cancer [76]. Generally, Q-dots do not enter cells and aggregation often occurs before and after internalization [63, 77]. To overcome these limitations, functionalization of the surface of Q-dots has been performed with CPPs and Herceptin by either covalent (Herceptin) [77-79] or noncovalent (CPPs) [79-81] linkages. Water-soluble, biocompatible, carboxyl- and

PEG-bi-functionalized InP/ZnS Q-dots, and CdSe/ZnS Q-dots were synthesized. Evaluation of CPP-and Herceptin-mediated uptake of QInP and QCdSe was carried out with lung cancer cells (A549) and breast cells (SK-BR3).

The synthesis of CdSe/ZnS quantum dots was performed using recently reported methods [40]. A mixture of trioctylphosphine oxide (TOPO), tetradecyl phosphonic acid (TDPA), and cadmium oxide (CdO) was heated to obtain a clear solution. A solution containing Se powder was dissolved in trioctylphosphine (TOP) and injected quickly into the hot solution. The solution was cooled to room temperature and highly luminescent CdSe nanocrystals were isolated and purified by centrifugation followed by precipitation with methanol and redissolved in toluene. To obtain the CdSe/ZnS core-shell Q-dots dots, the precipitated CdSe Q-dots were dispersed in TOP. In addition, diethylzinc ($ZnEt_2$) and hexamethyldisilathiane ($(TMS)_2S$) were dissolved in TOP upon gentle heating. After cooling to room temperature, the resulting mixture was injected dropwise into a reaction flask containing CdSe slowly. After the addition was complete, the particles were stirred for 6 hrs. The prepared CdSe/ZnS QDs were dissolved in chloroform ($CHCl_3$) and purified further by centrifugation and precipitation by methanol.

1, 2-distearoyl-sn-glycero-3-phosphoethanolamine-N-[carboxy(polyethyleneglycol)-2000] (DSPE-PEG 2000) and 1,2-dipalmitoyl-sn-glycero-3-phosphoethanolamine-N-[methoxy(polyethyleneglycol)-2000] (PEG-2 PE) (1 : 4 mol%) were dissolved in chloroform and transferred to a three neck flask containing CdSe/ZnS Q-dots in chloroform. When the reaction was complete, the chloroform was removed under vacuum, and the residue was mixed with water and transferred to a centrifuge tube.

Subsequently, water was added to the mixed solution, and the precipitated product was separated by centrifugation and washed with water [82].

Figure 1.12 shows the schematic procedure of the synthesis of lipidized InP/ZnS Q-dots. The preparation of InP was based on modifications of procedures found in literature [83]. Indium (III) acetate and hexadecanoic acid were mixed in octadecane. Tris(trimethylsilyl)phosphine (TMSP) was injected, and the temperature was raised. Following the reaction, the flask was quickly cooled by applying compressed air, yielding InP Q-dots. The size and shape, which affects the optical properties of InP Q-dots were controlled by the reaction time. A sufficient amount of butanol and methanol mixture was added to precipitate the product, which was subsequently washed with methanol and toluene. Formation of InP/ZnS core-shell structure and lipidization with PEG lipid was performed in the same manner as lipidization of CdSe/ZnS mentioned above.

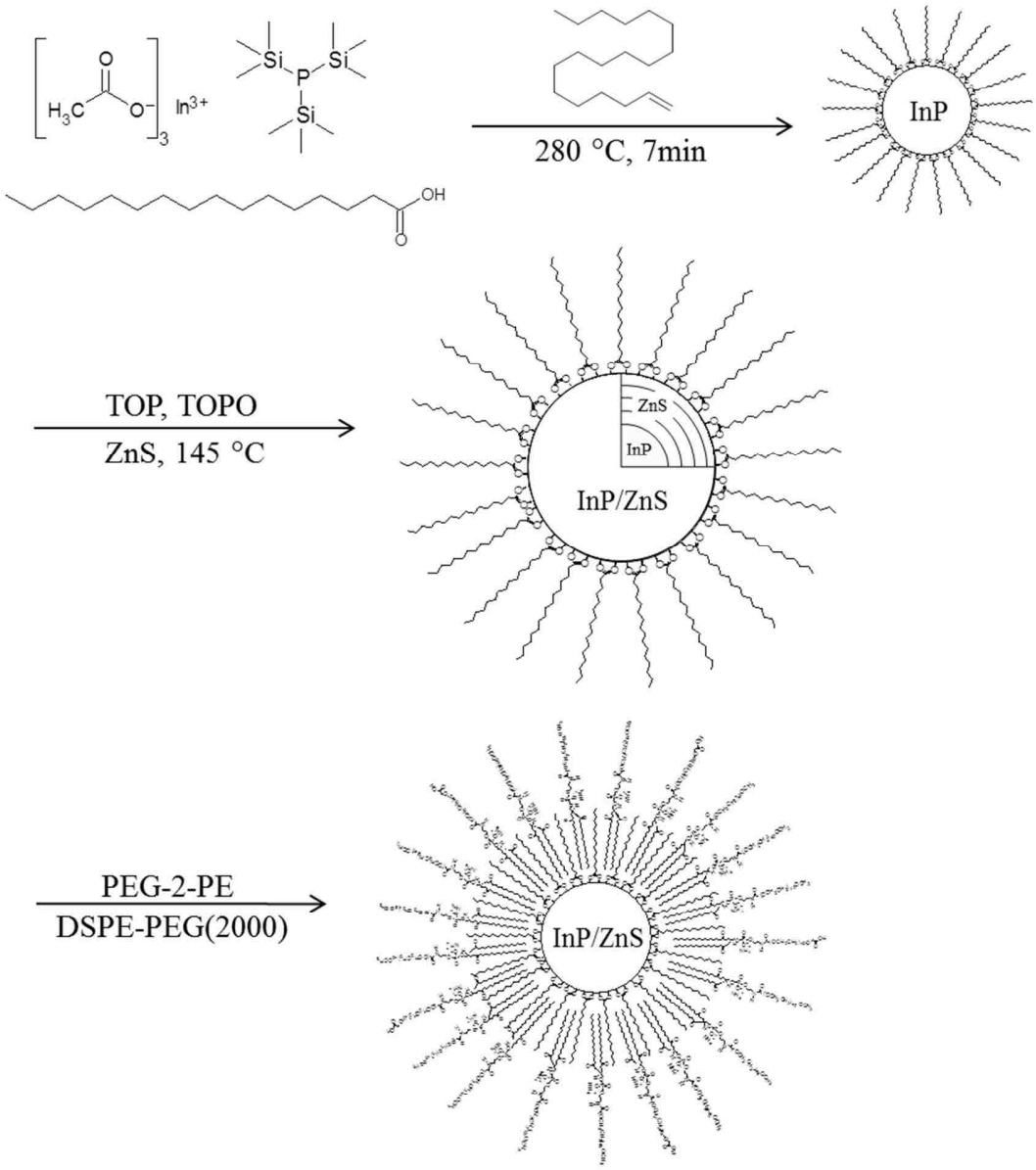

Figure 1.12**.** Synthesis and schematic structure of lipidized InP/ZnS.

REFERENCES

[1] *Photorefractive Materials and Their Applications, I & II, Topics in Applied Physics*, Vols. 61-62; Gunter, P., Huignard, J.-P., Eds.; Springer-Verlag: Berlin, **1988**.

[2] Yeh, P. *Introduction to Photorefractive Nonlinear Optics*; Wiley: New York, **1993**.

[3] Meerholz, K.; Volodin, B.; Kippelen, B.; Peyghambarian, N. *Nature* **1994**, 371, 497–500.

[4] Eralp, M.; Thomas, J.; Li, G.; Tay, S.; Schulzgen, A.; Norwood, R.; Peyghambarian, N.; Yamamoto, M. *Opt. Lett*. **2006**, 31, 1408–1410.

[5] Fuentes-Hernandez, C.; Suh, D.; Kippelen, B.; Marder, S. *Appl. Phys. Lett*. **2004**, 85, 534-537.

[6] Goonesekera, A.; Wright, D.; Moerner, W. *Appl. Phys. Lett*. **2000**, 76, 3358-3360.

[7] Ostrauskaite, J.; Karickal, H.; Leopold, A.; Haarer, D.; Thelakkat, M. *J. Mater. Chem.* **2002**, 12, 58-64.

[8] Wright, D.; Gubler, U.; Moerner, W.; DeClue, M.; Siegel, J. *J. Phys. Chem. B* **2003**, 107, 4732-4737.

[9] Kober, S.; Gallego-Gomez, F.; Salvador, M.; Kooistra, F.; Hummelen, J.; Aleman, K.; Mansurova, S.; Meerholz, K. *J. Mater. Chem*. **2010**, 20, 6170–6175.

[10] Tsutsumi, N.; Kinashi, K.; Nonomura, A.; Sakai, W. *Materials* **2012**, 5, 1477-1486.

[11] Gallego-Gomez, F.; Alvarez-Santos, J.; Rodriguez-Redondo, J.; Font-Sanchis, E.; Villalvilla, J. Sastre-Santos, A. Diaz-Garcia, M.; Fernandez-Lazaro, F. *J. Mater. Chem.* **2012**, 22, 12220–12228.

[12] Grishina, A.; Krivenko, T.; Savel'ev, V.; Rychwalski, R.; Vannikov, A. *High Energy Chem*. **2013**, 47, 46–52.

[13] Winiarz, J.; Zhang, L.; Lal, M.; Friend, C.; Prasad, P. *Chem. Phys.***1999**, 245, 417-428.

[14] Winiarz, J.; Zhang, L.; Lal, M.; Friend, C.; Prasad, P. *J. Am. Chem. Soc.* **1999**, 121, 5287-5295.

[15] Winiarz, J. G.; Zhang, L.; Park, J.; Prasad, P. N. *J. Phys. Chem. B.* **2002**, 106, 967-970.

[16] Aslam, F.; von Ferber, C. *Chem. Phys*. **2009**, 362, 114–119.

[17] *Nonlinear Optical Properties of Organic Molecules and Crystals*; Vols. 1 and 2; Chemla, D. S., Zyss, J., Eds.; Academic Press: Orlando, **1987**.

[18] *Photochromism*; Vols 1-3; Brown, G. H., Eds.; Wiley-Interscience: New York, **1971**.

[19] Zhu, J.; Kim, W.; He, G.; Seo, J.; Yong, K.; Lee, D.; Cartwright, A.; Cui, Y.; Prasad, P. *Appl. Phys. Lett*. **2010**, 97, 263108.

[20] Moerner, W.; Silence, S. *Chem. Rev.* **1994**, 94, 127-155.

[21] Ostroverkhova, O.; Moerner, W. E. *Chem. Rev.* **2004**, *104*, 3267-3314.

[22] Thomas, J.; Norwood, R. A.; Peyghambarian, N. *J. Mater. Chem.* **2009**, *19*, 7476-7489.

[23] Salvador, M.; Prauzner, J.; Koeber, S.; Meerholz, K.; Turek, J. J.; Jeong, K.; Nolte, D. D. *Opt. Exp.* **2009**, *17*, 11834-11849.

[24] Prasad, P. N.; Cui, Y.; Swedek, B.; Cheng, N.; Kim, K. S. *J. Phys. Chem. B.* **1997**, *101*, 3530-3534.

[25] Valley, G. *J. Opt. Soc. Am. B-Opt. Phys.* **1984**, 1, 868-873.

[26] Grunner-Jepsen, A.; Thompson, C.; Moerner, W. *Science* **1997**, 277, 549-552.

[27] Ashkin, A.; Boyd, G. D.; Dziedzic, J. M.; Smith, R. G.; Ballman, A. A.; Levinstein, J. J.; Nassau, K. *Appl. Phys. Lett*. **1966**, 9, 72.

[28] Chen, F. S. *J. Appl. Phys.* **1967**, *38*, 3418-3420.

[29] Sutter, K.; Hulliger, J.; Gunter, *P. Solid State Commun.* **1990**, 74, 867-870.

[30] Moerner, W.; Silence, S.; Hache, F.; Bjorklund, G. J. Opt. Soc. Am. B. **1994**, 11, 320-330.

[31] Moerner, W.; Silence, S.; Hache, F.; Bjorklund, G. J. Opt. Soc. Am. B. **1994**, 11, 320-330.

[32] Moerner, W.; Silence, S. *Chem. Rev.* **1994**, 94, 127-155.

[33] Winiarz, J. *J. Phys. Chem. C* **2007**, 111, 1904-1911.

[34] Wang, Y.; Herron, N. *J. Phys. Chem.* **1991**, *95*, 525-532.

[35] Steigerwald, M.; Brus, L. *Acc. Chem. Res.* **1990**, *23*, 183.

[36] Henglein, A. *Topics in Current Chemistry* **1988**, *143*, 113.

[37] Moon, I.; Choi, J.; Kim, N. *Macromol. Chem. Phys*. **2013**, 214, 478–485.

[38] Moon, J.; Mahala, B.; Winiarz, J. *J. Phys. Chem. C.* Submitted

[39] Sanchez, F.; Kayoun, P.; Huignard, J. *J. Appl. Phys*. **1988**, 64, 26-31.

[40] Barkhouse, D.; Pattantyus-Abraham, A.; Levina, L.; Sargent, E. *ACS Nano* **2008**, 2, 2356-2362.

[41] Binks, D.; Bant, S.; West, D.; O'Brien, P.; Malik, M. *J. Mod.Opt.* **2003**, 50, 299-313.

[42] Tay, S.; Thomas, J.; Eralp, M.; Li, G.; Norwood, R.; Schülzgen, A.; Yamamoto, M.; Barlow, S.; Walker, G.; Marder, S.; Peyghambarian, N. *Appl. Phys. Lett.* **2005**, *87*, 171105.

[43] Thomas, J.; Fuentes-Hernandez, C.; Yamamoto, M.; Cammack, K.; Matsumoto, K.; Walker, G.; Barlow, S.; Kippelen, B.; Meredith, G.; Marder, S.; Peyghambarian, N. *Adv. Mater.* **2004**, 16, 2032–2036.

[44] Meerholz, K.; Volodin, B.; Kippelen, B.; Peyghambarian, N. *Nature* **1994**, 371, 497–500.

[45] Li, H.; Termine, R.; Godbert, N.; Angiolini, L.; Giorgini, L.; Golemme, A. *Org. Electron*. **2011**, 12, 1184–1191.

[46] Grunnet-Jepsen, A.; Wright, D.; Smith, B; Bratcher, M.; Declue, M.; Siegel, J.; Moerner, W. *Chem. Phys. Lett.* **1998**, 291, 553–561.

[47] Daubler, T. K.; Bittner, R.; Meerholz, K.; Cimrova, V.; Neher, D. *Phys. Rev. B*, **2000**, 61, 13515-13527.

[48] Ostroverkhova, O.; Singer, K. D. *J. Appl. Phys.* **2002**, 92, 1727-1743.

[49] Van Steenwinckel, D.; Hendrickx, E.; Persoons, A. *J. Chem. Phys.* **2001**, 114, 9557-9564.

[50] Kukhtarev, N.; Markov, V.; Odulov, S.; Soskin, M.; Vinetskii, V. *Ferroelectrics* **1979**, *22*, 949-960.

[51] Moerner, W. E.; GrunnetJepsen, A.; Thompson, C. L. *Annu. Rev. Mater. Sci*. **1997**, 27, 585.

[52] Walsh, C.; Moerner, W. *J. Opt. Soc. Am. B* **1992**, 9, 1642-1647.

[53] Ducharme, S.; Scott, J.; Twieg, R.; Moerner, W. *Phys. Rev. Lett.* **1991**, 66, 1846-1849.

[54] Lin, C.; Lee, C.; Hsieh, J.; Wang, H.; Li, J.; Shen, J.; Chan, W.; Yeh, H.; Chang, W. *J. Med. Biol. Eng.*, **2009**, 26, 276-283.

[55] Wee, T.; Mau, Y.; Fang, C.; Hsu, H.; Han, C.; Chang, H. Diamond Relat. Mater, 18 (2009) 567–573.

[56] Yang, L.; Peng, X.; Wang, A.; Wang, X.; Cao, Z.; Ni, C.; Karna, P.; Zhang, X.; Wood, W.; Gao, X.; Nie, S.; Mao, H. *Clin. Cancer. Res.* **2009**. 15, 4722-4732.

[57] Alivisatos, A. *Science* **1996**, 271, 933–937.

[58] Mattoussi, H.; Palui, G.; Na, H.; *Adv. Drug Deliv. Rev*. **2012**, 64, 138–166.

[59] Yong, K.; *Theranostics*, **2012**, 2, 629–630.

[60] Bruchez, M.; Moronne, M.; Gin, P.; Weiss, S.; Alivisatos, A. *Science* **1998**, 281, 2012–2016.

[61] Chan, W.; Nie, S. *Science* **1998**, 281, 2016–2018.

[62] Chen, F.; Gerion, D. *Nano Lett*. **2004**, 4, 1827–1832.

[63] Michalet, X.; Pinaud, F.; Bentolila, L.; Tsay, J.; Doose, S.; Li, J.; Sundaressan, G.; Wu, A.; Gambhir, A.; Weiss, S. *Science* **2005**, 307, 538–544.

[64] Shao, L.; Gao, Y.; Yan, F. *Sensors* **2011**, 11, 11736–11751.

[65] Zhang, Y.; Wang, T. *Theranostics* **2012**, 2, 631–654.

[66] Farias, P.; Santos, B.; Fontes, A. *Meth. Mol. Biol.* **2009**, 544, 407–419.

[67] Hu, R.; Law, W.; Lin, G.; Ye, L.; Liu, J.; Reynolds, L.; Yong, K. *Theranostics* **2012**, 2, 723–733.

[68] Madani, F.; Lindberg, S.; Langel, U.; Futaki, S.; Graslund,A. *J. Biophys*. 2011, **2011**, 414729.

[69] Mager, I.; Langel, K.; Lehto, T.; Eiriksdottir, E.; Langel, U. *Biochim. Biophys. Acta* **2012**, 1818, 502–511.

[70] van den Berg, A.; Dowdy, S. Curr. Opin. *Biotechnol*. **2011**, 22, 888–893.

[71] Schmidt, N.; Mishra, A.; Lai, G.; Wong, G. *FEBS Lett*. **2010**, 584, 1806–1813.

[72] Pinaud, F.; King, D.; Moore, H.; Weiss, S. *JACS*, **2004**, 126, 6115–6123.

[73] Hanaki, K.; Momo, A.; Oku, T. *Biochem. Biophys. Res. Comm.* **2003**, 302, 496–501.

[74] Goldman, E.; Anderson, G.; Tran, P.; Mattoussi, H.; Charles, P.; Mauro, *J. Anal. Chem.* **2002**, 74, 841–847.

[75] Gerion, D.; Parak, W.; Williams, S.; Zanchet, D.; Micheel, C.; Alivisatos, A. *JACS* **2002**, 124, 7070–7074.

[76] Hudis, C. *N Engl J Med* **2007,** 357, 39-51.

[77] Xue, F.; Chen, J.; Guo, J.; Wang, C.; Yang, W.; Wang, P.; Lu, D. *J. Fluoresc*. **2007**, 17, 149–154.

[78] Koshman, Y.; Waters, S.; Walker, L.; Los, T.; de Tombe, P.; Goldspink, P.; Russell,B. *J. Mol. Cell*. Cardiol. **2008**, 45, 853–856.

[79] Wei, Y.; Jana, N.; Tan, S.; Ying, *J. Bioconjug. Chem*. **2009**, 20, 1752–1758.

[80] Liu, B.; Huang, Y.; Chiang, H.; Lee, H. *J. Nanosci. Nanotechnol*. **2010**, 10, 7897–7905.

[81] Xu, Y.; Liu, B.; Lee, H.; Shannon, K.; Winiarz, J.; Wang, T.; Chiang, H.; Huang, Y. *J. Biomed. Biotechnol*. **2010**, 2010, 948543.

[82] Liu, B.; Huang, Y.; Winiarz, J.; Chiang, H.; Lee, H. *Biomaterials* **2011**, 32, 3520–3537.

[83] Depalo, N.; Mallardi, A.; Comparelli, R.; Striccoli, M.; Agostiano, A.; Curri, M. *J. Col. Int. Sci.* **2008**, 325, 558-566.

PAPER

I. OFF-RESONANCE PHOTOSENSITIZATION OF A PHOTOREFRACTIVE POLYMER USING PbS NANOCRYSTALS

ABSTRACT

Due to their enhanced spectral response, photorefractive polymeric composites photosensitized with semiconductor nanocrystals are emerging as an important class of materials. Despite their promising characteristics, several deficiencies persist. Relatively low diffraction efficiencies and slow response times have prevented these materials from reaching their full potential. Here, we report on the photosensitization of photorefractive polymeric composites at visible wavelengths through the inclusion of narrow band-gap semiconductor nanocrystals composed of PbS. Unlike previous studies involving the photosensitization of a photorefractive polymer composite with inorganic nanocrystals, we employ an off-resonance approach where the first excitonic transition associated with the PbS nanocrystals lies at ~ 1220 nm even though photorefractive characterizations are conducted at 633 nm. Through this approach, internal diffraction efficiencies in excess of 82% have been observed, two-beam-coupling gain coefficients in excess of 211 cm-1, and response times 34 ms, representing some of the best figures-of-merit reported for this class of materials. These data mark a significant advancement for this class of materials and demonstrate the ability for semiconductor nanocrystals to compete with traditional organic photosensitizers. In addition to these promising characteristics, this approach also provides an inexpensive and easy means by which to photosensitive composite materials.

The photoconductive characteristics of the composites used for this study will also be described.

KEYWORDS

Photorefractive, Lead sulfide, Photoconductive, Holography, Nanocrystal, Semiconductor

1. INTRODUCTION

Owing to their substantial optical nonlinearities, low permittivity and low cost, polymeric photorefractive (PR) materials are potentially useful in a variety of real-time optical information processing applications including beam clean-up and amplification, dynamic interferometry, phase conjugation, and pattern recognition [1-5]. Consequently, a great deal of research has focused on the development of this class of materials, resulting in significant advances, including millisecond response times, τ, and nearly 100 % diffraction efficiencies, η [3]. In addition to these notable figures-of-merit, polymer based PR composites are also attractive due to the ease with which their constituents may be independently modified, allowing the eventual composite to be tailored for a specific application. Ordinarily, PR composites are composed of a charge-transporting polymer matrix doped with a non-linear optical dye capable of modulating its refractive index under the influence of a space-charge field. It is also customary to include a photosensitizer, capable of absorbing the employed optical radiation and subsequently produce free charge-carriers within the photoconductive (PC) matrix.

With the establishment of nano-technology it is now possible to photosensitize PR and PC polymer composites by doping them with semiconductor nanocrystals, also

known as *quantum dots orQ-dots* [6-19]. This approach has numerous advantages, perhaps the most appealing is the ability to readily manipulate the spectral features of Q-dots, and therefore the operational wavelength,λ, of the composite into which they are doped [6-9]. Control over the optical and electrical properties of the nanocrystalline material stems from the inverse correlation between the optical band-gap and the physical dimension of the Q-dots. This inverse relationship translates into a blue-shift in the absorption spectrum of a given material as its proportions are decreased beyond the dimensions of the associated Bohr radius. In addition, Q-dots are considerably smaller than the wavelengths associated with visible light; and as such, their inclusion does not adversely affect the optical quality of the PR composite.

While this new class of inorganic-organic hybrid polymeric composites shows enormous promise, the technology is still in its infancy and much work is needed to exploit its full potential. Operational voltages, diffraction efficiencies, and response times associated with PR inorganic-organic composites do not equal that of their all-organic counterparts and must be improved to meet the requirements of projected applications. In order to attend to these concerns, the fundamental mechanisms involved in photocharge generation and charge transport must be elucidated and innovative methods devised allowing for the PR performance to be optimized for a specified application. This optimization can be accomplished through variation of the constituents' stoichiometric ratio and prudent choice of the Q-dot's properties. Recently, advancements in the syntheses of Q-dots have significantly improved control over nanocrystal morphology, surface characteristics, and most notably, composition. Nevertheless, with few exceptions [10, 13, 14],studies concerning the photosensitization of PR polymeric composites with

Q-dots have focused on CdSe and CdS for use at visible wavelengths and PbSe and PbS for use at near IR wavelengths.

In this communication we describe the PR performance of a series of polymeric composites photosensitized through the inclusion of PbS nanocrystals (QPbS), synthesized using an approach based on a previous report in the literature.[20] This intention was inspired by results obtained in a previous study in which it was demonstrated that the PR performance of a polymeric composite could be enhanced by exchanging QCdSe, which has been traditionally utilized as a photosensitizer in studies conducted at visible wavelengths [10, 12-14], for the more novel QCdTe [18]. Here it was established that exchanging the relatively wide band-gap QCdSe with QCdTe, which possesses a comparatively narrower band-gap, an improvement in the was realized. The improvement in was primarily attributed to the ability to more fully exploit the faster charge-carrier mobility associated with the nanocrystals relative to that of the organic photoconductive matrix. Despite these promising results with regard to the τ, an anticipated enhancement in other PR parameters such as the degenerate-four-wave-mixing (DFWM) efficiency and two-beam-coupling (TBC) coefficient were not realized. The data presented in that study suggested that this deficiency could primarily be attributed to the excessive trapping of positively charged free charge-carriers by the QCdTe. In an effort to circumvent this issue, it was hypothesized that the inclusion of a Q-dot species with a much narrower band-gap, while still constituting a trapping species, would provide considerably shallower traps. By all accounts, shallower traps would have a less detrimental effect over the PR performance, allowing free charge-carriers to travel, on average, a longer distance before encountering a terminal-trap, optimizing the phase

shift between the dynamic space-charge field and the interference pattern associated with the writing beams. The data presented herein strongly support the realization of this hypothesis.

A reservation associated with this approach is that the narrow band-gap associated with the photosensitizer will no longer coincide with the energy associated with the employed radiation. In this case, the band-gap will occur at lower energies, or red-shifted relative to the 633 nm used to write the holographic diffraction grating. However, while the first excitonic transition no longer coincides with employed wavelength, this higher energy radiation can still excite higher order transitions where the QPbS possess a very large absorption cross-section. In fact, the absorption of the QPbS is considerably stronger at wavelengths which are largely blue shifted from the peak associated with the lowest energy exciton. Since all previous studies involving Q-dot photosensitization have made use of nanocrystals where the energy of the employed radiation closely coincided with that of the first exciton, the feasibility of this approach was initially in question. However, the data will show that now the requirement that the nanocrystal photosensitizer be carefully synthesized such that their size, and therefore their optical properties, meets the demands imposed by experimental parameters is loosened, greatly simplifying the use of Q-dots for this application.

In an effort to be able to draw a comparison between the results obtained in this study and those obtained for QNiS, QCdSe and QCdTe, with the exception of the photosensitizer, similar components were used in the fabrication of the PR composites. Therefore, in addition to the QPbS photosensitizer, the composites also contained poly(N-vinylcarbazole) (PVK) due to its well characterized hole transporting capability.

The glass transition temperature of the composite was lowered to below ambient temperature through the inclusion of N-ethylcarbazole (ECZ) and electro-optic activity was imparted through the addition of 2-[4-Bis(2-methoxyethyl)amino]benzylidenemalononitrile (AODCST).21 The Q-dots were synthesized through a well-established high-temperature approach utilizing oleic acid (OA) and 1-octadecene (ODE) as the capping groups and reaction solvents, respectively [20]. These procedures will be detailed in the following section.

To characterize the performance of the materials, DFWM, TBC, visible absorption spectroscopy, and conductivity experiments were employed, the results and implications of which will be presented. In addition to the insights gained into the fundamental mechanisms relevant to this class of materials, an enhancement in the PR response time realized, with $\tau <$ 34 ms is. Moreover, a maximum internal diffraction efficiency, η_{int}, of 82%, translating into an external diffraction efficiency, η_{ext}, of 45 %, as well as TBC gain coefficients, Γ, of 211 cm^{-1} have been measured. It is believed that these qualify as some of the highest figures-of-merit recorded for any organic PR composite photosensitized with Q-dots and compare to even the best all-organic PR composites. It is anticipated that the enhancement associated with this approach will be applicable to other systems.

2. EXPERIMENTAL SECTION

All chemicals were obtained from Aldrich and used as received unless otherwise noted. The nanocrystals used in this study were synthesized based on a procedure described in the literature [20].

2.1. Synthesis of QPbS. This procedure is based on a report found in the literature [20]. Briefly, two solutions were prepared, the first by adding 0.18 g of PbO to 4 mL of OA. The solution was then de-gassed under vacuum and mechanically stirred for 1 hour at 80° C, then stored under nitrogen until needed. In a separate vial (with septa top), 0.08437 mL of hexamethyldisilathiane (TMS) were dissolved in 2 mL of 1-octadecene and de-gassed at RT for 1 hour. Then, the temperature of the previously prepared lead oleate solution was raised to 150° C and stirred vigorously under nitrogen. This solution was then quickly injected into the vial containing the TMS solution at which time the reaction was quenched with an ice bath. The QPbS was stored in this solution until used in the fabrication of PR devices. At this time, the temperature of the original reaction mixture was raised to 60°C, and then 10 mL of methanol were injected. The mixture was centrifuged to collect the product which was then redispersed in toluene. Additional methanol was added, the mixture centrifuged and QPbS collected again. This purification procedure was repeated several times to remove any unreacted OA, TMS, and ODE. To remove unreacted PbO, the product was dispersed in toluene, centrifuged and the supernatant was collected. This procedure is known to produce QPbS with an average diameter of ~ 6 nm [20].

It is noted that an attempt was made to exchange the OA ligands associated with the QPbS for pyridine, similar in manner to which the trioctylphosphine was exchanged for pyridine in the studies involving QNiS, QCdSe and QCdTe. In summary, QPbs dispersed in toluene was precipitated through the addition of methanol and centrifuged. The supernatant was discarded and the wet nanocrystals were dispersed in 10 mL of pyridine. This solution was mechanically stirred, however, over the course of several

days it failed to become optically clear and instead an increase in aggregation was observed. For QNiS, QCdSe and QCdTe the ligand exchange procedure was shown to result in a photosensitizer which enhanced the PR properties to the parent composite [18, 19]. In this case, however, due to the rapid aggregation of the QPbS, the effect of this procedure was not part of this study. The QPbS were characterized using visible absorption spectroscopy recorded on a Beckman DU 640B spectrophotometer. The absorption spectra of the QPbS nanoparticle suspensions were obtained in toluene using a 1 cm quartz cell. The QPbS were also characterized via thermal gravimetric analysis using a TA Instruments TGA 2950 run at ramp-rate of 20°C/min in air.

2.2. PR Composite Devices. AODCST was synthesized in our lab according to a procedure in the literature [21]. For the composite samples, PVK (secondary standard), ECZ, AODCST, and the appropriate quantity of capped QPbS were dissolved in toluene:teterahydrofuran (13:1 by weight) and, after thorough mixing, filtered to remove any undissolved solids. This solution was stored in a vacuum oven at 50°C for 24 hours to remove the solvent. The solid residue was subsequently recovered, placed between two pieces of glass coated with indium tin oxide and heated above its melting temperature on a hot-plate. The sample was then mechanically pressed forming the typical "sandwich" geometry using glass spacers to control the thickness, d, of the device at 100 μm.

A total of three QPbS-photosensitized devices were fabricated, varying the concentration of QPbS in each. To determine the weight percentage of QPbS in each composite, several QPbS:solvent solutions of known absorbance and volume were evaporated to dryness and the mass of the solid residue was measured. It is noted that this residue includes the inorganic PbS as well as the organic passivating layer. The weight

percent of QPbS in each device was thus calculated indirectly from the known absorbance and volume of the aliquot used in the fabrication of the respective composite. For all PR devices, the PVK:AODCST:ECZ ratio was held constant. It is well known that above a threshold concentration, Q-dots will typically aggregate in organic environments such as those associated with the PR composites used in this study. Therefore, employing light scattering experiments, we first determined the maximum achievable concentration of QPbS in the organic composite which would not detrimentally affect the optical quality of the PR device. In this case, it was determined that a concentration of ~ 4.5 wt% resulted in scattering of 633 nm radiation which was comparable to a device containing no QPbS. For this reason, the first PR device was fabricated such that it contained 4.28 wt% of QPbS, and this device is herein referred to as PBS4. This QPbS concentration resulted in a device absorption coefficients at $\lambda = 633$ nm, α_{633}, of 26.7 cm^{-1}. Previous studies, and most notably those involving QCdTe, have shown that such high concentrations of Q-dots often diminish the PR performance relative to lower Q-dot concentrations [18, 19]. This behavior has been attributed to a coincidental increase in the concentration of deep traps. As detailed, it is specifically this undesirable behavior which is the subject of this study and therefore in order to gauge the success of this strategy, and to optimize the achievable PR performance using this approach, several additional PR devices were fabricated with successively lower QPbS concentrations. Specifically, concentrations of 1.47 wt % and 0.445 wt%, were employed, representing approximately 1/3 and 1/10 the QPbS concentration associated with the PBS4 device. These PR devices are herein referred to as PBS1 and PBS0.4 respectively. The compositions and the spectroscopically measured α_{633} of all devices are presented in Table 1.

Table 1. Compositions and α_{633} of the photorefractive devices used in this study.

Device	PVK (wt %)	AODCST (wt %)	ECZ (wt %)	Q-PbS (wt %)	α_{633} (cm^{-1})
PBS0.4	44.8	44.8	10.0	0.445	4.24
PBS1	44.3	44.3	9.85	1.47	9.38
PBS4	43.1	43.1	9.57	4.28	26.7

The PR devices have not shown any change in their optical properties or degradation in PR performance over the course of 9 months. UV-Vis absorption spectra were recorded on a Beckman DU 640B spectrophotometer.

2.3. PR Characterizations. The PR properties of the composite devices were studied via TBC and DFWM techniques using a standard tilted geometry. Holographic gratings were written through the intersection of two coherent beams generated by a helium-neon (HeNe) laser operating at 633 nm with incident angles of $\theta_1 = 45°$ and $\theta_2 = 75°$ (in air) relative to the sample normal. In the TBC experiments, both writing beams were *p*-polarized with intensities of $I_1 \sim 0.05$ mW and $I_2 \sim 8$ mW. The external bias was applied such that I_1 would experience gain at the expense of I_2. Asymmetric energy transfer was observed by monitoring the intensities of the writing beams after the PR device with a photodiode. In the DFWM experiment the writing beams were *s*-polarized with intensities of $I_1 \sim 3$ mW and $I_2 \sim 9$ mW. In addition, a *p*-polarized probe beam propagated in a direction opposite to I_1 with an intensity of $I_p \sim 2 \times 10^{-3}$mW. Through the

use of a polarizing beam splitter placed in the path of I_2 in conjunction with a photodiode, the diffracted portion of I_p, also referred to as the signal beam, I_s, could be quantified. All beams had diameters of 0.98 mm.

Photoconductivity, σ_p, characterizations were made using a dc-photocurrent technique with a Keithley electrometer used to measure the current passing through the sample as a function of applied bias. The beam intensity for all σ_p characterizations was ~ 10 mW.

3. RESULTS AND DISCUSSION

The goal of this study was to improve the PR performance at visible λ of a polymeric composite photosensitized with semiconductor Q-dots. This is to be accomplished by replacing the more traditional wide band-gap Q-dots, such as QCdS, QCdSe and QCdTe, with relatively narrow band-gap Q-dots, in this case, QPbS. The initial motivation for this approach was based on the anticipated decrease in propensity for trapping of free charge-carriers by the relatively narrow band-gap Q-dots. However, employing a narrow band-gap Q-dot also necessarily implies that, unlike all previous studies concerning Q-dot photosensitization, the energy associated with impinging radiation, 633 nm in this case, would not coincide with the energy associated with the band-gap of the photosensitizer. Founded in convention, it was anticipated that this may result in diminished PR performance. However, deeper contemplation reveals that, relative to the traditional narrow band-gap Q-dots, the QPbS would have a largely enhanced absorption cross-section at 633 nm. As such, it will be possible to achieve a higher PR device absorption with a relatively lower concentration of nanocrystals, even

further decreasing the overall concentration of traps which may be associated with the Q-dot photosensitizer. Then again, whether the relatively highly energetic excitons would allow for the positively charged hole to transfer from the Q-dot to the PC matrix, effectively contributing to the free charge-carrier population, would be a major component of the current study. Furthermore, it was anticipated that the since effective photosensitization can be accomplished with a lower Q-dot concentration, the response time may be adversely affected. This speculation is based on the observation that increased Q-dot loading can result in an enhanced PR response time [18]. Data will indicate that the positive aspects of this approach largely outweigh any negative qualities. The absorption spectrum of the QPbS dispersed in toluene is depicted in Figure 1.

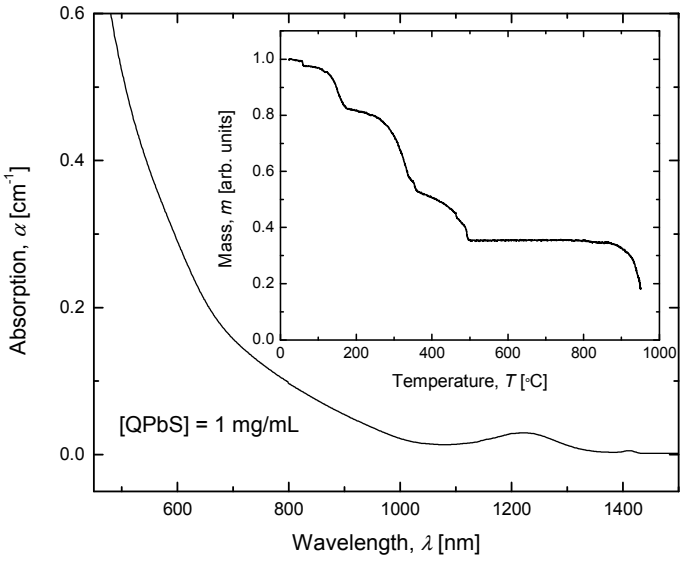

Figure 1.Visible absorption spectrum of QPbS in toluene.
The inset depicts the TGA data obtained for the QPbS.

Evident in the figure is that the absorption associated with the first exciton occurs at ~1220 nm, corresponding to a band-gap of 1.02 eV. This is compared to the value of 0.37 eV for bulk PbS, clearly demonstrating the effect of quantum confinement [22]. It is additionally apparent that at a normalized concentration of 1 mg/mL, the QPbS exhibits an absorption of $\alpha_{1220} = 0.0296$ cm^{-1} at this wavelength. The same concentration of QPbS possesses $\alpha_{633} = 0.234$ cm^{-1}, nearly an order of magnitude larger than α_{1220}. The presence of the well-defined peak at ~1220 nm indicates a high degree of mondispersity and coincides with the presumed 6 nm diameter of the QPbS [20].

As detailed in the experimental section, attempts to conduct ligand exchange on the QPbS were unsuccessful and therefore the as-synthesized QPbS were used in the remainder of this study. In order to quantify the ratio of organic capping material to inorganic PbS present in the QPbS, TGA was conducted, the results of which are presented in the inset of Fig. 1. Apparent from the figure is that ~ 2-3 wt% of the QPbS is lost at ~ 60° C. Although the sample was dried under vacuum at room temperature prior to analysis, this initial loss can likely be attributed to residual solvent, primarily toluene in this instance. Following this feature, it is observed that organic components are lost in three distinct phases until ~ 500° C is attained. The first loss phase terminates at ~ 170° C and it is not immediately clear as to the composition of the component lost during this phase. The second loss phase terminates at 360° C, the boiling point of OA, and can therefore likely be attributed to the loss of OA which is loosely associated with the inorganic PbS. The third and final loss phase terminates at ~ 500° C and although experimental proof is wanting, can expectedly be attributed to OA which is covalently associated with the surface of the inorganic PbS nanocrystal. Subsequent to ~ 500° C, a

constant mass is observed until ~ 850° C is achieved. It is this mass which is attributed to the inorganic PbS, which accounts for 33.6 wt% of the as-synthesized QPbS.

PR devices were fabricated photosensitized with QPbS. In order to optimize the PR performance which could be achieved using this specific photosensitizer, a series of PR devices were fabricated, starting with the maximum concentration of QPbS which could be incorporated prior to aggregation. As detailed beforehand, a concentration of 4.28 wt% was slightly below the concentration where aggregation would be observed, thus establishing the concentration of QPbS in the device labeled as PBS4. However, it has been described in several previously published studies that the optimized PR performance typically occurred at Q-dot concentrations lower than the maximum achievable concentration [18, 19], and therefore PR devices possessing progressively smaller concentrations of QPbS were fabricated and studied, decreasing the concentration of QPbS by approximately a factor of three in each increment. As will be seen, of all the relevant compositions studied, in fact it was PBS4 which demonstrated the best PR performance and therefore results for this composition will be presented. In addition, in order to illustrate critical points, results obtained for PR devices containing 1.47 wt% and 0.445 wt% QPbS, labeled as PBS1 and PBS0.4 respectively, will also be provided. The absorption spectra for PBS4, PBS1 and PBS0.4 are provided in Figure 2 and their α_{633} are given in Table 1. In addition, in the inset of Figure 2, the α_{633} for each device are plotted as a function of the wt % concentration of inorganic PbS in each device. The data were fit to a linear least squares function which also plotted in the inset. Notably, a good fit is obtained which exhibits a *y*-intercept of 1.22 cm^{-1}, interpreted as the α_{633} of 0 wt% of QPbS.

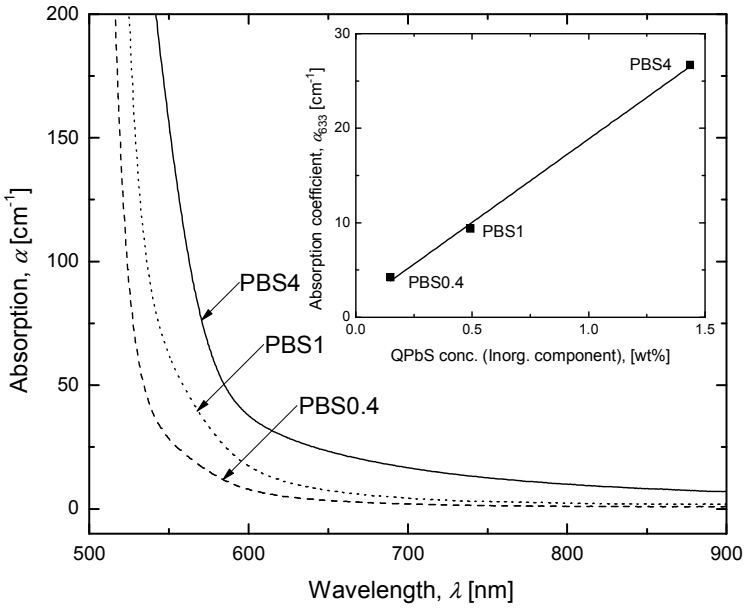

Figure 2. Visible absorption spectra of the PR devices used in this investigation; PBS4 (solid line), PBS1 (dotted line), and PBS0.4 (dashed line). The inset depicts α_{633} for each device vs. wt % concentration of inorganic PbS. The line represents a linear least squares fit of the data.

As described, there was large initial uncertainty regarding the ability of the QPbS to effectively inject charge-carries in to photoconductive matrix. Although the QPbS possessed an appreciably large α_{633}, the absorption at this wavelength did not coincide with the first excitonic absorption as it has all previous studies, located in this case at 1220 nm. Therefore, in an effort to assess the effectiveness of the photosensitizer, the photoconductivities, σ_p, as well as the dark conductivities, σ_d, were measured at $\lambda = 633$ nm and are presented as a function of the externally applied electric field, *E*, in Figure 2.3. These data were calculated using the equation

$$\sigma = J/E\,, \tag{1}$$

where J is the experimentally determined current density. Looking initially at the σ_p, it is observed that the σ_p increases in a regular way with QPbS concentration. Similar trends have been reported for other Q-dot sensitized composites as well as for all-organic composites [3, 18]. It is noted however that in some Q-dot photosensitized composites an opposite trend has been observed in that the σ_p was reported to decrease as Q-dot concentration was increased [19]. That study involved QNiS, and the trend was likely attribute to increased aggregation of the Q-dots, which was not an issue in this study. Based on the σ_p data, it was determined that while the first excitonic peak associated with the QPbS did not coincide with the wavelength of employed radiation, the QPbS nonetheless acted as a very efficient photosensitizer in the studied composite.

As seen in Figure 3, the σ_d is relatively independent of Q-PbS concentration. In this case, increasing the Q-dot concentration by almost a factor of ten less than doubled the σ_d, even with E = 80 V/μm.

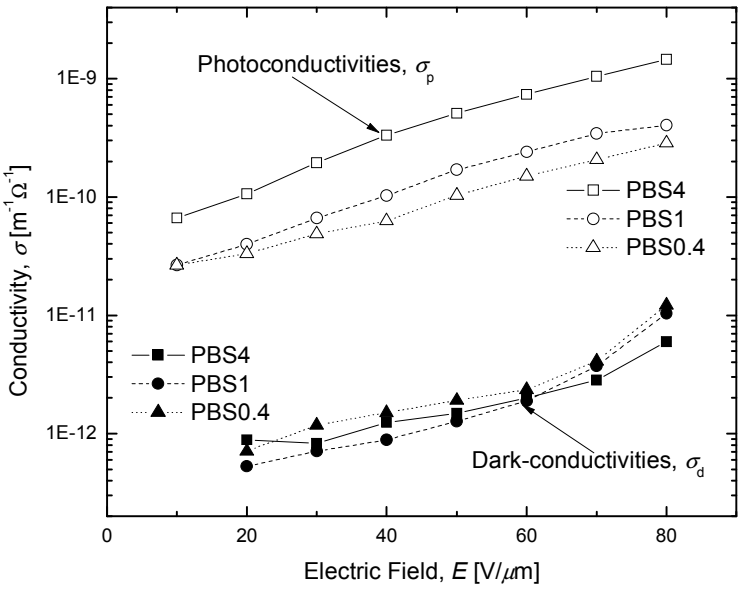

Figure 3. Electric field dependence of the photoconductivities, σ_p, (open symbols) and dark-conductivities, σ_d, (filled symbols) of PBS4 (squares), PBS1 (circles), and PBS0.4 (triangles) at λ = 633 nm. The lines are guides for the eye.

This trend stands in contrast to those observed for other Q-dot photosensitized PR composites. In the case of QCdTe, it was reported that increasing the Q-dot concentration by as little as a factor of 4.3 resulted in a > 3-fold increase in σ_d with E = 60 V/μm (the highest E for which data were reported in this study)[18]. Similarly, increasing the QNiS concentration by a factor of ~ 3 resulted in σ_d increasing by as much as a factor of ~ 5 at E = 70 V/μm.[19] The observation that the conductivity in the absence of illumination is unchanged by a relatively large change in QPbS concentration indicates the lack of influence of the Q-dots over this process. More specifically, evidently, QPbS does not act as a significant trapping species in this PR composite. Further evidence for this

conclusion is forthcoming. It is relevant to note that although PBS0.4 represents the lowest concentration in QPbS presented here, lower concentrations were investigated and no exceptions to the reported trends in σ_d or σ_p were observed.

From the σ_p data it is possible to determine the charge-generation quantum efficiencies, Φ, of the photosensitizer using the equation

$$\Phi = \frac{N_{cc}}{N_{ph}} = \frac{\sigma_p hcE}{Ie\lambda\alpha_\lambda d}, \tag{2}$$

where N_{cc} is the number of charge-carriers generated per unit volume, N_{ph} is the number of photons absorbed per unit volume, h is Plank's constant, c is the speed of light, and e is the fundamental unit charge. The Φ measured for the devices used in this study are depicted in Figure 4.

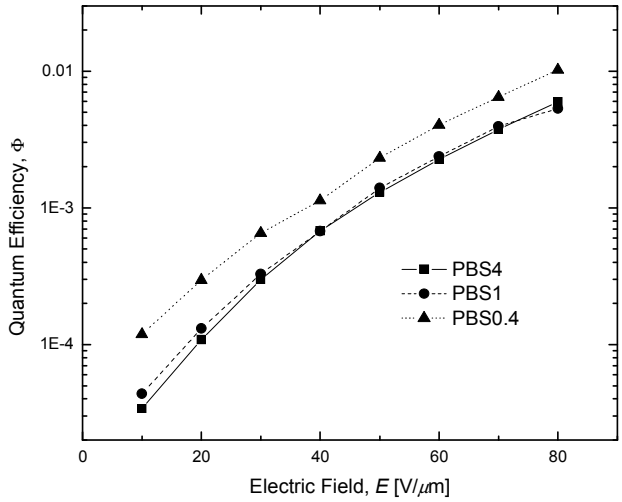

Figure 4. Electric field dependence of the quantum efficiencies, Φ, for PBS4 (squares), PBS1 (circles), and PBS0.4 (triangles) at λ = 633 nm. The lines are guides for the eye.

Immediately apparent is the consistency in magnitude of Φ among the various PR devices across the entire range of *E*. Specifically PBS4 and PBS1 exhibit virtually identical Φ with PBS0.4 showing a slightly higher Φ. Ignoring Q-dot –Q-dot interactions, one would expect Φ to be independent of Q-dot concentration, however, practically speaking, considerations such as aggregation and other interactions between photosensitizing entities often result in a dependence of Φ on concentration. In this case, however, such undesirable interactions appear to be largely absent, most notably those which may be due to aggregation. That being said, the slight enhancement in Φ for the composite containing the smallest concentration of QPbS, i.e. PBS0.4, does indicate that these interactions are not completely avoided. The slight decrease in Φ observed for PBS1 and PBS4 and can almost certainly be attributed to a small degree of aggregation of QPbS caused by the higher QPbS concentration in these devices.

In addition to the fundamental insights gained from the σ data, it was also possible to gauge the potential PR performance form these data. This is so because the magnitude of the spaces-charge field, $|E_{SC}|$, is related to the ratio σ_p/σ_d as dictated by the equation

$$|E_{SC}| = m \cdot E_q \cdot \left[\frac{E_0^2 + E_d^2}{E_0^2 + (E_d + E_q)^2} \right]^{1/2} \cdot \frac{1}{1 + \sigma_d/\sigma_p}, \qquad (3)$$

where *m* is the depth of modulation, E_0 is the is the component of *E* which coincides with the grating vector, E_q is the magnitude of the trap-density-limited space-charge field, and E_d is that of the diffusion field [23]. The σ_p/σ_d data are presented as a function of *E* in

Figure 5. The functional form of the data is highly reminiscent of these data for other Q-dot photosensitized PR composites, with σ_p/σ_d reaching a maximum at intermediate E [18, 19]. Evident in the figure is that PBS4 exhibits the largest σ_p/σ_d achieving a maximum value ~ 3 times that of PBS1 and nearly 7 times that observed PBS0.4. This

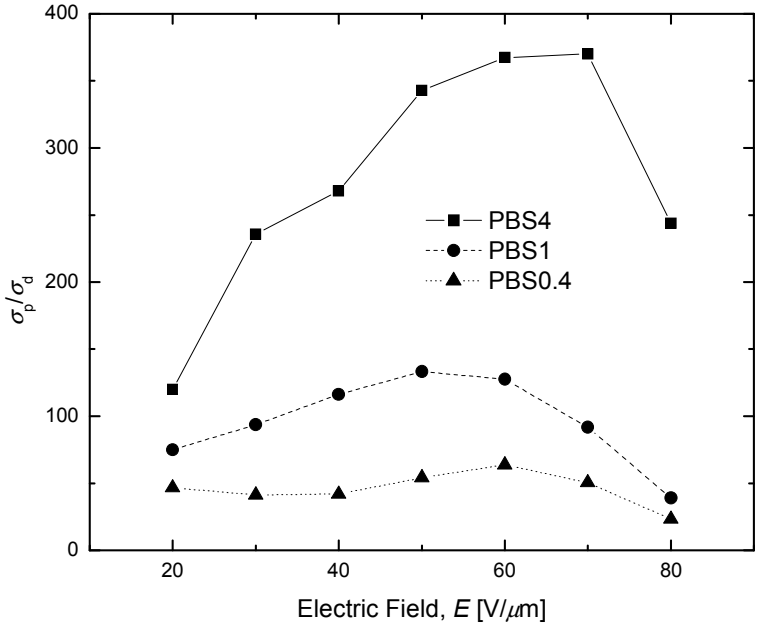

Figure 5. Electric field dependence of the ratio of photoconductivity to dark conductivity, σ_p/σ_d, for PBS4 (squares), PBS1 (circles), and PBS0.4 (triangles) at $\lambda = 633$ nm. The lines are guides for the eye.

reflects the improvement in σ_p with increasing QPbS concentration while not affecting σ_d. Based on these data, it can be predicted that PBS4 will exhibit relatively large diffraction efficiencies as this attribute should correlate directly with $|E_{SC}|$.

Having established the ability of QPbS to photosensitize the PR composite with high efficiency, the next goal was to confirm the PR nature of any holographic gratings which may be formed within the devices. A distinctive feature of the PR effect is that the refractive index grating created in the medium is spatially shifted with respect to the light intensity pattern of the writing beams [24]. As a result, an asymmetric exchange of energy occurs between beams interfering in a PR medium. Therefore, the PR nature of the gratings created within the composites used in this study was confirmed using conventional TBC experiments. The Γ is given in terms of the experimentally measured quantities γ and β, as

$$\Gamma = \left[\ln(\gamma\beta) - \ln(\beta + 1 - \gamma)\right]/L, \tag{4}$$

where L is the path length of the beam experiencing gain inside the sample, β is the ratio of the writing beam intensities before the sample, and γ is the ratio of the intensity of the beam experiencing gain with and without the pump beam. The Γ_{633} are presented as a function of E in Figure 6. Inspection of the data reveals that, as has been the case for similar Q-dot photosensitized PR composites, the usual dependency upon E^2, predicted for organic PR composites, is not observed [18, 19]. In previous studies, as in this one, Γ achieves a maximum and then begins to decrease at relatively high E. In previous observances of such functioning, it was speculated that a correlation existed between the trends observed for Γ and that of σ_p/σ_d. Again, in this study a similar congruence is seen and lends credence to the hypothesized connection.

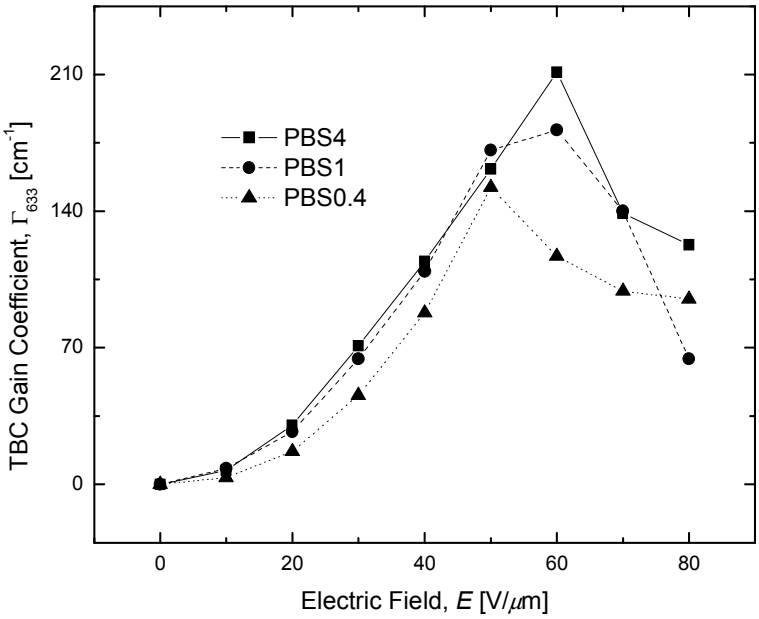

Figure 6. Electric field dependence of the TBC gain coefficient, Γ, for PBS4 (squares), PBS1 (circles), and PBS0.4 (triangles) at $\lambda = 633$ nm. The lines are guides for the eye.

Despite this important similarity among various Q-dot photosensitized composites, other important differences are observed. Specifically, previous studies which looked at the dependence of Γ on Q-dot concentration showed a decrease in Γ as the Q-dot concentration was increased. This detrimental behavior was attributed to the Q-dots acting as deep traps. It was speculated an increase in trap concentration, associated with an increase in Q-dot concentration, resulted in a decrease in the phase shift between the refractive index grating and the light intensity pattern of the writing beams from the ideal value of π/2, thus diminishing the TBC performance. As seen in Figure 6, however, notably different behavior is observed for PR composites photosensitized with QPbS.

Here it is seen that an increase in QPbS concentration is accompanied by an increase in Γ across the entire range of *E* considered. This trend provides further confirmation that by using narrow band-gap Q-dots, such as QPbS, it is possible to significantly reduce the propensity for trapping exhibited by the Q-dots, subsequently optimizing the PR performance of the relevant composite. It is noted that the difference in Γ for the various concentrations is surprisingly minor until $E > 50$ V/μm, where differences become more pronounced. It is further noted that $\Gamma = 211$ cm^{-1} is recorded for PBS4, which is significantly larger than the Γ measured for similar Q-dot photosensitized PR composites. For PR composites photosensitized with QNiS, $\Gamma \approx 80$ cm^{-1} was reported whereas Γ for similar composites containing QCdSe or QCdTe did not exceed 40 cm^{-1}.

For practical applications, the Γ_λ should exceed the α_λ, for a given device. For all devices involved in this study Γ_{633} does exceed α_{633}. In this instance the PBS4 device exhibits the highest figure-of-merit, with $\Gamma_{633} - \alpha_{633} = 184$ cm^{-1} at $E = 60$ V/μm. As such, the results reported herein constitute a significant advancement in this class of materials and for the first time allows Q-dot photosensitized to effectively compete with their all-organic counterparts with respect to practical applications relying on optical amplification.

To access the off-resonance approach to photosensitization with regard to diffraction efficiencies, the η_{int} were evaluated experimentally and quantified according to the equation

$$\eta_{\text{int}} = I_s / I_{p'}, \tag{5}$$

where $I_{p'}$ is the intensity of the probe beam after the device with no bias applied. These data are presented in Figure 7.

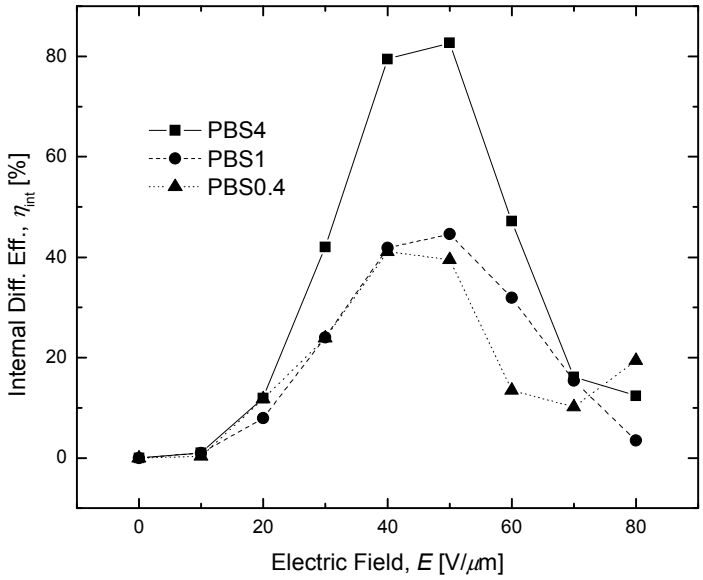

Figure 7. Electric field dependence of the internal diffraction efficiencies, η_{int}, for PBS4 (squares), PBS1 (circles), and PBS0.4 (triangles) at $\lambda = 633$ nm. The lines are guides for the eye.

Immediately conspicuous is the $\eta_{int} = 82.7$ % for PBS4 at approximately the over-modulation field of $E = 50$ V/μm. This stands as one of the highest η_{int}, reported for an organic PR composite photosensitized with Q-dots and, as was the case for the Γ, compares well with current state-of-the-art PR composites, again opening the door with regard to practical applications for this class of materials. As seen in the figure, decreasing the QPbS concentration, resulted in a corresponding decrease in the η_{int}, with PBS1 exhibiting $\eta_{int} = 44.6$ %, also at approximately the over-modulation field of $E = 50$

V/μm. Interestingly, a further decrease in QPbS concentration does not produce a proportionately large decrease in the efficiency with η_{int} = 41.1 % for QPBS0.4. Furthermore, the over-modulation field is clearly lowered to ~ 40 V/μm. Although accompanied by a slight decrease in efficiency, a lowering of the operational over-modulation field is attractive for practical applications.

While the η_{int} are fundamentally important, it is the η_{ext} which are of functional significance. The η_{ext} associated with the devices are shown as a function of *E* in Figure 8. Here η_{ext}, accounting for reflections, was determined according to the equation

$$\eta_{ext} = I_s / I_p \, . \tag{6}$$

As depicted in Figure 2.8, PBS4 exhibited the highest figure-of-merit with a maximum η_{ext} of 44.7 % at *E* = 50 V/μm, however, due to its relatively low α_{633}, PBS0.4 showed a maximum η_{ext} = 37.3 % at a lower *E* = 40 V/μm. In light of the small differences in η_{ext}, the lower QPbS concentration, and hence the lower α_{633}, associated with PBS0.4 as compared to PBS4 or PBS1, may be more favorable for practical applications where lower operational voltages are desired.

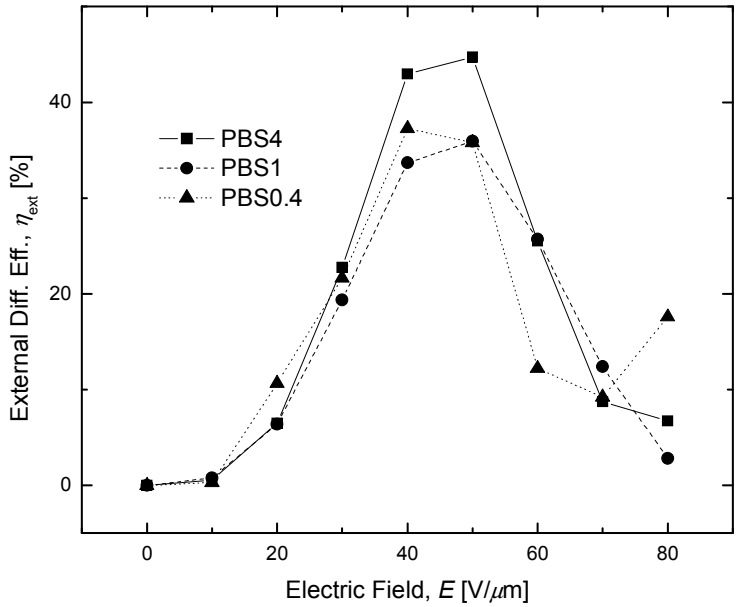

Figure 8. Electric field dependence of the external diffraction efficiencies, η_{ext}, for PBS4 (squares), PBS1 (circles), and PBS0.4 (triangles) at λ = 633 nm. The lines are guides for the eye.

Having established Γ and η_{int} for the series of PR devices, it is possible to gauge the magnitude of the phase shift between the illumination pattern and the modulation of the refractive index, ϕ, according to the equation[24]

$$\phi = \sin^{-1}\left\{\Gamma L \Big/ \left[(\cos\theta_1 + \cos\theta_2)\sin^{-1}\sqrt{\eta_{int}}\right]\right\} . \qquad (7)$$

The results of this manipulation are plotted as a function of E in Figure 2.9 for the relevant PR devices.

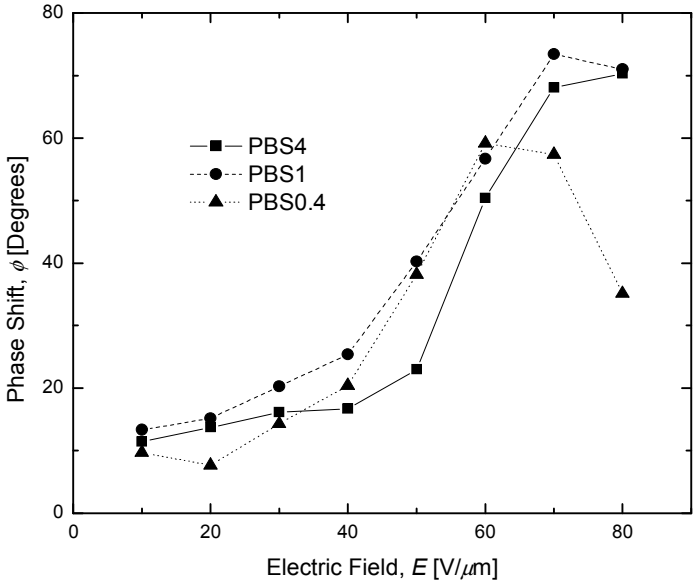

Figure 9. Electric field dependence of the phase shift between the illumination pattern and the modulation of the refractive index, ϕ, for PBS4 (squares), PBS1 (circles), and PBS0.4 (triangles) at $\lambda = 633$ nm. The lines are guides for the eye.

Since ϕ pertains to the distance traveled by free charge-carriers prior to becoming trapped, it also provides insight into the occurrence of traps which are sufficiently deep to immobilize the charge-carriers. For the QPbS photosensitized devices it is apparent that, within the approximate nature of this approach, that the various devices exhibit similar ϕ across the range of E considered. The fact that ϕ, and therefore the deep trap density, are reasonably independent of the concentration of QPbS, is a strong indication that the QPbS are not playing a significant role in terms of charge-trapping, further bolstering the motivating hypothesis that narrow band-gap Q-dots would provide enhanced PR performance based on their diminished propensity to trap free charge-carriers. It is

noteworthy that this behavior is in contrast to that observed in other studies concerning the influence of narrow band-gap Q-dot concentration over this parameter [18, 19]. In these instances, it was invariably found that the composite containing the lowest Q-dot concentration also exhibited the largest ϕ. Moreover, the proximity to the ideal value of ϕ = 90° achieved by all the devices in this study, not only attests to the operational facility of the PR composites but, again, is a strong indication of the absence of deep traps often associated with Q-dot photosensitizers. This observation also stands in contrast to those involving narrow band-gap Q-dots, where the maximum ϕ was ~48° and values of 10° – 30° were much more typical [18, 19]. In these instances, the trends were attributed to the propensity of the narrow band-gap Q-dots to behave as trapping entities.

Although an extensive study of the response times in composites photosensitized with QPbS will be the subject of a future work, at present it is possible to gain insight into this aspect. Time resolved DFWM techniques were used in the quantification of the holographic grating growth rates, τ. For this experiment, E was applied to the device while blocking one of the writing beams. The device was permitted to settle for approximately 30 s and the blocked writing beam was unblocked. The diffracted portion of the probe beam was then recorded as a function of time. The data obtained in this experiment for PBS4 with E = 60 V/μm are presented in Figure 10. The solid line in the figure represents the best fit to a biexponential equation of the form

$$\eta(t) = \sin^2\{A[1 - m\exp -t/\tau_f - (1-m)\exp -t/\tau_s]\}, \quad (8)$$

where A is a fitting constant, m is a weighting ratio, t is time, τ_f is the fast time constant and τ_s is the slow time constant. For the fitting, all four variables were allowed to float. Evident from the figure is that a reasonably good fit to the data is obtained. In this case, $\tau_f = 33.9 \pm 0.4$ ms was derived from the fitting process. This figure-of-merit represents one of the best obtained for any Q-dot photosensitized composite and compares with those reported for state-of-the-art PR materials in general. Also relevant, $\tau_s = 0.391 \pm 0.002$ and $m = 0.648 \pm 0.002$ were recorded, indicating the ability for PBS4 to be used in video-rate applications. It is noted that while visual inspection of the data were subjectively convincing that even faster response times were obtained for larger E, satisfactory fits to the data using equation 8 were not obtained. The reason for this discrepancy will also be the subject of future studies.

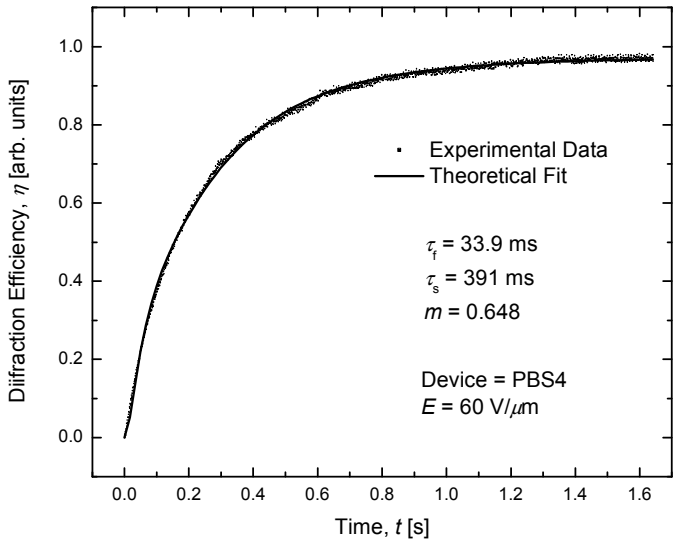

Figure 10. Temporal evolution of the diffracted probe beam, I_s, in the DFWM experiment for the PBS4 device at $E = 60$ V/μm. The solid line is a fit to a weighted biexponential function (see text).

4. CONCLUSION

The feasibility of photosensitizing a polymeric PR composite for use at visible wavelengths using narrow band-gap Q-PbS was investigated. Experimental evidence strongly suggests that previously observed propensity for Q-dots to act as trapping centers is greatly diminished through this approach, resulting in diffraction efficiencies, gain coefficients and response times which are unprecedented PR composites photosensitized through the inclusion of Q-dots. It is important to note that the size of QPbS utilized in this study were arbitrary with regard to the application, with the choice based on the availability and ease of a recipe in the literature. And while this is actually an attractive aspect of this approach, in that the need to carefully synthesize and size-selectively precipitate Q-dots in order to ensure that their optical properties coincide with the experimental parameters is eliminated, future studies should focus on the consequence of optimizing this parameter. Future studies will also look at the ability of other narrow band-gap Q-dots to function in a similar fashion.

ACKNOWLEDGEMENT. The Authors wish to acknowledge the Materials Research Center at the Missouri University of Science and Technology and the Department of Chemistry at the Missouri University of Science and Technology.

REFERENCES AND NOTES

[1] *Photorefractive Materials and Their Applications, I & II, Topics in Applied Physics*, Vols. 61 and 62; Gunter, P., Huignard, J.-P., Eds.; Springer-Verlag: Berlin, 1988.

[2] Yeh, P. *Introduction to Photorefractive Nonlinear Optics*; Wiley: New York, 1993.

[3] Ostroverkhova, O.; Moerner, W. E.*Chem. Rev.* **2004**, *104*, 3267.

[4] Winiarz, J. G.; Ghebremichael, F.; Thomas, J.; Meredith, G.; Peyghambarian, N. *Opt. Exp.***2004**, *12*, 2517.

[5] Winiarz, J. G.; Ghebremichael, F. *Appl. Opt.***2004**, *43*, 3166.

[6] Winiarz, J. G.; Zhang, L.; Lal, M.; Friend, C. S.; Prasad, P. N. *Chem. Phys.***1999**, *245*, 417.

[7] Winiarz, J. G.; Zhang, L.; Lal, M.; Friend, C. S.; Prasad, P. N. *J. Am. Chem. Soc.***1999**, *121*, 5287.

[8] Winiarz, J. G.; Zhang, L.; Park, J.; Prasad, P. N. *J. Phys. Chem. B***2002**, *106*, 967.

[9] Winiarz, J. G.; Prasad, P. N. *Opt. Lett.***2002**, *27*, 1330.

[10] D. J. Binks, S. P. Bant D. P. West, P. O'Brien, and M. A. Malik, J. Mod.Opt. **50**, 299 (2003).

[11] K. R. Choudhury, J. G. Winiarz, M. Samoc, and P. N. Prasad, Appl. Phys. Lett. **82**, 406 (2003).

[12] C. Fuentes-Hernandez, D. J. Suh, B. Kippelen, and S. R. Marder,Appl. Phys. Lett. **85**, 534 (2004).

[13] F. Aslam, D. J. Binks, S. Daniels, N. Pickett, and P. O'Brien, Chem. Phys. **316**, 171 (2005).

[14] F. Aslam, D. J. Binks, M. D. Rahn, D. P. West, P. O'Brien, N. Pickett, S. Daniels, J. Chem. Phys. **122**, 184713 (2005).

[15] K. R. Choudhury, Y. Sahoo, T. Y. Ohulchanskyy, and P. N. Prasad, Appl. Phys. Lett. **87**, 073110 (2005).

[16] K. R. Choudhury, Y. Sahoo, S. Jang, and P. N. Prasad, Adv. Func. Mat. **15**, 1751 (2005).

[17] N. Cho, K. R. Choudhury, R. B. Thapa, Y. Sahoo, T. Ohulchanskyy,A. N. Cartwright, K.-S. Lee, and P. N. Prasad, Adv. Mater. **19**, 232 (2007).

[18]. J. G. Winiarz, J. Phys. Chem. C **111**, 1904 (2007).

[19] T. Fears, C. Anderson, and J. G. Winiarz,J. Chem. Phys. **129**, 1 (2008).

[20] D. A. R. Barkhouse, A. G. Pattantyus-Abraham, L. Levina, and E. H. Sargent, ACS Nano**2**, 2356 (2008).

[21] M. A. Díaz-García, D. Wright, J. D. Casperson, B. Smith, E. Glazer, W. E. Moerner, L. I. Sukhomlinova, and R. J. Twieg, Chem. Mater. **11**, 1784 (1999).

[22] Streetman, Ben G.; Sanjay Banerjee (2000). Solid State electronic Devices (5th ed.). New Jersey: Prentice Hall. p. 524.ISBN 0-13-025538-6.

[23] Kukhtarev, N. V.; Markov, V. B.; Odulov, S. G.; Soskin, M. S.; Vinetskii, V. L. *Ferroelectrics***1979**, *22*, 949.

[24] W. E. Moerner and S. M. Silence, Chem. Rev. **94**, 127 (1994).

[25] R. Bittner, K. Meerholz, G. Steckman, and D. Psaltis, Appl. Phys. Lett. **81**, 211 (2002).

II. SUB-MILLISECOND RESPONSE TIME IN A PHOTOREFRACTIVE COMPOSITE OPERATING UNDER CW CONDITIONS

ABSTRACT

Inspired by the promise of enhanced spectral response, photorefractive polymeric composites photosensitized with semiconductor nanocrystals have emerged as an important class of materials. In addition to providing efficient photosensitization, however, extensive study of these hybrid composites has indicated that the inclusion of nanocrystals also provides an enhancement in the charge-carrier mobility, and subsequent reduction in the photorefractive response time. Unfortunately, the included nanocrystals have also been shown in most cases to increase the deep trap concentration, resulting in a significant decrease in the photorefractive performance, specifically diminished diffraction efficiencies as well as reduced two beam coupling gain coefficients. Nonetheless, evidence suggests that this problem can be largely avoided through the inclusion of semiconductor nanocrystals possessing a relatively narrow band-gap. Here, we fully exploit this quality by doping PbS nanocrystals into a newly formulated photorefractive composite based on molecular triphenyldiamine photosensitized with C_{60}. Through this approach, unprecedented response times of 400 μs are observed, opening the door for video and other high-speed applications. It is further demonstrated that this improvement in response time occurs with little sacrifice in photorefractive efficiency, with internal diffraction efficiencies of 72% and two-beam-coupling gain coefficients of 500 cm^{-1} being measured. A thorough analysis of the experimental data is presented, supporting the hypothesized mechanism of enhanced charge mobility without the

accompaniment of superfluous traps. It is anticipated that this approach can play a significant role in the eventual commercialization of this class of materials.

KEYWORDS

Photorefractive, Lead sulfide, Photoconductive, Triphenyldiamine, Nanocrystal, Fullerene.

1. INTRODUCTION

Owing to their large optical nonlinearities, low permittivity and low cost, organic photorefractive (PR) composites are potentially useful in a variety of real-time optical information processing applications including beam clean-up and amplification, dynamic interferometry, phase conjugation, and pattern recognition. [1-5]. Consequently, a great deal of research has focused on the development of this class of materials, resulting in substantial two-beam-coupling (TBC) as well as nearly 100 % diffraction efficiencies [3]. In addition to their notable performance, polymer-based PR composites are also attractive due to the ease with which their constituents may be independently modified, allowing the eventual combination to be tailored for a specific application. Ordinarily, PR composites are made up of a charge-transporting polymer matrix doped with a molecular non-linear optical (NLO) dye capable of modulating its refractive index under the influence of a space-charge field, often through a combination of a Pockels mechanism and the typically dominant birefringent effect.[6] It is also customary to include a photosensitizer which exhibits an electronic transition with energy corresponding to the wavelength, λ, of the optical radiation used to conduct the PR characterizations, resulting

in the production of free charge-carriers within the photoconductive (PC) matrix. Despite the flexibility associated with this approach, the lack of organic photosensitizers exhibiting sufficiently large photo-charge generation at specific λ, prevalent in many military and commercial applications, and the challenges associated with modifying the spectral characteristics of existing organic photosensitizers, proved to be a significant hurdle. It was largely this challenge which inspired the photosensitization of otherwise all-organic PR composites through the inclusion of semiconductor nanocrystals, also known as quantum dots or Q-dots. [7-21] The optical and electrical properties associated with Q-dots can be synthetically controlled due to an inverse correlation between the optical band-gap and the physical dimension of the Q-dots. [22] This relationship translates into a blue-shift in the absorption spectrum of a given material as its proportions are decreased beyond the dimensions of the Bohr radius specific to that material. The ability to readily manipulate the spectral features of Q-dots permits unprecedented control over the operational wavelength of the composite into which they are incorporated [7-10]. Although the photosensitization of PR composites through the inclusion of Q-dots was initially motivated by extending spectral range accessible to this class of materials, most studies have been conducted at established wavelengths, primarily $\lambda = 633$ nm, using Q-dots such as nano-sized CdS (QCdS) as well as QCdSe and QCdTe [7, 8, 10-15, 19]. In each case, careful synthetic procedures or size-selective purification techniques were employed to ensure the band-gap energy of the included Q-dots corresponded with that of the relevant experimental λ. Although far fewer examples exist, narrower band-gap semiconductor materials such as QPbS or QPbSe have been generally used for λ such as 1.31 μm and 1.51 μm [9, 16-18]. As before, efforts were

made to ensure that band-gap of the Q-dots coincided with λ. To date, the photosensitization of polymeric PR composites through the inclusion of Q-dots has been successful in extending the spectral sensitivity of these composites, however, reported efficiencies and response times have been substandard relative to those reported for PR composites photosensitized with more traditional organics, most notably C_{60}.

While photosensitization was the primary motivation for the incorporation of Q-dots into otherwise all-organic PR composites, a large amount of experimental data, particularly those from time-of-flight characterizations, indicate that in addition to acting a photosensitizer the included Q-dots increase the charge-carrier mobility, μ, within the PR composite [12]. This enhancement in μ is primarily attributed to the ability of the free charge-carriers to enter into, and subsequently be transported through the included Q-dots, where they experience a faster μ relative to that attributed to the conventional charge-transporting species which is typically polymeric. Not surprisingly, it has also been demonstrated that this improvement in the μ may be accompanied by a reduction in the PR response time, τ [19-21]. The ability to affect this parameter is particularly significant because it has been the slow τ associated with organic PR materials in general which has largely precluded them from numerous envisioned applications [3]. Notwithstanding the enormous insights gained into the fundamental processes of charge-generation and charge-transport occurring in inorganic-organic hybrid composites, there has existed an inability to capitalize on these understandings with, until recently, $\tau >$ 100 ms representing the best PR response time reported for an organic composite photosensitized with Q-dots. [19, 21] This τ is nearly two orders of magnitude larger than those reported for PR

composites photosensitized with organic photosensitizers such as C_{60} [23-32]. Furthermore, for studies involving visible λ, the data suggest that while the inclusion of Q-dots introduces a secondary charge-transport species imparting enhanced μ, they have also been shown to serve as a trapping species [19-21]. While a certain concentration and depth of traps is necessary for the PR effect, excessive trapping of positive free charge-carriers can have a detrimental influence over the response time, operational voltage as well as the overall diffraction efficiency in PR composites [1-3, 33]. In an effort to circumvent this issue, a recent study investigated the photosensitization of a PR composite at λ = 633 nm through the inclusion of QPbS where the QPbS exhibited significant, but off-resonance, absorption [21]. In this case the Q-dots exhibited a spectral feature associated with first excitonic absorption at ~1220 nm, significantly red-shifted from λ. In this study, it was hypothesized that while still constituting a trapping species, the QPbS, with its relatively narrow band-gap, would constitute considerably shallower traps than those associated with Q-dots possessing significantly larger band-gaps. By all accounts, shallower traps would have a less detrimental effect over the PR performance, allowing free charge-carriers to travel, on average, a longer distance before encountering a terminal-trap, thus optimizing the phase shift between the dynamic space-charge field and the interference pattern associated with the writing beams. Moreover, the lack of deep traps encountered along the way, even if not terminal in nature, should decrease the time required to attain the dynamic equilibrium of charge distribution composing the space-charge field. This approach proved to be largely successful, resulting in $\tau \lesssim 40$ ms and diffraction efficiencies comparable to those observed in all-organic PR composites. In a separate study it was established that by exchanging the relatively wide band-gap

QCdSe with QCdTe, which possesses a comparatively narrower band-gap, an improvement in the τ was realized [19]. These studies provided strong evidence that although the direct photosensitization of PR composites through the inclusion of Q-dots had much potential especially with regard to extending the operational spectral range, Q-dots may alternatively be used specifically for enhancing the charge-carrier μ, substantially reducing the τ of a PR composite.

In this communication we present a novel PR composite specifically formulated to exploit the insights gained with regard to the influence of Q-dot inclusion over charge-carrier μ and reduction in τ. Initial work focused on the development of the composite with the optimization of τ being the primary consideration in this process. The vast majority of organic PR composites described in literature use poly(*N*-vinylcarbazole) (PVK) due to its efficient hole-transporting capability. The exceedingly high glass transition temperature, T_g, of PVK, however, dictates the need for the inclusion of a plasticizer so that the NLO dye may reorient within the established space-charge field at ambient temperatures. Plasticization usually involves the inclusion of a comparatively inert species such as tritolylphosphate (TCP) or *N*-ethylcarbazole (ECZ) which does not significantly contribute to any of the essential processes required for the PR effect. More recently PR composites based on polymers which replace the charge-transporting carbazole group with that of triphenyldiamine (TPD), or similar structures, have been described [25-32]. Of these polymers perhaps the most notable is poly(acrylic tetraphenyldiaminobiphenyl) (PATPD) which is composed of a TPD molecule attached to acrylic backbone through a pendant linkage [27, 29. 30-32]. Due to the enhanced charge-carrier, μ associated with polymers functionalized with TPD in conjunction with a

valence-band lower in energy than that associated with PVK, greater efficiencies and faster τ have also been reported. Unfortunately, the T_g of the TPD-functionalized polymers is also well above the ambient temperature, and therefore must be lowered through the addition of a relatively inert plasticizer, typically ECZ. Moreover, in pendant geometry, the TPD group which is solely responsible for charge-transport needs to be attached to an inert backbone as well as an inert pendant linkage, adding to the ineffectual volume of the PR composite. The use of a polymerized form of TPD was long considered necessary due to the propensity of molecular forms of TPD to crystallize in the solid solution of the PR composite, greatly diminishing the optical quality of the PR device as well as its ability to withstand the comparatively high external electric field, *E*, required to elicit an appreciable PR response. In this communication, it will be demonstrated that through a judicious choice of functional groups attached to the TPD molecule, in conjunction with the appropriately chosen co-components, mixed in the proper ratio, it is possible to formulate a PR composite where a molecular form of TPD acts as the primary organic charge-transport species. Through this approach, the inert backbone as well as the pendant linkage associated with polymerized forms of TPD can be eliminated, greatly increasing the loading content of the active components and thereby improving the PR performance. Furthermore, it will be established that this approach affords a composite which does not require the addition of an inert plasticizer to elicit the desired birefringence associated with the reorientation of the NLO dye within the soft matrix. This too allows for a greater loading of active components.

In addition to the charge-transporting molecular TPD, the composite described herein also contains the NLO dye 4-homopiperidinobenzylidenemalononitrile (7-DCST)

providing the electro-optic activity required for the PR effect [24]. 7-DCST has been used in conjunction with PVK as well as PATPD and is a common choice of NLO dye for PR composites in which the optimization of τ is of interest [23, 24, 29-32]. Solid phase crystallization of the molecular TPD as well as that of the 7-DCST, also well known for its susceptibility to phase-separation, was successfully suppressed through the inclusion of a small amount of polymer. Rather than employ a functionally passive polymer, it was found that PVK in concentrations as low as 10 wt% was especially effective at preventing any aggregation of the molecular constituents. Since the primary goal of this study was to study the performance of a PR composite in which the charge-carrier μ is enhanced through the inclusion of narrow band-gap Q-dots, there was no need for the Q-dots to perform as the photosensitizer as in most of the previous studies involving the inclusion of Q-dots in an otherwise all-organic PR composite. This, in conjunction with the experimental λ = 633 nm, permitted the use of C_{60} as the photosensitizer in the current study. Data reveal that this approach, featuring a molecular derivative TPD void of any Q-dots, results in PR composite whose performance rivals those reported for composites utilizing PVK or any polymerized form of TPD with τ = 2.4 ms, external diffraction efficiencies, η_{ext}, of 63 % and two beam coupling gain coefficients of 510 cm^{-1}.

To study the enhancement of the τ as a result of the inclusion of narrow band-gap Q-dots, QPbS was introduced into the previously described composite at various concentrations. The Q-dots were synthesized through a well-established high-temperature approach utilizing oleic acid (OA) and 1-octadecene (ODE) as the capping groups and reaction solvents, respectively [34]. The synthetic procedure resulted in QPbS with a diameter of ~ 6nm corresponding to a band-gap of ~ 1.02 eV, relatively narrow in

comparison to λ = 633 nm (1.96 eV). It will be demonstrated that the inclusion of the QPbS in the previously described composite resulted in a decrease in τ by a factor of 6, to τ = 400 μs, the fastest τ reported for PR composite under CW conditions. This significant decrease in τ is especially exciting due to the ability to avoid the detrimental effect over PR efficiency, with η_{ext} decreasing by only 4%, to 59 %, as a result of introducing the QPbS into the composite.

To characterize the performance of the composites, time-resolved DFWM, TBC, visible absorption spectroscopy, and conductivity experiments were employed, the results and implications of which will be presented. In addition to the insights gained into the fundamental mechanisms relevant to this class of materials, a significant advancement in PR performance is realized, with τ decreasing to 1/6 the value observed in the similar composite which does not containing QPbS. A maximum internal diffraction efficiency, η_{int}, of 72%, as well as TBC gain coefficients, Γ, of 500 cm^{-1} have been measured for the composite containing QPbS. It is clear that the inclusion of QPbS results in a substantial decrease in τ without significantly affecting η and Γ. Furthermore, it is believed that these qualify as some of the best figures-of-merit recorded for any organic PR composite. It is anticipated that the advances illustrated herein represent significant progress towards the eventual practical application of PR composite materials.

2. EXPERIMENTAL SECTION

All chemicals were obtained from Aldrich and used as received unless otherwise noted.

2.1. Synthesis of QPbS. This procedure is based on a report found in the literature [34]. Briefly, a reaction flask was charged with 0.18 g of PbO and 4 mL and OA. This solution was degassed under vacuum and mechanically stirred for 3 hr at 80° C. In a separate flask purged with nitrogen, 0.084 mL of hexamethyldisilathiane (TMS) were dissolved in 2 mL of ODE and subsequently degassed under vacuum at RT for 1 hour. The temperature of the previously prepared lead oleate solution was raised to 150° C and the TMS/ODE solution was quickly injected into the reaction flask. The reaction was observed to turn brown to black, at which time it was quenched with an ice bath. The QPbS was stored in this solution until used in the fabrication of PR devices. At this time, the temperature of the original reaction mixture was raised to 60 °C and 10 mL of methanol were injected. Upon reaching RT, the mixture was centrifuged to collect the QPbS which was then redispersed in toluene. Additional methanol was added, the mixture centrifuged and QPbS collected again. This purification procedure was repeated several times to remove any unreacted OA, TMS, and ODE. To remove unreacted PbO, the product was dispersed in toluene, centrifuged and the supernatant was collected. It is noted that previous studies have shown that by exchanging the aliphatic ligands which are associated with the surface of the Q-dots, and assumed to be effectively insulative, with ligands having conjugated or aromatic structure, the process of charge-transfer between the charge-transporting polymer and the Q-dot can be significantly enhanced [7, 8, 20]. Therefore an attempt was made to exchange the OA ligands associated with the QPbS for pyridine. In this case, however, due to the rapid aggregation of the QPbS following ligand exchange, the effect of this procedure was not part of this study. The QPbS were characterized using visible absorption spectroscopy and the absorption

spectra of the QPbS nanoparticle suspensions were obtained in toluene using a 1 cm quartz cell. The QPbS were also characterized via thermal gravimetric analysis (TGA) using a TA Instruments TGA 2950, run at ramp-rate of 20 °C/min in air. TEM pictures were acquired using a Philips EM430T Scanning Transmission Electron Microscope with carbon-coated grids.

2.2. PR Composite Devices. N,N-Bis(3-methylphenyl)-N,N-bis(phenyl)benzidine (DMTPD) was obtained from Magical Scientific USA and purified by recrystallization in hot CH_2Cl_2 prior to use. 7-DCST was synthesized in our lab according to a procedure in the literature [24]. For the composite samples, PVK (secondary standard), TPD, 7-DCST and the appropriate quantities of capped QPbS and C_{60} were dissolved in toluene and, after thorough mixing, filtered to remove any undissolved solids. This solution was stored in a vacuum oven at 50° C for 24 hours to remove the solvent. The solid residue was subsequently recovered, placed between two pieces of glass coated with indium tin oxide and heated above its melting temperature on a hot-plate. The sample was then mechanically pressed forming the typical "sandwich" geometry using glass spacers to control the thickness of the device, d, at 100 μm.

Although many compositions were considered, the results for a total of four devices will be presented here. For these PR devices, the TPD:7-DCST:PVK wt% ratio was held constant at 45:45:10 respectively. The first PR device contained only these components, constituting a control device and is herein referred to as D0. The second device contained these components in this ratio as well as being photosensitized through inclusion of 0.200 wt % of C_{60}. This device is referenced as DC60. A third PR device was

fabricated nearly identical to the second with the exception of the addition of 0.223 wt% of QPbS. It is noted that this wt% includes both inorganic PbS as well as the organic capping groups. This device is referred to as DC60PBS. Finally a fourth PR device was fabricated which was identical to the third, with the exception that the C_{60} was not included. This device was fabricated so that the effect of the QPbS over the charge-generation process could be isolated and is referred to as DPBS. To determine the weight percentage of QPbS in each composite, several QPbS:solvent solutions of known absorbance and volume were evaporated to dryness and the mass of the solid residue was measured. It is noted that this residue includes the inorganic PbS as well as the organic passivating layer. The weight percent of QPbS in each device was thus calculated indirectly from the known absorbance and volume of the aliquot used in the fabrication of the respective composite. The compositions and the spectroscopically measured α_{633} of all devices are presented in Table 1. The PR devices have not shown any change in their optical properties or degradation in PR performance over the course of 12 months. All UV-Vis absorption spectra were recorded on a Beckman DU 640B spectrophotometer.

2.3. PR Characterizations. The PR properties of the composite devices were studied via TBC and temporally resolved DFWM techniques using a standard tilted geometry [3]. Holographic gratings were written through the intersection of two coherent beams generated by a helium-neon (HeNe) laser operating at 633 nm with incident angles of $\theta_1 = 45°$ and $\theta_2 = 75°$ (in air) relative to the sample normal. In the TBC experiments, both writing beams were *p*-polarized with intensities of $I_1 \approx 0.05$ mW and $I_2 \approx 8$ mW. The external bias was applied such that I_1 would experience gain at the expense of I_2. Asymmetric energy transfer was observed by monitoring the intensities of the writing

beams after the PR device with a photodiode. In the DFWM experiment the writing beams were *s*-polarized with intensities of $I_1 \approx 3$ mW and $I_2 \approx 9$ mW. In addition, a *p*-polarized probe beam propagated in a direction opposite to I_1 with an intensity of $I_p \approx 2 \times 10^{-3}$ mW. Through the use of a polarizing beam splitter placed in the path of I_2 in conjunction with a photodiode, the diffracted portion of I_p, also referred to as the signal beam, I_s, could be quantified. In all PR experiments, I_1 and I_2 had beam diameters of ~ 280 μm while I_p possessed a beam diameter of ~ 120 μm. Beam diameters were measured by using a fractional irradiance of $1/e^2$.

The Γ, was determined in terms of the experimentally measured quantities γ and β, as

$$\Gamma = \left[\ln(\gamma\beta) - \ln(\beta + 1 - \gamma)\right]/L, \quad (1)$$

where L is the path length of the beam experiencing gain inside the sample, β is the ratio of the writing beam intensities before the sample, and γ is the ratio of the intensity of the beam experiencing gain with and without the pump beam. The η_{int} were quantified according to the equation

$$\eta_{int} = I_s / I_{p'}, \quad (2)$$

where $I_{p'}$ is the intensity of the probe beam after the device with no bias applied. Similarly, the η_{ext}, accounting for reflections, were determined according to the equation

$$\eta_{ext} = I_s / I_p . \tag{3}$$

Time resolved DFWM techniques were used in the quantification of the τ. For this experiment, E was applied to the device while blocking one of the writing beams. The device was permitted to settle for approximately 30 s and the blocked writing beam was unblocked. The diffracted portion of the probe beam was then recorded as a function of time, t. The determination of the τ was accomplished by fitting the data obtained in DFWM experiments to an equation of the form

$$\eta(t) = \sin^2\{A[1 - m\exp -t/\tau_f - (1-m)\exp -t/\tau_s]\}, \tag{4}$$

where A is a fitting constant, m is a weighting ratio, τ_f is the fast time constant and τ_s is the slow time constant. For the fitting, all four variables were allowed to float.

Photoconductivity, σ_p, characterizations were made using a dc-photocurrent technique with a Keithley electrometer used to measure the current passing through the sample as a function of E. The beam intensity for all σ_p characterizations was ~ 10 mW with a beam diameter of 0.98 mm. This technique also permits the measurement of the dark conductivities, σ_d, associated with the PR devices. To measure the dark conductivity, σ_d, an E was applied and the current was allowed to reach a steady state. To measure the

σ_p, the sample was initially illuminated for several minutes followed by the application of the E and the current was allowed to achieve a steady state (typically ~ 5 min). In calculating the σ_p, the dark current density was subtracted from the photocurrent density. For calculations involving the photocurrent density, the diameter of the laser was employed, and for those related to the dark current density, the area of electrode overlap was used. These data were calculated using the equation

$$\sigma = J/E, \tag{5}$$

where J is the experimentally determined current density.

In an From the σ_p data it is possible to determine the internal charge-generation quantum efficiencies, Φ, of the photosensitizer using the equation

$$\Phi = \frac{N_{cc}}{N_{ph}} = \frac{\sigma_p hcE}{Ie\lambda\alpha_\lambda d}, \tag{6}$$

where N_{cc} is the number of charge-carriers generated per unit volume, N_{ph} is the number of photons absorbed per unit volume, h is Plank's constant, c is the speed of light, and e is the fundamental unit charge.

3. RESULTS AND DISCUSSION

The goal of this study was to examine the feasibility of using Q-dots to affect charge-carrier μ in a PR composite so as to improve the τ without detrimentally affecting PR efficiency of the composite. The first objective to these ends involved the choice of semiconductor material and was made based on the results of many studies, but several in particular [19-21]. It must be noted that in all previous studies concerning the inclusion of Q-dots into a PR composite, the Q-dots were included to serve as the photosensitizer. It was during these studies that data began to indicate that in addition to creating free charge-carriers within the PC matrix, the Q-dots were also enhancing the τ of the PR composites. It was soon speculated that this enhancement in τ was attributable to the faster charge-carrier μ associated with inorganic semiconductors as compared to the organic matrix, typically PVK. The earliest definitive evidence of charge-carrier μ being enhanced through the inclusion of Q-dots in to a PC polymer came in a study in which QCdS was doped into a thin film of PVK [12]. Using time-of-flight experimental techniques, it was shown that inclusion of QCdS in a PVK matrix exhibited a faster charge carrier μ than in pure PVK. Moreover, it was demonstrated that the μ scaled with Q-dot concentration.

Despite these promising results, there was also indication that the Q-dots could play a third role in addition to photocharge-generator and charge transport species, that of a charge trapping species. Although a certain concentration and depth of charge traps are required for the PR effect, traditionally impurities and imperfections associated with the polymer have effectively addressed this requirement, and a separate species is not usually

included to act as trapping species. For the case of Q-dots, data indicate that their propensity to act as charge traps can have a detrimental influence over the efficiency of a PR composite into which they are included. In an effort to overcome this hindrance, recent work has focused on the use of Q-dots with a narrower band-gap [21]. These studies have demonstrated the ability to photosensitize a PR polymeric composite with QPbS where, unlike in the majority previous studies, the QPbS had a band-gap energy (1.02 eV) which was considerably less than that associated with the optical radiation employed in the PR characterizations (λ = 633 nm, corresponding to 1.96 eV). Here it was demonstrated that using the relatively narrow band-gap QPbS resulted in τ = 34 ms, which is among the fastest reported for a polymeric PR composite photosensitized with Q-dots, as well as for polymeric PR composites in general. In addition, this τ was achieved without sacrificing efficiency, as indicated by the η_{int} = 83 % reported for this PR composite. Based on these results, it was determined that QPbS would serve as the Q-dot used in the current study. It is noted that the QPbS used in the current study originate from the same batch as those used in this cited work [21].

TEM was employed and the image obtained for QPbS is presented in Fig. 1. The particles are irregularly shaped, but approximately spherical in character. Using only particles which appeared not to be part of an aggregate, the mean diameter was determined to be 3.62 ± 0.58 nm (N = 40). The relatively small standard deviation is reflective of the monodispersity associated with the QPbS. The absorption spectrum of the QPbS dispersed in toluene is depicted in Fig. 2. Evident in the figure is that the absorption associated with the first exciton occurs at ~1220 nm, corresponding to a band-gap of 1.02 eV. This is compared to the value of 0.37 eV for bulk PbS, clearly

demonstrating the effect of quantum confinement [35]. It is additionally apparent that at a normalized concentration of 1 mg/mL, the QPbS exhibits an absorption coefficient of α_{1220} = 0.0296 cm^{-1} at this wavelength. The same concentration of QPbS possesses α_{633} = 0.234 cm^{-1}, nearly an order of magnitude larger than α_{1220}. The presence of the well-defined peak at ~1220 nm indicates a high degree of monodispersity.

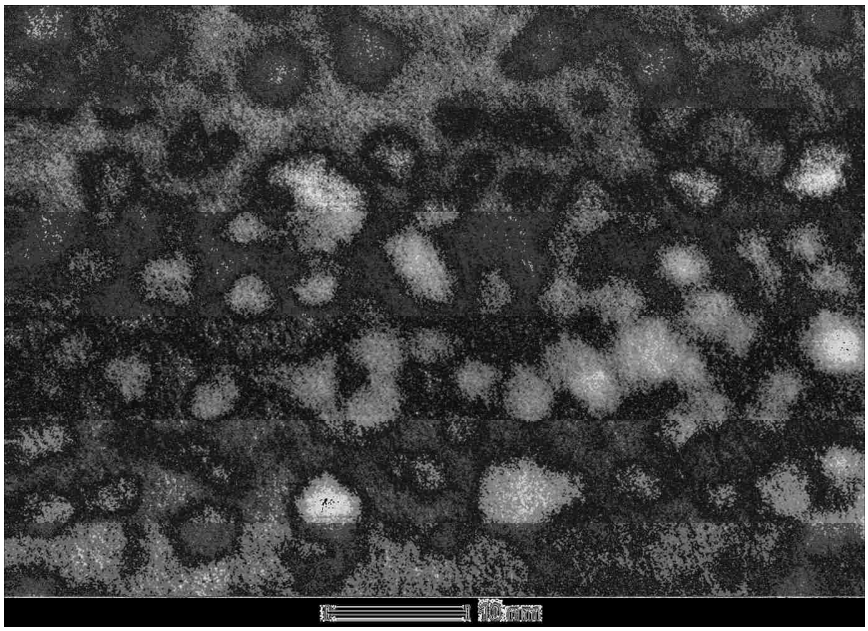

Figure 1. TEM image of PbS quantum dots.

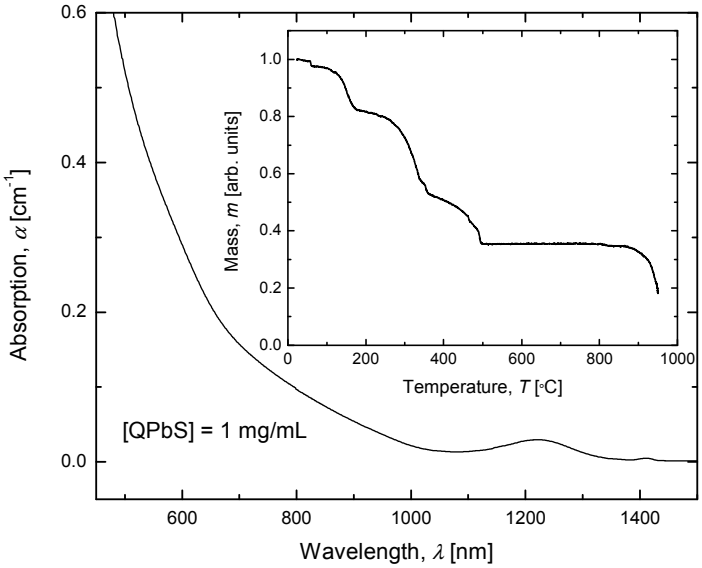

Figure 2. Visible absorption spectrum of QPbS in toluene. The inset depicts the TGA data obtained for the QPbS.

As detailed in the experimental section, attempts to conduct ligand exchange on the QPbS were unsuccessful and therefore the as-synthesized QPbS were used in the remainder of this study. In order to quantify the ratio of organic capping material to inorganic PbS present in the QPbS, TGA was conducted, the results of which are presented in the inset of Figure. 2. Apparent from the figure is that ~ 2-3 wt% of the QPbS is lost at ~ 60° C. Although the sample was dried under vacuum at room temperature prior to analysis, this initial loss can likely be attributed to residual solvent, primarily toluene in this instance. Subsequent to this feature, it is observed that organic components are lost in three distinct phases until ~ 500° C is attained. The first loss phase terminates at ~ 170° C and it is not immediately clear as to the composition of the

component lost during this phase. The second loss phase terminates at 360° C, the boiling point of OA, and can therefore likely be attributed to the loss of OA which is loosely associated with the inorganic PbS. The third and final loss phase terminates at ~ 500° C and although experimental proof is wanting, can expectedly be attributed to OA which is covalently associated with the surface of the inorganic PbS nanocrystal. Subsequent to ~ 500° C, a constant mass is observed until ~ 850° C is achieved. It is this mass which is attributed to the inorganic PbS, and accounts for 33.6 wt% of the QPbS used in the PR composites.

The next objective in this study was the formulation of the organic components constituting the PR composite. Because this study is largely concerned with the PR τ, it was this parameter which motivated the choices made in this regard. Perhaps the most influential component over the PR τ is that of the charge-transporting species. This requirement is most often fulfilled through the inclusion of a PC polymer, with PVK being the most prevalent. More recent research indicates, however, that PR composites which contain TPD as the charge-transporting moiety exhibit superior PR performance compared to their PVK counterparts, attributed in part to a faster charge-carrier μ associated with TPD [25-29, 30-32]. The superior performance associated with TPD-based composites, can also be traced to the relationship among the various highest-occupied-molecular-orbitals (HOMO) associated with the components, especially when used in conjunction with certain NLO dyes [27]. Specifically, TPD is more easily ionized than is PVK since the HOMO of TPD lies higher in energy at approximately – 5.4 eV, than that of PVK which occurs at – 5.92 eV. Furthermore, when PVK is used in

conjunction with certain NLO dyes, such as 7-DCST which has a HOMO occurring at −5.9 eV, it is energetically favorable for the positively charged holes to become trapped at a 7-DCST molecule, whereas in the case of TPD this issue is avoided [27].

The TPD-based PR composites typically contain polymers in which the TPD is either part of the polymer backbone or alternatively as a pendant unit grafted to a polymer backbone. When employed in the pendant geometry as in PATPD, TPD-based PR composites have exhibited τ = 10 ms with η_{int} = 80% under CW conditions. These figures-of-merit are remarkable, especially considering that PATPD is 78.9 wt % TPD, with the remainder of the mass being attributable to the polymer backbone and pendant structure, which is essentially inert with respect to the PR process. Furthermore, PATPD has a T_g well above RT, dictating the need to include an also inert plasticizer allowing for the orientational mobility of the NLO dye. There are also questions as to whether the TPD pendants are able to achieve the optimal stacking conformation which is conducive to the hopping mechanism of charge-transport ubiquitous to these types of PC materials. Faster τ have been reported for other PR composites utilizing polymerized forms of TPD, however these fast τ often come at the expense of efficiency. Several studies exist in which τ as fast as 1-3 ms are reported, though diffraction efficiencies were either not reported or did not exceed 0.5% [25, 28]. To date, a sub-millisecond τ has not been reported for a PR composite characterized under CW conditions. A sub-millisecond of τ = 300 μs has been described for a PR composite characterized under pulse conditions [32].

Based on these considerations, we attempted to formulate a PR composite rooted in a molecular form of TPD. Nevertheless, polymeric forms of TPD are typically

employed due to the very large propensity for TPD, as well as its various molecular derivatives, to crystallize within the solid solution of the PR composite. After screening a substantial number of TPD derivatives in conjunction with several NLO dyes as well as selected organic photosensitizers, it was established that a PR composite, stable against aggregation of any components for at least 12 months up until now, could be achieved using the DMTPD derivative of TPD as the PC species. Although fraught with a pair of methyl groups to aid in phase stability, this is a relatively small cost in terms of additional inert mass. As will discussed in greater detail, this allowed for ~ 45 wt% loading of DMTPD, a relatively high concentration that is favorable for charge-carrier μ. The lack of a need for a plasticizer is another significant benefit associated with the use of molecular DMTPD. In addition to the DMTPD, a relatively small amount of PVK totaling ~ 10 wt% was introduced to assist in phase stabilization. Although difficult to confirm, it is likely that charge-transport occurs in the PVK as well as the DMTPD, and as such the PVK may not be inert with regard to the PR process. However, based on the HOMO considerations, a positively charged hole is lower in energy when associated with DMTPD than when with PVK, and as such, once a hole becomes associated with DMTPD, it is unlikely to re-associate with the PVK.

To impart NLO activity to the PR composite, 7-DCST was employed as it has been in many recent studies which have highlighted the PR τ [23, 24, 29-32]. The PR composites described herein contained ~ 45 wt% 7-DCST which is similar to concentrations employed in previously described PR composites. The photosensitizer used in the current study was C_{60} and is well known to be one of the most efficient PR photosensitizers for λ = 633 nm. With a HOMO occurring at – 6.40 eV, C_{60} can also

behave as a trapping species within the PR medium. In previous studies C_{60} has been used for this function in a range of concentrations, but typically on the order of 0.2 – 2.0 wt%. In this study C_{60} was included at 0.2 wt% which is a relatively low concentration. Although attempts were made to increase the C_{60} concentration in an effort to improve the PR performance, it was observed that unlike DMTPD and 7-DCST, C_{60} exhibited a very high susceptibility to aggregation within the PR composite at higher concentrations. The resulting PR device is referred to as DC60PBS and its composition is detailed in Table 1.

Table 1. Compositions and α_{633} of the photorefractive devices used in this study.

Device	C_{60} (wt%)	QPbS (wt%)	DMTPD (wt%)	7-DCST (wt%)	PVK (wt%)	α_{633} (cm^{-1})
DC60PBS	0.199	0.223	44.8	44.8	9.96	8.04
DC60	0.200	NA	44.9	44.9	9.98	7.81
DPBS	NA	0.223	44.9	44.9	9.98	2.75
D0	NA	NA	45.0	45.0	10.0	2.46

As described in the Experimental section several control devices were also fabricated and their compositions are also detailed in Table 1 as well as the α_{633} for the relevant devices. The absorption spectra of the devices employed in this study are provided in Figure 3. The device void of C_{60} and QPbS, D0, exhibits $\alpha_{633} = 2.46$ cm^{-1} whereas the addition of 0.223 wt % of QPbS, as in the DPBS device, increased the α_{633} by 0.29 cm^{-1}. Similarly, the addition of 0.200 wt % of C_{60}, as in DC60, resulted in an

increase in α_{633} of 5.35 cm^{-1}. Finally, in the DC60PBS device, the presence of both C_{60} and QPbS at concentrations commensurate with those of the control devices produced an increase in α_{633} by 5.58 cm^{-1}.

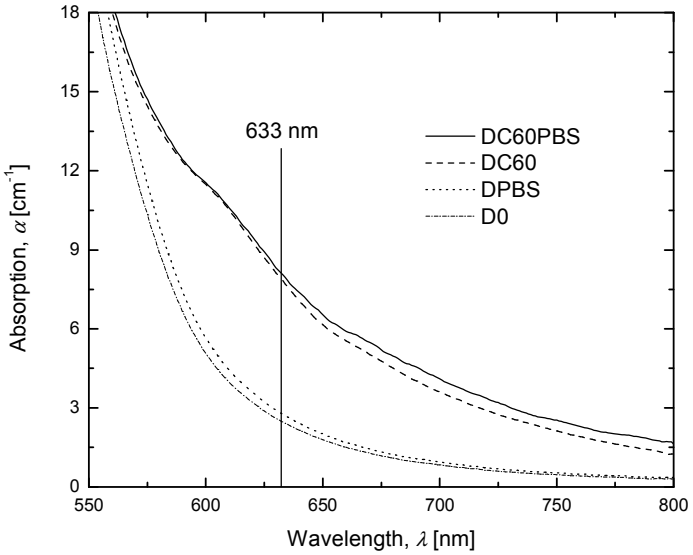

Figure 3. Visible absorption spectra of the PR devices used in this investigation; DC60PBS (solid line), DC60 (dashed line), and DPBS (dotted line).

For the DC60PBS device, C_{60} is intended as the primary sensitizer, however, QPbS, included for purposes of enhanced charge transport, has also been shown to photosensitize similar composites with λ= 633 nm. In an effort to distinguish between the effects of the respective potential photosensitizers as well as to gain insight in the fundamental physical processes occurring in these materials, the σ_p and σ_d were measured for each device and are shown as a function of *E* in Figure 4. Looking first at

the σ_d, it is observed that this parameter is nearly constant for all devices across the entire range of investigated *E*. While somewhat surprising, it indicates that the presence of C_{60} and/or QPbS does not have a significant effect on the σ_d. Because conductivities in general, σ, depend explicitly on mobility as

$$\sigma = pe\mu, \tag{7}$$

where *p* is the density of mobile charge carriers (holes) and *e* is the fundamental electric charge, it can be assumed that the unilluminated QPbS does not enhance charge carrier mobility under these conditions. This situation is favorable for the PR effect because the

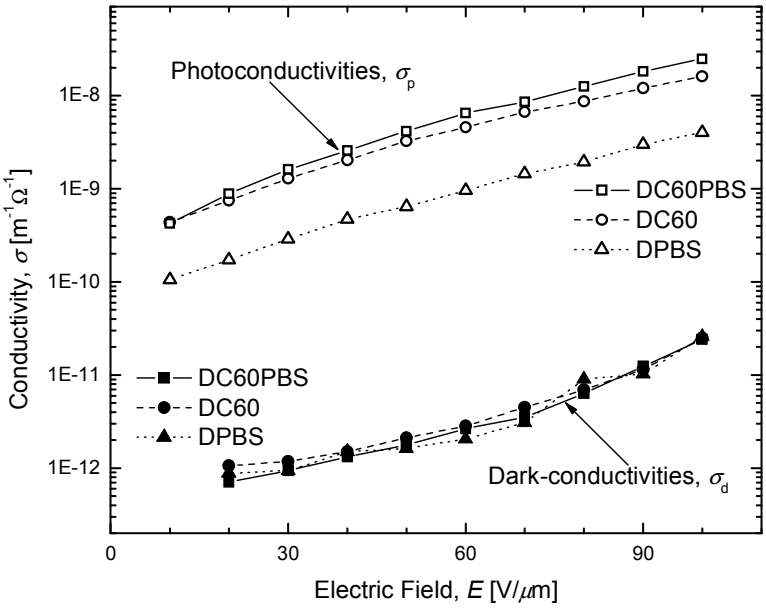

Figure 4. Electric field dependence of the photoconductivities, σ_p, (open symbols) and dark-conductivities, σ_d, (filled symbols) of DC60PBS (squares), DC60 (circles), and DPBS (triangles) at λ = 633 nm. The lines are guides for the eye.

establishment of a space charge field depends on large ratio of σ_p/σ_d. Turning to the σ_p, it is apparent from the figure that the DC60PBS device exhibits the best performance in this regard. This is not surprising since this composite contains both C_{60} and QPbS. The DC60 device shows a slightly diminished σ_p relative to that of the DC60PBS device. This is again expected since DC60, though void of QPbS, still contains the primary photosensitizer, C_{60}. These data evidence the ability of QPbS to act as a significant photosensitizer. The DPBS device, although decreased by nearly an order of magnitude relative to the DC60PBS device, still exhibits a significant increase σ_p relative to its σ_d, again demonstrating the ability for QPbS for photosensitize this composite, though significantly less effectively than that of the C_{60}. It is noted that for this study the concentration of QPbS was chosen so as to optimize the τ of the DC60PBS device and not the σ_p of the DPBS device, and therefore it is not possible to draw a direct comparison of the photosensitization ability between the QPbS and C_{60} from these data. The DC0 device did not exhibit a measurable σ_p.

From the σ_p it was possible to determine Φ for the relevant devices and are presented as a function of *E* in Fig. 5. The Φ are surprisingly similar for all compositions. The Φ of the DC60 device does consistently exceed that of the DPBS device, suggesting that C_{60} provides somewhat superior photosensitization relative to that of QPbS in this composite. The strikingly similar performance, however, indicates that with further optimization, the Φ of QPbS, or some similar material, may exceed that of C_{60}. It is also observed that the Φ of the DC60PBS device slightly exceeds that of the DC60 device. Because the DC60PBS device contains both C60 and PbS, to a first approximation, the Φ

should be intermediate between that of DC60 and that of DPBS. The reason for this observation is not immediately apparent but may indicate an as of yet unknown synergistic effect between the QPbS and the C_{60}. The available data do not warrant further speculation.

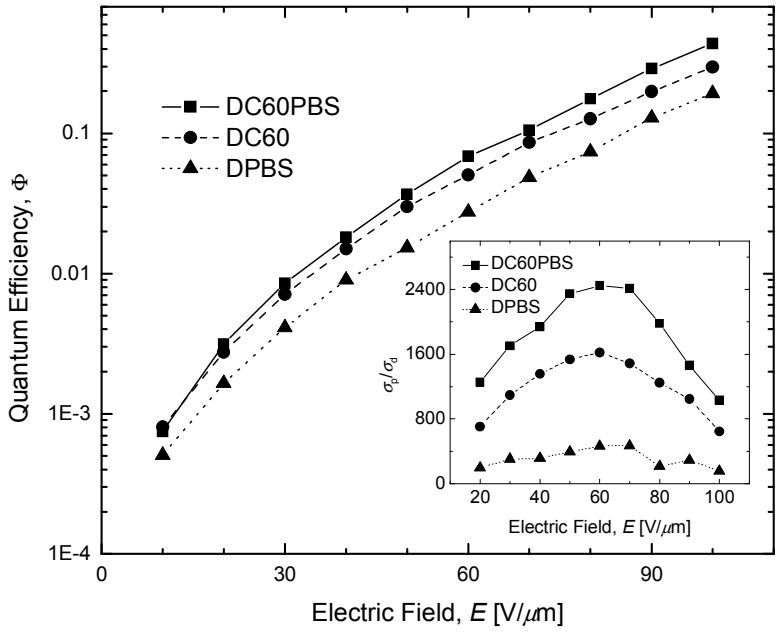

Figure 5. Electric field dependence of the quantum efficiencies, Φ, for DC60PBS (squares), DC60 (circles), and DPBS (triangles) at $\lambda = 633$ nm. The lines are guides for the eye. The inset depicts the electric field dependence of the ratio of photoconductivity to dark conductivity, σ_p/σ_d, for the same PR devices at $\lambda = 633$ nm. The lines are guides for the eye.

In addition to the fundamental insights gained from the σ data, they may also provide an indication as to the potential PR performance. This is because the magnitude of the PR space-charge field, $|E_{SC}|$, is related to the ratio σ_p/σ_d as dictated by the equation

$$\left|E_{SC}\right| = m \cdot E_q \cdot \left[\frac{E_0^2 + E_d^2}{E_0^2 + \left(E_d + E_q\right)^2}\right]^{1/2} \cdot \frac{1}{1 + \sigma_d/\sigma_p}, \quad (8)$$

where m is the depth of modulation, E_0 is the is the component of E which coincides with the grating vector, E_q is the magnitude of the trap-density-limited space-charge field, and E_d is that of the diffusion field [23]. The σ_p/σ_d data are presented as a function of E in the inset of Fig. 5. Interestingly, the functional form of the data is highly reminiscent of those for other Q-dot photosensitized PR composites, with σ_p/σ_d reaching a maximum at an intermediate E [18, 19]. However, the device photosensitized with only C_{60}, DC60, also shows a similar trend, indicating that this behavior is not unique to composites photosensitized with Q-dots. For the DC60PBS device, the σ_p exceeds the σ_d by more than three orders of magnitude, indicating its potential as an efficient PR composite.

A distinct characteristic feature of the PR effect is that the refractive index grating created in the medium is spatially shifted with respect to the light intensity pattern of the writing beams [22]. As a result, an asymmetric exchange of energy occurs between beams interfering in a PR medium. The PR nature of the gratings created within the composites used in this study was confirmed using conventional TBC experiments. The Γ is presented as a function of E in Fig. 6 for the relevant devices. Apparent from the figure is that DC60PBS, DC60, and DPBS exhibit nearly identical Γ across the entire range of E investigated. Because the Γ is highly dependent upon the phase shift between the illumination pattern and that of the internal space-charge field, which in turn is highly

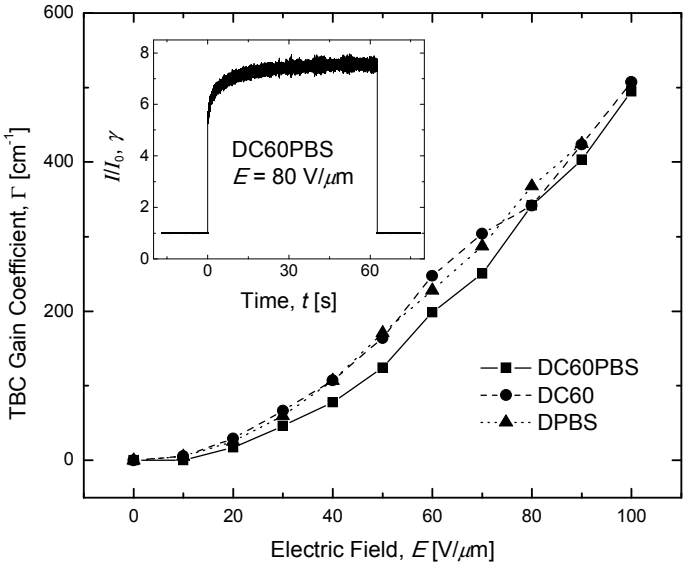

Figure 6. Electric field dependence of the TBC gain coefficient, Γ, for DC60PBS (squares), DC60 (circles), and DPBS (triangles) at $\lambda = 633$ nm. The lines are guides for the eye. The inset depict the temporal evolution of the experimental quantity γ for DC60PBS with $E = 80$ V/μm.

dependent upon the concentration of reasonably deep traps, it can be assumed that the concentration of such deep traps does not vary significantly among the various compositions. This reinforces the hypothesis that narrow band-gap Q-dots have a reduced propensity to act as deep traps in these PR composites relative to their wider-band-gap counterparts. The magnitude of Γ is also noteworthy with DC60 exhibiting $\Gamma = 510$ cm^{-1}, and DC60PBS showing a slightly diminished $\Gamma = 500$ cm^{-1}, both at $E = 100$ V/μm. Although the DPBS device experienced dielectric breakdown prior to 100 V/μm, it still showed $\Gamma = 420$ cm^{-1} at $E = 90$ V/μm. For practical applications the condition $\Gamma > \alpha$ should be met for a given device. Due to its relatively small α_{633}, DPBS meets this

condition at E as low as 10 V/μm. For DC60 and DC60PBS, their Γ exceeds their respective α_{633} prior to 20 V/μm. Remarkably, these figures-of-merit are among the best reported for any PR material. The inset in Fig. 6 depicts the optical amplification factor, γ, as a function of t for the DC60PBS device at E = 80 V/μm and provides qualitative insight into the temporal characteristics associated with the TBC in these composites.

Having established the PR nature of the observed gratings, the η_{int} were evaluated. These data are presented as a function of E in Fig. 7. In this figure the solid lines represent the best fit of the data to a simple sine-squared function as predicted by theory [33]. Although the fits are wanting, an over-modulation E where η_{int} achieves a maximum is clearly observed for all three devices. For DC60PBS and DC60 this occurs at E ~ 50 V/μm and for DPBS at E ~ 40 V/μm, which are typical values for organic PR composites. Moreover, there exists a subsequent minimum in η_{int} for DC60PBS and DC60 at E ~ 90 V/μm and for DPBS at E ~ 80 V/μm. With η_{int} = 75 %, it was the DC60 device which exhibited the highest internal efficiency at it over-modulation E, however, the addition of the QPbS in the DC60PBS device lowered the efficiency only slightly to 72 % at the same E. It is central to this study that the diffraction efficiency is maintained in the presence of the QPbS.

The performance of the DPBS was far inferior with η_{int} = 9.5 % at its maximum. However, it is again noted that the composition of this sample was not optimized for performance and is only for comparison purposes, and other studies employing the same QPbS species at higher concentrations in similar composites have shown significantly higher diffraction efficiencies [23].

While the η_{int} are fundamentally important, it is the η_{ext} which are of functional significance and are depicted as a function of E in Fig. 8. As in Fig. 7, the solid lines represent the best fit of the data to a simple sine-squared function. Due to their relatively high η_{int}, in conjunction with their reasonably low α_{633}, the DC60 and DC60PBS devices also exhibit a favorable η_{ext} at their over-modulation E, with η_{ext} = 63 % and η_{ext} = 59 %, respectively. These η_{ext} indicate the potential application of the composites.

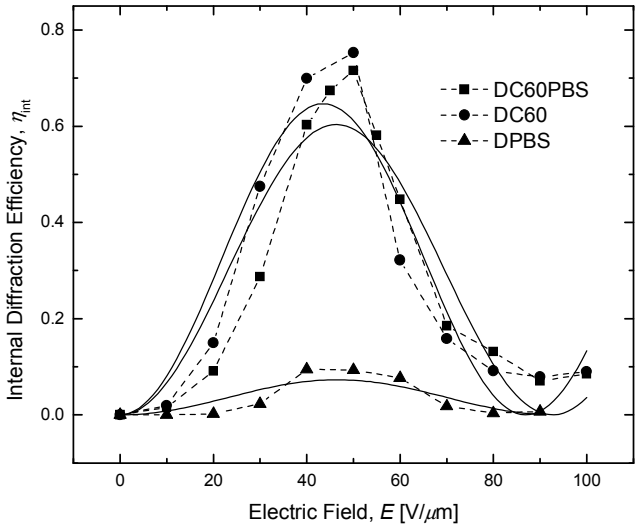

Figure 7. Electric field dependence of the internal diffraction efficiencies, η_{int}, for DC60PBS (squares), DC60 (circles), and DPBS (triangles) at λ = 633 nm. The dashed lines are guides for the eye and the solid lines represent the best fits to a theoretical function (see text).

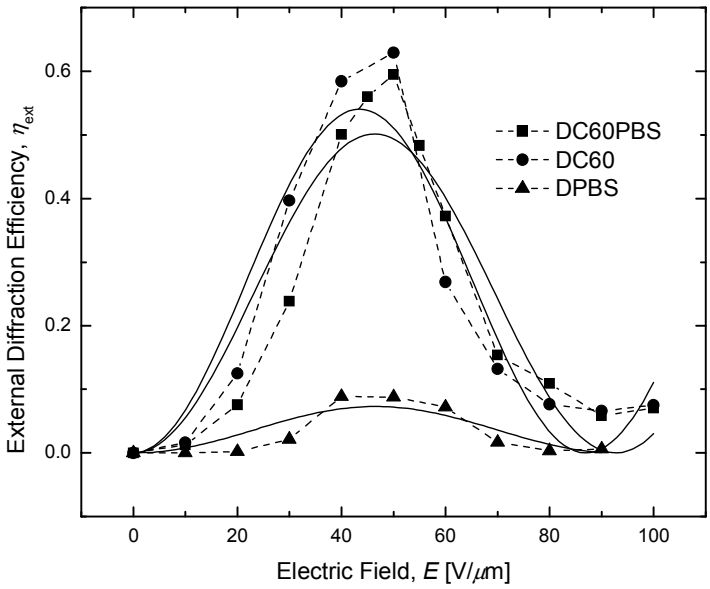

Figure 8. Electric field dependence of the external diffraction efficiencies, η_{ext}, for DC60PBS (squares), DC60 (circles), and DPBS (triangles) at $\lambda = 633$ nm. The dashed lines are guides for the eye and the solid lines represent the best fits to a theoretical function (see text).

Time resolved DFWM techniques were used in the quantification of the τ. An example of such DFWM data is presented in Fig. 9, where η is presented as a function of t for the DC60PBS with $E = 100$ V/μm. The solid line in the figure represents the best fit to Eq. 4 and a reasonably good fit to the data is obtained. In this case, $\tau_f = 0.399$ ms was derived from the fitting process. This figure-of-merit represents one of the best reported for any PR composite. This τ_f is nearly an order of magnitude faster than that obtained for the DC60 composite with $\tau_f = 2.42$ ms. It is noted that even this τ_f is among the best for

any PR composite under these conditions, which is demonstration of the practicality of the DMTPD-based composite.

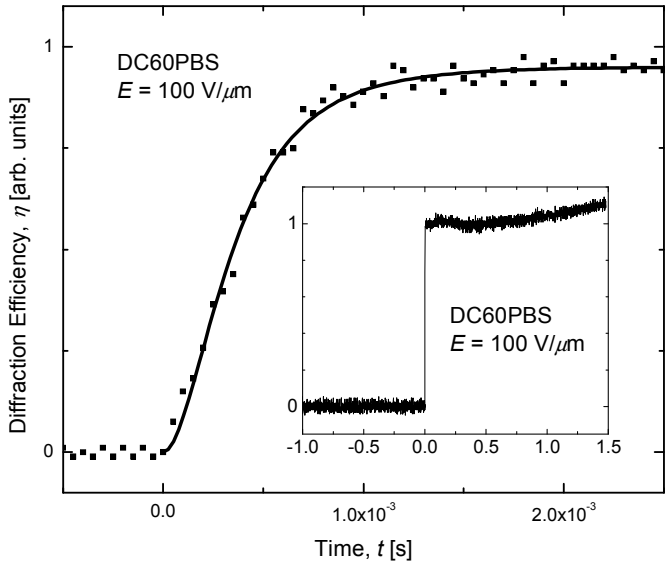

Figure 9. Temporal evolution of the diffracted probe beam, I_s, in the DFWM experiment for the DC60PBS device at E = 100 V/μm. The solid line is a fit to a weighted biexponential function (see text). The inset depicts an expanded view of the same data (the fit is eliminated for clarity).

Figure 10 depicts the τ_f as a function of E for the relevant devices. Obvious is that DC60PBS has a significantly faster τ_f than DC60, and both exhibit superior τ_f relative to DPBS, for the entire range of E investigated. It is speculated that DPBS has a relatively slow τ_f due to the exceedingly low concentration of photosensitizer present in this composite. As such, it takes longer to produce sufficient number of free charge-carriers to achieve a steady-state space-charge field. These data strongly suggest that the presence of

the QPbS has a significant effect on τ_f. These τ_f indicate the potential for the use of these composites in video-rate applications.

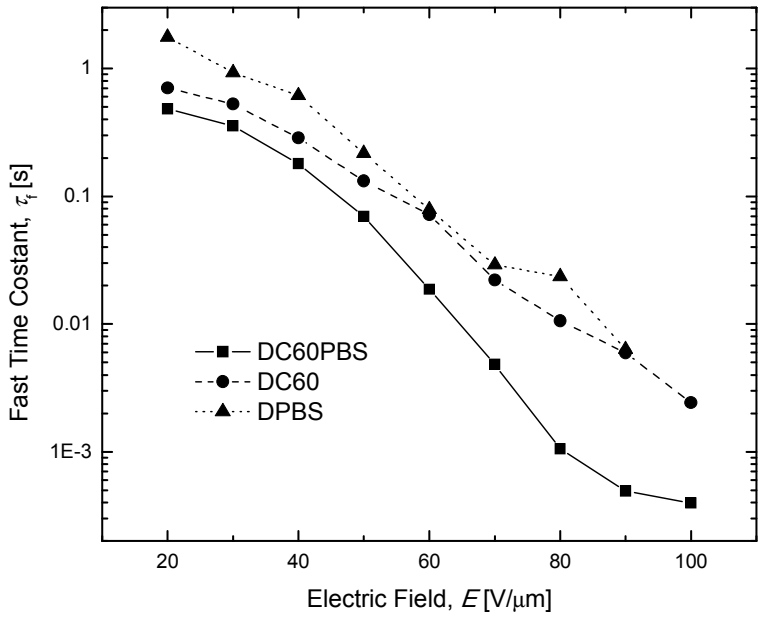

Figure 10. Electric field dependence of the fast time constant, τ_f, for DC60PBS (squares), DC60 (circles), and DPBS (triangles) at $\lambda = 633$ nm.
The lines are guides for the eye.

It has been speculated that it is the τ_f which is associated formation of the space-charge field and it is the τ_s which is attributed to the reorientation of the NLO chromophore, 7-DCST in this case. The τ_s are plotted as a function of E in Fig. 11. The τ_s exhibit a similar functional form as the τ_s however there appears to appear to be more noise in these data. Also evident is that there are no τ_s reported for DC60PBS for $E > 80$

V/μm or for DC60 when $E > 70$ V/μm. The reason for this is evident from the inset of Fig. 11. As mentioned in the Experimental section, the weighting factor, *m*, was also allowed to float in the fitting process.

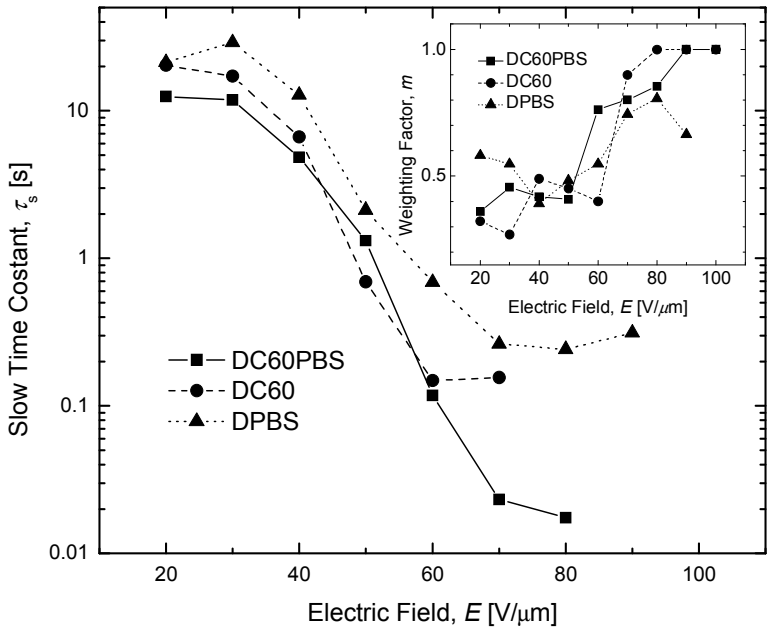

Figure 11. Electric field dependence of the slow time constant, τ_s, for DC60PBS (squares), DC60 (circles), and DPBS (triangles) at $\lambda = 633$ nm. The lines are guides for the eye. The inset depicts the electric field dependence of the weighting factor, *m*, for the same PR devices. The lines are guides for the eye.

Apparent from the figure is that the *m* are highly scattered, but display the unmistakable trend of more heavily weighting τ_f at the expense of τ_s as *E* is increased for all devices. At relatively low voltages m ≈ 0.5 and the τ_s and τ_f contribute almost equally to the grating formation. As higher voltages are attained, the data suggest that it is the formation of the space-charge field which becomes the limiting process. For relatively

high voltages the rise in DFWM signal can be modeled by a single exponential and *m* tends toward unity. For DPBS, *m* does increase with *E*, but $m \neq 1$ even at higher *E*. This is again attributed to the relatively slow build up in the density of free charge carriers, and the inability of the NLO chromophore to align quickly in the absence of a reasonably large space-charge field. Though given the scatter in the data, it is best to not draw a strict interpretation concerning this fact.

As outlined in the introduction, QPbS was included in the DC60PBS device with the expectation of enhancing the charge-carrier μ, thus improving the τ of this PR composite relative to a composite void of QPbS, i.e. DC60. The data leave little doubt as to the success of the approach, as τ_f showed an enhancement of nearly one order of magnitude and τ_s remained relatively constant. This distinction corresponds to current PR theory in that the presence of the QPbS was included to enhance charge-carrier μ, which would directly improve the speed at which the space-charge field is established, and it is this process which is commonly associated with the τ_f. Conversely, there is no reason to expect that the presence of QPbS would influence the rate at which the NLO chromophores, 7-DCST in this case, would reorient within the established space-charge field. Because it this process which is associated with τ_s, it is expected that τ_s should not be effected by the presence of QPbS and thus remain relatively constant between the DC60PBS and DC60 devices.

Although the inclusion of QPbS dramatically improved the τ_f, this observation does not in itself confirm that this enhancement was accomplished through the envisioned mechanism, an enhancement in charge-carrier μ, and this conclusion requires some

further analysis. Ideally, the μ should be measured directly through time-of-flight experiments. An attempt was made in this regard, however, as is typically the case the presence of the highly dipolar 7-DCST resulted in highly diffuse charge-packets precluding such measurements. In an effort to circumvent this issue, samples were fabricated void of 7-DCST however the DMTPD crystalized before such experiments could be completed. Although not possible with the current compositions, previous time-of-flight characterizations conducted with PVK doped with QCdS clearly demonstrated a correlation between the concentration of QCdS and the charge-carrier μ [19]. While it is very probable that the observed improvement in τ_f can be primarily attributed to an enhancement in μ, other mechanisms may be considered. Perhaps the most obvious mechanism is one involving the augmentation charge-carriers with QPbS acting primarily as a photosensitizer. Although QPbS does certainly act as a photosensitizer it is unlikely that such a significant improvement in τ_f could be attributed to this effect. Although the DPBS device exhibits respectable Φ, the loading content of QPbS, as exemplified by the exceedingly small increase in α_{633} in the DPBS device relative to that of the D0 device ($2.75\ cm^{-1} - 2.46\ cm^{-1} = 0.29\ cm^{-1}$), indicates that the QPbS is not likely responsible for any significant increase in the charge-carrier density. Furthermore, if QPbS were significantly contributing to the photo-charge generation process, an accompanying increase in η would be expected, but this was not observed. It was also speculated that QPbS may enhance PR performance in ways not related to its ability to act as a photosensitizer. Based on the propensity for Q-dots to act as traps in PR composites, it may be possible that the included QPbS may enhance the trapping of holes in the dark fringes. However, because the presence or absence of QPbS in the respective composites

had little if any effect on σ_d, and only a favorable effect on σ_p, it seems unlikely that QPbS is acting as a significant trapping species. Interestingly, the fact that the addition of QPbS results in an improvement in σ_p, without affecting σ_d, indicates that enhancements in charge-carrier μ may manifest exclusively in illuminated regions and not in dark regions. This performance would be favorable for PR performance because charge-carriers are ideally immobilized within the dark fringes. Lastly, because TBC is highly sensitive to trap density, the similarity in the TBC performances across the various composites further refutes the speculation that QPbS is acting as a significant source of traps.

4. CONCLUSION

The goal of this study was to examine the feasibility of using Q-dots to affect charge-carrier μ in a PR composite so as to improve the τ without detrimentally affecting PR efficiency of the composite. It has been demonstrated that through the inclusion of a narrow bang-gap Q-dot, specifically QPbS, sub-millisecond response times have been achieved for the first time in a PR composite under CW conditions. With a $\tau_f = 400$ μs, this approach makes the use of PR composites viable materials for video and other high-speed applications. It is noteworthy that the enhancement in τ_f is not accompanied by a loss in PR efficiency, with $\eta_{int} = 72\%$ and $\Gamma = 500$ cm^{-1} observed in the same composite, indicating that the included QPbS does not act as a significant of traps. An analysis of the experimental data strongly suggests that the enhancement in τ_f can be attributed to an improvement in enhanced charge μ, which may even be exclusively manifest in the

illuminated regions of the PR sample. It is anticipated that this approach can play a significant role in the eventual commercialization of this class of materials.

ACKNOWLEDGEMENT. The Authors wish to acknowledge the Materials Research Center at the Missouri University of Science and Technology and the Department of Chemistry at the Missouri University of Science and Technology.

REFERENCES

[1] *Photorefractive Materials and Their Applications, I & II, Topics in Applied Physics*, Vols. 61 and 62; Gunter, P., Huignard, J.-P., Eds.; Springer-Verlag: Berlin, 1988.

[2] Yeh, P. *Introduction to Photorefractive Nonlinear Optics*; Wiley: New York, 1993.

[3] Ostroverkhova, O.; Moerner, W. E. *Chem. Rev.* **2004**, *104*, 3267.

[4] Thomas, J.; Norwood, R. A.; Peyghambarian, N. *J. Mater. Chem.* **2009**, *19*, 7476.

[5] Salvador, M.; Prauzner, J.; Koeber, S.; Meerholz, K.; Turek, J. J.; Jeong, K.; Nolte, D. D. *Opt. Exp.* **2009**, *17*, 11834.

[6] Kukhtarev, N.; Dovgalenko, G.; Duree, G. C., Jr.; Salamo, G. J.; Sharp, E. J.; Wechsler, B. A.; Klein, M. B. *Phys. Rev. Lett.* **1993**, *71*, 4330.

[7] Winiarz, J. G.; Zhang, L.; Lal, M.; Friend, C. S.; Prasad, P. N. *Chem. Phys.* **1999**, *245*, 417.

[8] Winiarz, J. G.; Zhang, L.; Lal, M.; Friend, C. S.; Prasad, P. N. *J. Am. Chem. Soc.* **1999**, *121*, 5287.

[9] Winiarz, J. G.; Zhang, L.; Park, J.; Prasad, P. N. *J. Phys. Chem. B* **2002**, *106*, 967.

[10] Winiarz, J. G.; Prasad, P. N. *Opt. Lett.* **2002**, *27*, 1330.

[11] Binks, D. J.; Bant S. P.; West, D. P.; O'Brien, P.; Malik, M. A. *J. Mod. Opt.* **2003**, *50*, 299.

[12] Choudhury, K. R.; Winiarz, J. G.; Samoc, M.; Prasad, P. N. *Appl. Phys. Lett* **2003**, *82*, 406.

[13] Fuentes-Hernandez, C.; Suh, D. J.; Kippelen, B.; Marder, S. R. *Appl. Phys. Lett.* **2004**, *85*, 534.

[14] Aslam, F.; Binks, D. J.; Rahn, M. D.; West, D. P.; O'Brien, P.; Pickett, N.; Daniels, S. *J. Chem. Phys.* **2005**, *122*, 184713.

[15] Aslam, F.; Binks, D. J.; Daniels, S.; Pickett, N.; O'Brien, P. *Chem. Phys.* **2005**, *316*, 171.

[16] Choudhury, K. R.; Sahoo, Y.; Ohulchanskyy, T. Y.; Prasad, P. N. *Appl. Phys. Lett.* **2005**, *87*, 073110.

[17] Choudhury, K. R.; Sahoo, Y.; Jang, S.; Prasad, P. N. *Adv. Func. Mat.* **2005**, *15*, 1751.

[18] Cho, N.; Choudhury, K. R.; Thapa, R. B.; Sahoo, Y.; Ohulchanskyy, T.; Cartwright, A. N.; Lee, K.-S.; Prasad, P. N. *Adv. Mater.* **2007**, *19*, 232.

[19] Winiarz, J. G. *J. Phys. Chem. C* **2007**, *111*, 1904.

[20] Fears, T.; Anderson, C.; Winiarz, J. G. *J. Chem. Phys.* **2008**, *129*, 1.

[21] Moon, J.-S.; Mahala, B. D.; Winiarz, J. G. *J. Phys. Chem. C.* Submitted.

[22] Smith, A. M.; Nie, S. *Acc. Chem. Res.* **2010**, *43*, 190.

[23] Wright, D.; Díaz-García, M. A.; Casperson, J. D.; DeClue, M.; Moerner, W. E. *Appl. Phys. Lett.* **1998**, *73*, 1490.

[24] Díaz-García, M. A.; Wright, D.; Casperson, J. D.; Smith, B.; Glazer, E.; Moerner, W. E.; Sukhomlinova, L. I.; Twieg, R. J. *Chem. Mater.* **1999**, *11*, 1784.

[25] Ostrauskaite, J.; Karickal, H. R.; Leopold, A.; Haarer, D.; Thelakkat, M. *J. Mater. Chem.* **2002**, *12*, 58.

[26] Wright, D.; Gubler, U.; Moerner, W. E.; DeClue, M. S.; Siegel, J. S. *J. Phys. Chem. B* **2003**, *107*, 4732.

[27] Thomas, J.; Fuentes-Hernandez, C.; Yamamoto, M.; Cammack, K.; Matsumoto, K.; Walker, G. A.; Barlow, S.; Kippelen, B.; Meredith, G.; Marder, S. R.; Peyghambarian, N. *Adv. Mater.* **2004**, *16*, 2032.

[28] Jung, G. B.; Yoshida, M.; Mutai, T.; Fujimura, R.; Ashihara, S.; Shimura, T.; Araki, K.; Kuroda, K. *Sen'i Gakkaishi* **2004**, *60*, 193.

[29] Fuentes-Hernandez, C.; Thomas, J.; Termine, R.; Meredith, G.; Peyghambarian, N.; Kippelen, B. *Appl. Phys. Lett.* **2004**, *85*, 1877.

[30] Tay, S.; Thomas, J.; Eralp, M.; Li, G.; Norwood, R. A.; Schülzgen, A.; Yamamoto, M.; Barlow, S.; Walker, G. A.; Marder, S. R.; Peyghambarian, N. *Appl. Phys. Lett.* **2005**, *87*, 171105.

[31] Eralp, M.; Thomas, J.; Li, G.; Tay, S.; Schülzgen, A.; Norwood, R. A.; Peyghambarian, N.; Yamamoto, M. *Opt. Lett.* **2006**, *31*, 1408.

[32] Eralp, M.; Thomas, J.; Tay, S.; Li, G.; Schülzgen, A.; Norwood, R. A.; Yamamoto, M.; Peyghambarian, N. *Appl. Phys. Lett.* **2006**, *89*, 114105.

[33] Grunnet-Jepsen, A.; Wright, D.; Smith, B.; Bratcher, M. S.; DeClue, M. S.; Siegel, J. S.; Moerner, W. E. *Chem. Phys. Lett.* **1998**, *291*, 553.

[34] Barkhouse, D. A. R.; Pattantyus-Abraham, A. G.; Levina, L.; Sargent, E. H. *ACS Nano* **2008**, *2*, 2356.

[35] Streetman, B. G.; Sanjay, B. *Solid State electronic Devices* (*5th ed.*); Prentice Hall: New Jersey, **2000**.

III. FORMATION OF WATER SOLUBLE WAVELENGTH TUNABLE InGaP AND InP QUANTUM DOTS

ABSTRACT

Quantum dots (Qdots) have recently been of interest for biological applications as effectual bio-makers. Operational wavelength and water solubility are some of the core considerations applicable to Qdots in biology. High quality, wavelength tunable, and water soluble InGaP and InP have been prepared via a simple thermal synthesis method. Experimental evidence illustrates that the decrease in quantum yield previously observed in lipidized quantum dots loss is greatly diminished through this approach, resulting in excellent controle of emission wavelength and enhanced PL intensity. The size of Qdots was controlled via a two-step etching process. The two-step etching process provided ease of size control with improved PL intensity. Through this approach, the loss in PL intensity associated with the lipidation process is minimized.

INTRODUCTION

Nanoparticles have very different optical, electrical and surface properties, relative to their bulk counterparts. These unique properties make nanoparticles potential useful in a variety of applications such as core materials in the field of solar cells [1, 2], light-emitting diodes (LED) [3], Lasers [4, 5] and others. There has also been a variety of research concerning the use of nanoparticles as biological labeling agents [6-10]. Qdots are a type of nanoparticle which shows size-dependent properties [11]. Since the first high grade quantum dots were synthesized by the Bawendi et al. in 1993, group II-IV semiconductor Q-dots have been the focus of many studies primarily due to their the high

photoluminescence (PL) efficiencies. Core-shell Q-dots utilizing CdSe as the core and the wider band-gap material ZnS as the shell have exhibited PL quantum efficiencies in excess of 85% [12-14]. In II-IV group semiconductor quantum dots, CdTe quntum dots could have more than 65% of PL efficiency by the optimal synthetic condition [15]. In spite of the high quality in PL efficiency, group II-IV Q-dots are composed of highly toxic materials such as Cd, Se, or Te, which hinders biological applications and are associated with serious environmental problems.

For this reason research has more recently focused on group III-V Q-dots, such as indium phosphide (InP) and indium gallium phosphide (InGaP). InP Q-dots are non-toxic and have reasonably good quantum yield, though typically lower than that associated with CdSe Q-dots [16]. It is possible to tune the PL emission from InP Q-dots from visible to near infrared wavelengths, with a range slightly larger than that associated with CdSe [17]. There have been several attempts to synthesize InP core-shell Q-dots, however, the PL quantum efficiencies were relatively low. Specifically, InP cores with $ZnCdSe_2$ shells showed a PL quantum efficiency of 5-10%, [18] and InP cores with ZnS shells, involving a 3 week reaction time, exhibited over 23% [19]. Recently Strouse et al. reported a novel method by which to synthesize Q-dots such as CdSe, InGaP and InP using a microwave reactor with a coordinating solvent, decane in this case. They reported a nearly monodisperse size distribution [17]. This approach is a modification of the dehalosilylation reaction between indium chloride and tris-(trimethylsilyl)phosphine in tri-n-octylphosphine oxide/tri-n-octylphosphine (TOPO/TOP) [20-22]. However, PL efficiency of the InP Q-dots was quite low as 15%. Micic et al. as well as the Weller group have described an enhancement in PL efficiency through the removal of dangling

bonds at the Q-dot surface by etching in HF and irradiation in ultra violet light. [23-25] Using this approach InP Q-dots with quantum yields of 30-40% were reported [26]. Herein, a synthesis of InP and InGaP Q-dots is described which employs tunability in operating wavelength and water solubility as well as better quantum efficiency. As we mentioned before, another shell of the semiconductor which has wider band gap than core materials can increase PL efficiency such as CdSe core with ZnS shell [27], and InAs core with CdSe or ZnSe shell.[18], have suggested .

InP Q-dots are non-toxic, exhibit moderate PL quantum yield, and can be made water soluble for biological applications. The InGaP and InP Q-dots were lipidized with PEG lipid micelles based on a technique in literature and are highly soluble in water [28].

EXPERIMENTAL SECTION

All chemicals were purchased from Sigma-Aldrich Chemical and used without further purification except where otherwise noted. The lipidization materials, 1, 2-distearoyl-sn-glycero-3-phosphoethanolamine-N-[carboxy(polyethylene glycol)-2000] (DSPE-PEG 2000) and 1,2-palmitoyl-sn-glycero-3-phosphoethanolamine-N-[methoxy(polyethylene glycol)-2000] (PEG-2-PE) were purchased from Avanti Polar Lipids. The minimum amount of toluene was used to disperse Q-dots. A 2:1 anhydrous butanol and methanol mixture was used to induce particle precipitation, and precipitated Q-dots collected in the pellet state after centrifugation for 15 min. The collected particles were redispersed in toluene and the precipitation process was repeated. After this process the product was dispersed in methanol.

Synthesis of InGaP and InP. The preparation of InGaP was based on a modified method from literature [17, 29, 30]. The In and Ga intermediates was prepared by mixing 428.2 μmol of Indium(III) acetate, 42.8 μmol of gallium(III) 2,4-pentanedionate and 1.413 mmol of plamitic acid in 30mL of octadecane in a three neck flask. The solution was backfilled with nitrogen four over 2 hours at 110° C and then cooled to 50° C. At this time 237 μmol of tris(trimethylsilyl)phosphine (TMSP) was injected into the flask with stirring and the color turned from colorless to pale yellow. After 30 min the solution was rapidly heated to 280 °C and the color turned from pale yellow to deep orange. After ~ 7 min the flask was quickly cooled with compressed air. The product was precipitated by the addition of the butanol/methanol mixture and redispersed in toluene. The precipitation process was repeated three times. The preparation of InP Q-dots was identical to that of InGaP Q-dots with the exception of the gallium precursor. The isolated Q-dots were characterized by UV-vis, and PL spectroscopy.

Etching of InGaP and InP. The concentration and size of InGaP and InP was estimated from the absorption spectrum using the molar coefficient of InP [26]. An aliquot of InGaP or InP nanocrystals which contain 1×10^{-7} mol of particles in toluene was dispersed in about 5 mL of n-butanol. Particles which have a size larger than 5nm are insoluble in n-butanol. A small amount (2-5mL) of isooctane was added to dissolve large particle until the solution became optically clear, and then 0.25 g of trioctylphosphine oxide (TOPO) was added. The prepared etching solution was moved into a 50 mL polyperfluoroethylene vessel to avoid corrosion by the strong acid, and 250 μL of HF solution was added under stirring. The HF etching solution contained 0.527 mL of aqueous HF (40 wt%), 0.065 mL of H_2O, and 5.0 mL of n-butanol. For the second,

photochemical etching process, Q-dots which dispersed in etching solution were exposed to 120W halogen lamp passed through a long-pass filter with a cutoff wavelength which depended on particle size as determined by UV-vis spectroscopy. Q-dots were etched for 4 hr. The etched Q-dots were isolated from the reaction mixture by adding 15 mL of acetonitrile, and centrifuged at 5,000 rpm for 10 min and redispersed in toluene.

Before the second etching, InGaP or InP Q-dots were cleaned with methanol once. The 1 mL HF etching solution which is 2.5 times more concentrated than first etching solution was dropped into InGaP or InP nanoparticle solution slowly. Typically, Each nan oparticles are dispersed in n-butanol and isooctane as the same as the first etching. The se cond etching process was complete in ~ 3 hours, and Q-dots were cleaned by successive precipitations and finally re-dispersed in toluene. The collected product was stable in air a nd retained their PL efficiency for several months.

Carboxylation. In a typical preparation, 1×10^{-7} mol of InP or InGaP, as calculated based on UV spectroscopy and dispersed in chloroform was mixed with 5.5×10^{-6} mol of phospholipids (80% PEG-2-PE and 20% DSPE-PEG(2000)) Carboxylic Acid. The chloroform was evaporated by bubbling nitrogen gas through the solution and the dried product was kept under vacuum for several hours to remove residual solvent. The dried film was heated to 80° C in a water bath for 1 min and 2 ml of water were added. The sample was heated to 80° C for 15 min with a vigorous mixing, and then the sample was cooled in water and sonicated for 20 min. This heating and cooling/sonication process was repeated at least 4 times to obtain an optically clear solution. Subsequently aggregates and large particles were removed by a centrifuge (13,000 rpm for 5 min).

RESULTS AND DISCUSSION

InGaP and InP nanoparticles were made by a modified thermal synthesis. The products were orange in color and can be easily dispersed in toluene or chloroform.

Figure 1 and 2 shows the absorption spectrums of InGaP and InP Qdots. After the HF etching process a blue-shift was observed in the absorption spectrum of InGaP. Prior to etching, the InGaP Q-dots exhibited a peak at ~500 nm. Therefore, long wave pass filter with a cut-off wavelength of 500nm was employed in the first etching. The decrease in absorption was observed after the etching process caused by a decrease in Q-dot concentration. The average sizes of InP Qdots are 4.5 nm by the first etching and 3.1 nm by second etching based on TEM image which is shown in figure 3.

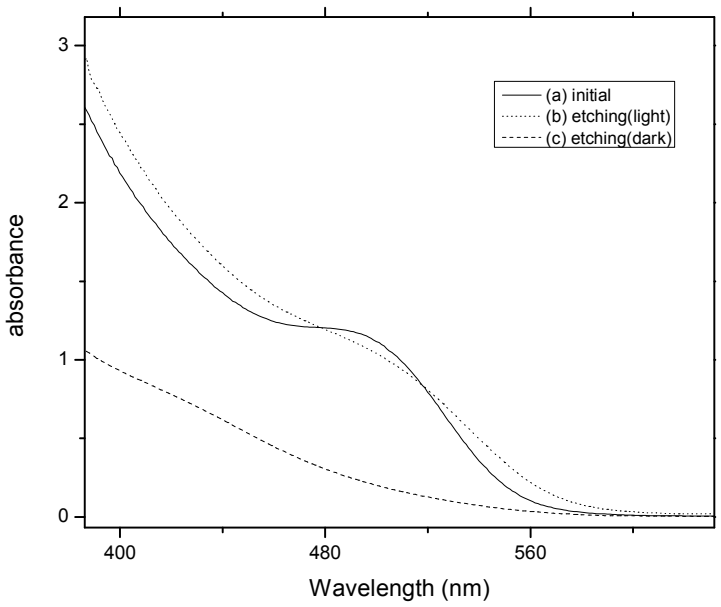

Figure 1. UV-vis spectrum of InGaP (a) initial, (b) after first etching, and (c) after second etching.

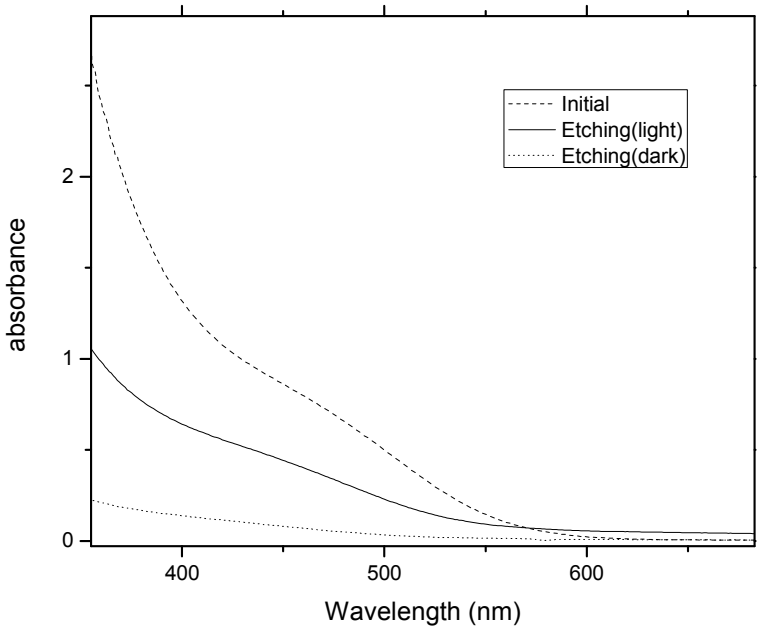

Figure 2. UV-vis spectrum of InP (a) initial, (b) after first etching, and (c) after second etching.

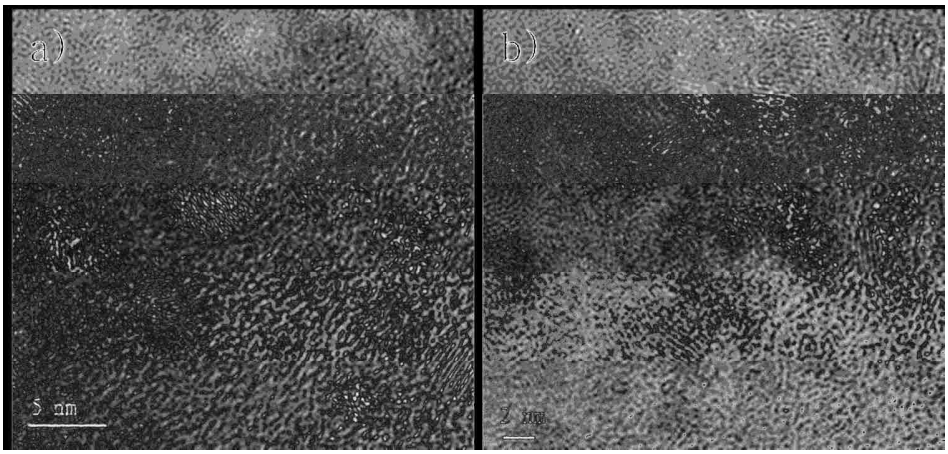

Figure 3. TEM images of InP Qdots, a) after first etching, b) after second etching.

Resulting from first etching, as shown in figure 4, PL intensity increased more 4 times than the initial state. It is shown in figure 4 (a) and (b). Both PL peak was shown at 588 nm in the initial and after first etching under the light. We expected a small blue-shift the following literature; however, it did not been changed. Micic et al. reported that the increased PL resulted from removal of surface phosphorus vacancies which acted as an electron trap [23]. In many cases, especially for biological application, emission wavelength needs to be specified. In this communication, we tried to make InGaP and InP nanoparticles detectable at the specific filter in confocal LASER microscope. Weller et al. reported wavelength specified InP which was etched by HF, and sorted by size selective precipitation [19]. However, by their methods, final nanoparticles which have specific wavelength of PL were only a part of products. Therefore, we tried the second etching with the additional HF and made protocol more appropriate for the desired PL wavelength. Figure 4 (c) shows the PL spectrum result after second etching. We also have tried second etching with illumination of light; however, etching rate or size decrease rate per time was strongly fast as decreasing size of nanoparticles. For a control of etching rate, we did not use light for second etching. When comparing second etching with the first etching, in case of InGaP, PL peak blue-shifted from 585 nm to 550 nm which accomplished in 3 hours. It is shown in figure 4 (b) and (c). However, PL efficiency decreased about 40% which needs to be improved further study.

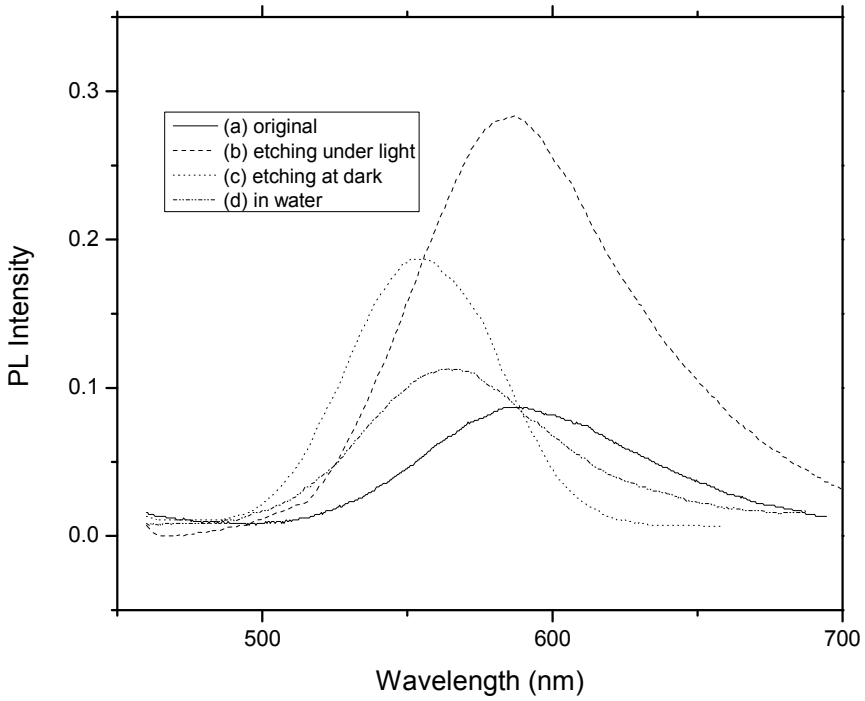

Figure 4. InGaP PL spectrum (a) initial, (b) after first etching, (c) after second etching, and (d) after lipidization.

In figure 5, the PL wavelength of initial state of InP was changed from 584 nm to 576 nm after the first etching with illumination of light. PL efficiency of InP nanoparticle after first etching was increased about 3 times when compared with initial state. PL efficiency was enhanced by the same reason with in case of InGaP. The decreasing of PL wavelength resulted from decreasing of particle size. The concentration of HF etching solution was a little bit higher for InP nanoparticles, however, was appropriate for InGaP nanoparticle and need to be studied for future experiments.

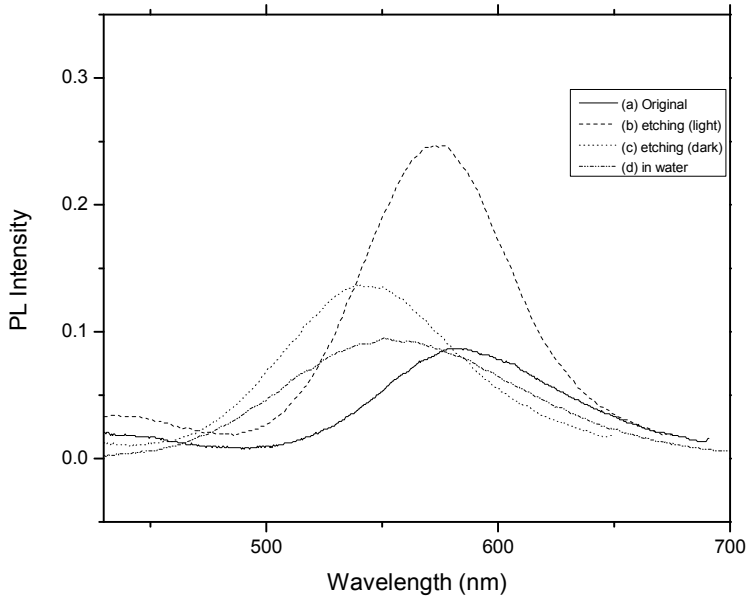

Figure 5. InP PL spectrum (a) initial, (b) after first etching, (c) after second etching, and (d) after liphidization.

In the literature, PL efficiency was rapidly increased and reached the steady state during the first etching process over 20 hours [19]. In our experiment, we have got slightly different result. In Figure 6, during 14 hours etching with low concentration etching solution and light, PL efficiency rapidly increased until 3 hours, and then decreased in next 12 hours. Figure 7 shows emission wavelength decreased gradually during the initial 3 hours and then the rest rapidly dropped. It was slightly different batch to batch because we did not use size selective precipitation but showed same trend batch to batch. Our nanoparticle solution was mixture of particles those sizes were vary. We think different size distribution of each batch made different etching efficiency.

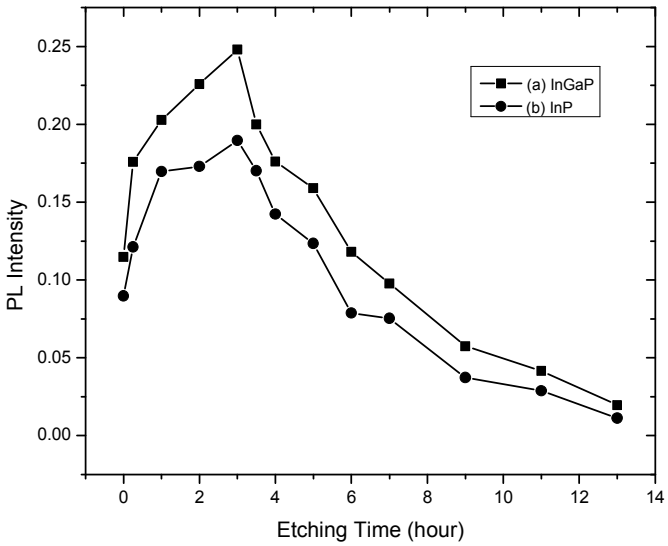

Figure 6. Changing in PL intensity by first etching (a) InGaP, and (b) InP. The lines are guides for the eye.

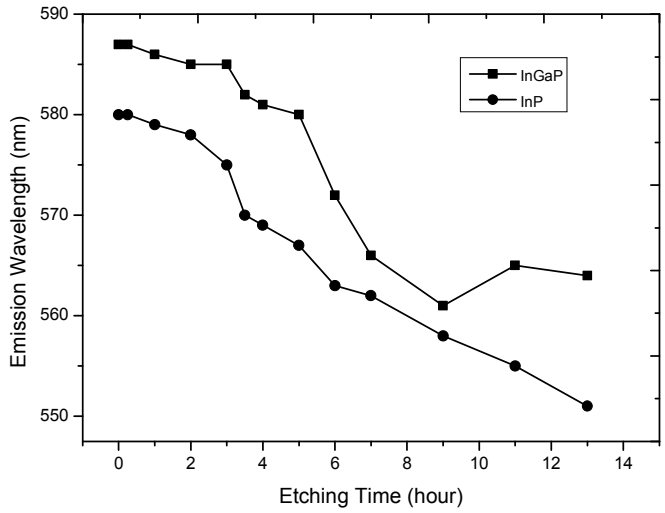

Figure 7. Changing in emission wavelength by first etching (a) InGaP, and (b) InP. The lines are guides for the eye.

Indeed, PL efficiency was bright enough to use them for biological application of our collaborated group. However, PL peak wavelength was too long to apply them in our conforcal laser microscope. Rather than spend thousands of dollars, we decided to reduce their size. There were two choices. One was size selective precipitation of nanoparticles. The other was further etching to reduce particle size. In our purpose, we needed a large amount of nanoparticles if there were some loss of quality such as size distribution, PL efficiency and so on. 2.5 times more concentrated HF etching solution was used for second etching process. Figure 8 show PL intensity decreases by function of etching time. Figure 9 shows the PL emission wavelength was moved from about 580 nm to 540 nm in 2 hours in both InGaP and InP. PL intensity dropped in this period of time. After 3 hours we could not detect PL because majority of particles get too small to detect in our PL spectrum.

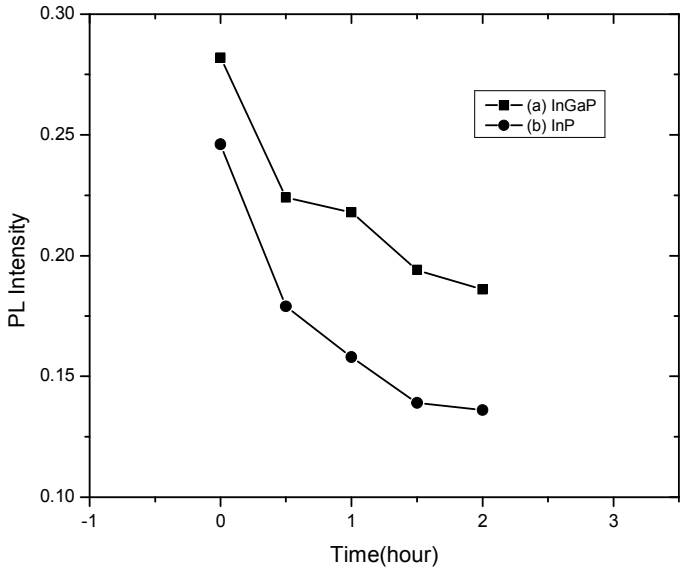

Figure 8. Changing in PL intensity by second etching (a) InGaP and (b) InP. The lines are guides for the eye.

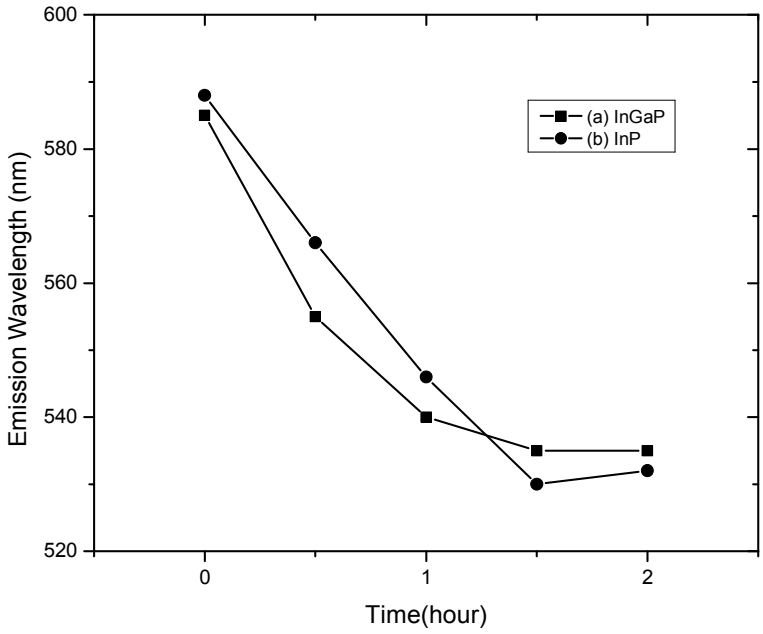

Figure 9. Changing in emission wavelength by second etching (a) InGaP and (b) InP. The lines are guides for the eye.

When it is combined with both the first and the second etching, from the initial state of Qdots, PL intensity was slightly increased and/or even. Figure 10 shows combination of 3 hours in the first etching and the second etching. We could manipulate operating wavelength by decreasing Qdot size without PL intensity through the double etching process. Figure 11 shows operating wavelength maintained almost in the same level with the first etching, and then decreased sharply in the second etching. Maintaining PL efficiency with manipulating wavelength at same time seems impossible without the double etching process.

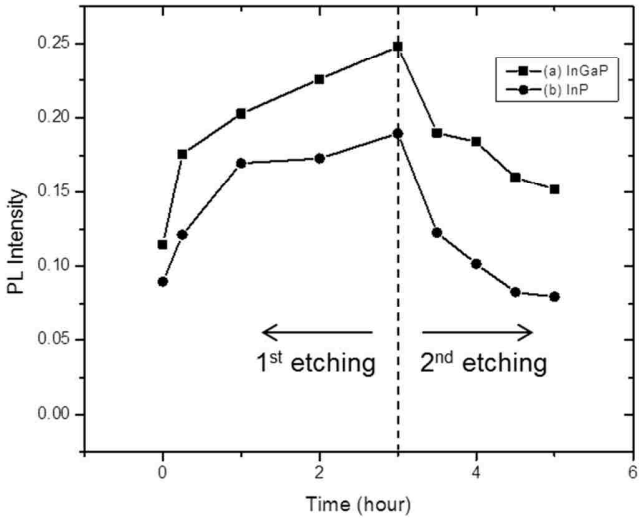

Figure 10. Changing in PL intensity by etching (a) InGaP and (b) InP.
The lines are guides for the eye.

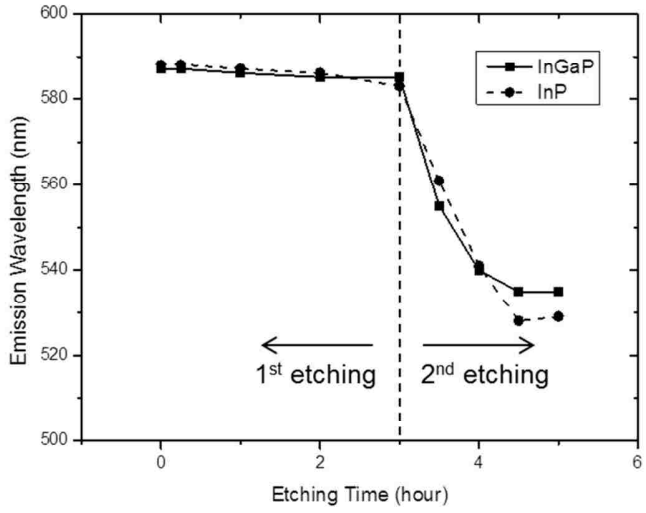

Figure 11. Changing in emission wavelength by etching (a) InGaP and (b) InP.
The lines are guides for the eye.

Collected and cleaned particles with toluene and methanol have bright yellow color. The color of nanoparticles changed from deep orange to bright yellow by processing. By using PEG based phosphor lipid we successfully dispersed etched nanoparticles in water. Nanoparticles lost less than 40% of PL efficiency and it was less than other results in literature [26].

CONCLUSION

The emission wavelength tunable water soluble InGaP and InP Q-dots using thermal synthesis method was investigated. Experimental evidence strongly suggests that previously observed quantum yield loss of lipidized quantum dot is greatly diminished through this approach, resulting in excellent controlling of emission wavelength in short time and enhanced PL intensity. It is important to note that the size of Q-dots utilized in this study was controlled by two step etching process. When it compare with single step etching, results of double step etching shows effective tuning in emission wavelength and improvement of PL intensity. The loss of PL intensity when Q-dots were lipidized was also decreased. The future study should focus on the consequence of optimizing the parameter.

ACKNOWLEDGEMENTS

The Authors wish to acknowledge the Materials Research Center at the Missouri University of Science and Technology and the Department of Chemistry at the Missouri University of Science and Technology.

REFERENCES

[1] Robert J. Cava, Francis J. DiSalvo, Louis E. Brus, Kim R. Dunbar, Christopher B. Gorman, Sossina M. Haile, Leonard V. Interrante, Janice L. Musfeldt, Alexandra Navrotsky, Ralph G. Nuzzo, Warren E. Pickett, Angus P. Wilkinson, Channing Ahn, James W. Allen, Peter C. Burns, Gerdrand Ceder, Christopher E. D. Chidsey, William Clegg, Eugenio Coronado, Hongjie Dai, *et al., Prog. Solid State Chem.*, **2002**, 30, 1.

[2] Nozik, A. *J. Physic. E* **2002**, 14, 115.

[3] Colvin, V. L.; Schlamp, M. C.; Alivisatos, A. P. *Nature* **1994**, 370, 354.

[4] Kilmov, V. I.; Mikhailovsky, A. A.; Xu, S.; Malko, A.; Hollingsworth, J. A.; Leatherdale, C. A.; Eisler, H. J.; Dawendi, M. G. *Science* **2000**, 290, 314.

[5] Artemyev, M. V.; Woggon, U.; Wannemacher, R.; jaschinski, H.; Langbein, W. *nano Lett.* **2001**, 1, 309.

[6] Bruchez, M.; Moronne, M.; Gin, P.; Weiss, S.; Alivisatos, A. P. *Science* **1998**, 281, 2013.

[7] Chan, W. C. W.; Nie, S. M. *Science 1998*, 281, 2016.

[8] Han, M. Y.; Gao, X.; Su, J. Z.; Nie, S. M. *Nat. Biotechnol*. **2001**, 19, 631.

[9] Kim, S.; Lim, Y. T.; Soltesz, E. G.; De Grand, A. M.; Lee, J.; Nakayama, A.; Parker, J. A.; Mihaljevic, T.; Laurence, R. G.; Dor, D. M.; Cohn, L. H.; Bawendi, M. G.; Frangioni, J. V. *Nat. Biotechnol*. **2004**, 22, 93.

[10] Michalet, X.; Pinaud, F. F.; Bentolila, L. A.; Tsay, J. M.; Doose, S.; Li, J. J.; Sundaresan, G.; Wu, A. M.; Gambhir, S. S.; Weiss, S. *Science* **2005**, 307, 538.

[11] Yu, W. W.; Qu, L.; Guo, W.; Peng, X.; *Chem. Matter.* **2003**, 15, 2854.

[12] Dabbousi, B. O.; Rodriguez-Viejo, J.; Mikulec, F. V.; Heine, J. R.; Mattoussi, H.; Ober, R.; Jensen, K. F.; Bawendi, M. G. *J. Phys. Chem. B* **1997**, 101, 9463.

[13] Talapin, D. V.; Rogach, A. L.; Kornowski, A.; Haase, M.; Weller, H. *Nano Lett.* **2001**, 1, 207.

[14] Talapin, D. V.; Rogach, A. L.; Mekis, I.; Haubold, S.; Kornowski, A.; Haase, M.; Weller, H. *Colloid Surf. A* **2002**, 202, 145.

[15] Li, C. L.; Murase, N. *Chem. Lett*. **2005**, 34, 92.

[16] Li, C. L.; Ando, M.; Enomoto, H.; Murase, N. *J. Phys. Chem. C* **2008**, 112, 20190.

[17] Gerbec, J. A.; Magana, D.; Washington, A.; Strouse, G. F.; *J. Am. Chem. Soc.* **2005**, 127, 15791.

[18] Cao, Y. W.; Banin, U. *J. Am. Chem. Soc.* **2000**, 122, 9692.

[19] Micic, O. I.; Smith, B. B.; Nozik, A. J. *J. Phys. Chem. B* **2000**, 104, 12149.

[20] Guzelian, A. A.; Katari, J. E. B.; Kadavanich, A. V.; Banin, U.; Hamad, K.; Juban, E.; Alivisatos, A. P.; Wolters, R. H.; Arnold, C. C.; Heath, J. R. *J. Phys. Chem.* **1996**, 100, 7212.

[21] Micic, O. I.; Nozik, A. J. *Handbook of Nanostructured Materials and Nanotechnology*, Nalwa, H. S., Ed.; Academic Press: San Diego, **2000**; v. 1, 427.

[22] Micic, O. I.; Curtis, C. J.; Jones, K. M.; Sprague, J. R.; Nozik, A. J. *J. Phys. Chem.* **1994**, 98, 4966.

[23] Micic, O. I.; Sprague, J. R.; Curtis, C. J.; Jones, K. M.; Machol, J. L.; Nozik, A. J.; Giessen, H.; Fluegel, B.; Mohs, G.; Peyghambarian, N. *J. Phys. Chem.* **1995**, 99, 7754.

[24] Micic, O. I.; Cheong. H. Fu; Zunger, A.; Sprague, J. R.; Mascaren-has, A.; Nozik, A. J. *J. Phys. Chem. B* **1997**, 101, 4904.

[25] Micic, O. I.; Jones, K. M.; Cahill, A.; Nozik, A. J. *J. Phys. Chem. B* **1998**, 102, 9791.

[26] Talapin, D. V.; Gaponic, N.; Borchert, H.; Rogach, A. L.; Haase, M.; Weller, H *J. Phys. Chem. B* **2002**, 106, 12659.

[27] Hines, M. A.; Guyot-Sionnest, P. *J. Phys. Chem.* **1996**, 100, 468.

[28] Depalo, N.; Mallardi, A.; Comparelli, R.; Striccoli, M.; Agostriano, A.; Curri, M. L. *J. Col. Int. Sci.* **2008**, 325, 558.

[29] Battaglia, D.; Peng, X. G. *Nano Lett*. **2002**, 2, 1027.

[30] Strouse, G. F.; Gerbec, J. A.; Magana, D. Method for Synthesis of Colloidal Nanoparticles, Patent Pending 2005, S/N 10/945, 053.

IV. SYNTHESIS, CHARACTERIZATION AND APPLICATIONS OF CARBOXYLATED AND POLYETHYLENE-GLYCOLATED BIFUNCTIONALIZED InP/ZnS QUANTUM DOTS IN CELLULAR INTERNALIZATION MEDIATED BY CELL-PENETRATING PEPTIDES

ABSTRACT

Semiconductor nanoparticles, also known as quantum dots (QDs), are widely used in biomedical imaging studies and pharmaceutical research. Cell-penetrating peptides (CPPs) are a group of small peptides that are able to traverse cell membrane and deliver a variety of cargoes into living cells. CPPs deliver QDs into cells with minimal nonspecific absorption and toxic effect. In this study, water-soluble, monodisperse, carboxyl-functionalized indium phosphide (InP)/zinc sulfide (ZnS) QDs coated with polyethylene glycol lipids (designated QInP) were synthesized for the first time. The physicochemical properties (optical absorption, fluorescence and charging state) and cellular internalization of QInP and CPP/QInP complexes were characterized. CPPs noncovalently interact with QInP in vitro to form stable CPP/QInP complexes, which can then efficiently deliver QInP into human A549 cells. The introduction of 500 nM of CPP/QInP complexes and QInP at concentrations of less than 1 M did not reduce cell viability. These results indicate that carboxylated and polyethylene-glycolylated (PEGylated) bifunctionalized QInP are biocompatible nanoparticles with potential for use in biomedical imaging studies and drug delivery applications.

INTRODUCTION

A quantum dot (QD) is composed of a few hundred to several thousand atoms, and the size of a QD typically ranges from 1 to 20 nm [1,2]. Since the first demonstration

of the use of QDs as a fluorescent label in biological systems, many surface modifications and functionalization for various applications have been described [3–5]. Due to their high photo luminescent quantum efficiency, photostability, tunability, narrow emission spectral band and pro-longed fluorescence lifetime, QDs have the potential to improve sensitivity and specificity of fluoroassays relative to more traditional fluorescent proteins and organic fluorophores [2, 6, 7]. Many approaches have been taken to utilize QDs for biomedical imaging, including cellular labeling, intracellular sensors, deep-tissue and tumor targeting and imaging agents, and sensitizers for photothermal therapy [8]. In addition, QDs exhibit a high capacity for drug loading due to their large surface area relative to their submicron counterparts.

In general, QDs can be synthesized in aqueous solutions, nonpolar solvents or on a solid substrate [9]. A common practice is to passivate qds with an inorganic layer of another semiconducting species with a wider band-gap, forming a core–shell structure, such as cadmium selenide (cdse) qd cores coated with a zinc sulfide (ZnS) shell. This passivating shell provides several advantages including: (1) enhancement of QD luminescence by improving quantum yield and narrowing the emission spectrum and (2) reduction of cytotoxicity by preventing the leaching of core materials [9,10]. The toxicity of lead sulfide (PbS) QDs can be significantly reduced by encapsulating the QD surface with polyethylene glycol (PEG) grafted (PEGylated) phospholipid micelles [11]. While QDs have been extensively studied for use in fields such as nanomedicine, the toxicity issues associated with QDs are of concern due to the unknown risks associated with biological exposure to QDs [11]. In addition, the core–shell structure can be functionalized using covalent conjugation schemes to link desired

probes to the surface of the QD. The organic capping layer on the QD surface may possess reactive groups that interact with target molecules in a covalent or noncovalent manner. Cell-penetrating peptides (CPPs), or protein transduction domains, comprised of basic amino acid-rich sequences are able to traverse the cell membrane and deliver molecular cargoes of varied nature into living cells [12–15]. CPPs were first recognized in the human immunodeficiency virus type 1 (HIV-1) transactivation of transcription (Tat) protein that is capable of crossing plasma membranes of viral-infected and uninfected cells [16,17]. CPPs include amphipathic, hydrophobic and cationic peptides [18, 19]. Research into the ability of CPPs to deliver biologically active molecules into cells has dramatically increased in recent years. CPPs are one of the most promising tools in the development of therapeutics, as evident in at least twenty medical trials [14,20]. CPP-compatible cargo molecules include proteins, nucleic acids, peptide nucleic acids, cytotoxic therapeutic drugs, inorganic particles and liposomes [13, 14, 21]. CPPs can deliver cargoes with sizes up to 200 nm in diameter [22]. CPPs are nontoxic to most cells and small organisms [23–27]. CPPs are also usually nontoxic in vitro and nonimmunogenic in vivo [28].

QDs do not readily enter cells, and aggregation often occurs before and after internalization [7, 29]. To overcome these limitations, functionalization of the QDs surface has been performed with CPPs by either covalent [30–32] or noncovalent [33–36] linkages. CPP-facilitated delivery of QDs has the potential to reduce nonspecific absorption and adverse effects in cells and organisms [8]. We previously demonstrated that arginine-rich CPPs, such as nonaarginine (R9) and histidine-rich nona-arginine (HR9), interact with carboxylated QDs to form stably noncovalent CPP/QD complexes

in vitro [33–36]. These CPP/QD complexes enter live cells efficiently. Furthermore, mechanistic studies revealed that the cellular uptake mechanisms of R9/QD or HR9/QD complexes involve multiple internalization pathways [33] or direct membrane translocation [36], respectively.

In this study, we (1) synthesized water-soluble, biocompatible, carboxyl- and PEG-bifunctionalized indium phosphide (InP)/ZnS QDs (QInP), (2) characterized the physicochemical properties of QInP and (3) evaluated CPP-mediated uptake of QInP into cells. The absorption and photoluminescence spectra of QInP were characterized using a spectrophotometer. The morphology and charging state of QInP and CPP/QInP complexes were characterized using an agarose-based gel retardation assay and zeta-potential analyzer. Four CPPs were used: SR9, HR9, PR9 and IR9. The intracellular delivery of CPP/QInP complexes was examined using flow cytometry, zeta-potential analysis and live cell imaging. Finally, the cytotoxicity of QInP and CPP/QInP complexes was assessed using the sulforhodamine B (SRB) assay.

MATERIALS AND METHODS

Synthesis of InP/ZnS QDs functionalized with DSPE-PEG (2000) carboxylic acid The preparation of QInP was based on modifications of published methods [37–40]. Indium (iii) acetate and hexadecanoic acid were mixed in octadecane. Subsequently, the temperature was raised to 280° C and tris(trimethylsilyl)phosphine (TMSP) was injected. Following the reaction, the flask was quickly cooled by applying compressed air, yielding InP QDs. The size and shape, which affect the optical properties of InP QSs, were controlled by modifying the reaction time. Typical reaction times were 10, 20 and 30 min a ZnS shell was added to the surface of InP QDs in the presence of

trioctylphosphine (top), trioctylphosphine oxide (TOPO), diethylzinc (ZnEt2) and hexamethyldisilathiane ((TMS)2S) at 145 °C, yielding InP/ZnS QDs. To functionalize InP/ZnS QDs with 1, 2-distearoyl-sn-glycero-3-phosphoethanolamine-N-[carboxy(polyethyleneglycol)-2000] [DSPE-PEG(2000)] carboxylic acid, InP/ZnS QDs were dissolved in chloroform along with 80% (v/v) of 1,2-dipalmitoyl-sn-glycero-3-phosphoethanolamine-N-[methoxy(polyethyleneglycol)-2000] (PEG-2-PE) and 20% of DSPE-PEG(2000) carboxylic acid. The solvent was evaporated by bubbling nitrogen gas through the solution, producing a dried layer of InP/ZnS QDs and PEG lipids. The dried film was then heated to 80 ◦C in a water bath for several minutes, and then cooled, yielding water-soluble carboxyl-functionalized InP/ZnS QDs coated PEG lipids (denoted as QInP). To functionalize InP/ZnS QDs with 1, 2-distearoyl-sn-glycero-3-phosphoethanolamine-N-[carboxy(polyethyleneglycol)-2000] [DSPE-PEG(2000)] carboxylic acid, InP/ZnS QDs were dissolved in chloroform along with 80% (v/v) of 1,2-dipalmitoyl-sn-glycero-3-phosphoethanolamine-N-[methoxy(polyethyleneglycol)-2000] (PEG-2-PE) and 20% of DSPE-PEG(2000) carboxylic acid. The solvent was evaporated by bubbling nitrogen gas through the solution, producing a dried layer of InP/ZnS QDs and PEG lipids. The dried film was then heated to 80 ◦C in a water bath for several minutes, and then cooled, yielding water-soluble carboxyl-functionalized InP/ZnS QDs coated PEG lipids (denoted as QInP).

Optical characterization Dilute solutions of QInP in deionized water were placed in 0.5 cm quartz cuvettes, and their absorption spectra were obtained using a Beckman DU 640B UV-VIS spectrophotometer (Beckman Coulter, Fullerton, CA, USA),

as previously described [41]. Photoluminescence spectra were obtained using a PerkinElmer LS-5 fluorescence spectrometer (PerkinElmer, Waltham, MA, USA).

Peptide preparation Four arginine-rich CPPs, SR9 (RRRRRRRRR), HR9 (CHHHHHRRRRRRRRRHHHHHC), PR9 (FFLIPKGRRRRRRRRR) and IR9 (GLFEAIEGFIENGWEGMIDGWYGRRRRRRRRR), were synthesized by Genomics (Taipei, Taiwan), as previously described [23–25, 36]. 2.4.

Gel retardation assay To prepare CPP/QInP complexes, various amounts of CPP peptides were incubated with QInP at molecular ratios of 0 (QInP alone), 10, 20, 30, 40 and 50 in phosphate buffered saline (PBS) at 37° C for 2 h. CPP/QInP complexes were analyzed by electrophoresis on a 0.5% agarose gel (Multi ABgarose, Thermo Fisher Scientific, Waltham, MA, USA) in 0.5× TAE (40 mM of Tris-acetate and 1 mM of EDTA, pH 8.0) buffer at 100 V for 40 min Images were captured using a Typhoon FLA 9000 biomolecular imager (GE Healthcare, Piscataway, NJ, USA) with the excitation wavelength at 473 nm (LD laser) and the emission above 473 nm (LPB filter) [43] for SR9/QInP complexes and a Typhoon Trio imager with the excitation wavelength at 532 nm (SYAG laser) and the emission above 532 nm for HR9/QInP and PR9/QInP complexes. Data were analyzed using ImageQuant TL 7.0 software (GE Healthcare).

Cell culture Human lung carcinoma A549 cells (American Type Culture Collection, Manassas, VA, USA; CCL-185) were maintained in Roswell Park Memorial Institute (RPMI) 1640 medium (Gibco, Invitrogen, Carlsbad, CA, USA) supplemented with 10% (v/v) bovine serum (Gibco) [33].

CPP-mediated QInP delivery into human cells A549 cells were seeded at a density of 1 × 104 per well of 96-well plates. For the transduction of noncovalent CPP/QInP complexes, 0, 50, 100 and 500 nM of CPPs (SR9, HR9 and PR9) were mixed with QInP at a molecular ratio of 30 at 37° C for 2 h. Without washing, CPP/QInP complexes were then incubated with cells at 37° C for 1 h. Samples were analyzed using a flow cytometer, a Zetasizer or a confocal microscope.

Flow cytometric analysis Cells were seeded at a density of 2.5 × 105 per well of 24-well plates. Cells in the control and experimental groups treated with QInP or CPP/QInP complexes were harvested and analyzed using a Cytomics FC500 flow cytometer (Beckman Coulter) with a FL1 filter for green fluorescent protein (GFP) detection [36].

Confocal and fluorescent microscopy Fluorescent and bright-field images were recorded using a BD Pathway 435 bioimaging system (BD Biosciences, Franklin Lakes, NJ, USA) [36]. This system without pinhole includes both fluorescent and confocal microscopic sets. Excitation filters were at 377/50, 482/35 and 543/22 nm for blue, green and red fluorescence, respectively. Emission filters were at 435LP (long-pass), 536/40 and 593/40 nm for blue (BFP), GFP and red fluorescent protein (RFP) channels, respectively. Bright-field microscopy was used to assess cell morphology. Confocal images were also obtained using a TCS SP5 II confocal microscope system (Leica, Wetzlar, Germany). The parameters for this confocal microscopy were as follows: excitation at 405 nm and emission at 435–480 nm for the detection of BFP; excitation at 488 nm and emission at 495–540 nm for the detection of GFP; and excitation at 543 nm and emission at 590–665 nm for the detection of RFP.

Zeta-potential measurement QInP (150 nM) or CPP/QInP complexes prepared at a molecular ratio of 30 were dissolved in double deionized water. To prepare CPP/QInP complexes, 4.5 M of CPPs (SR9, HR9, PR9 or IR9) were mixed with 150 nM of QInP at a molecular ratio of 30 (as well as 60 for IR9) in double deionized water, and incubated at 37° C for 2 h, as previously described [33]. Each solution was temperature equilibrated at 25 ◦C for 120 s in a zeta cell. Zeta-potentials of QInP or CPP/QInP complexes were analyzed using a Zetasizer Nano ZS with Zetasizer software 6.30 (Malvern Instruments, Worcestershire, UK) [42].

Subcellular colocalization analysis To examine subcellular localization of delivered CPP/QInP complexes, cells were treated with PBS, 500 nM of green fluorescent QInP alone or PR9/QInP complexes prepared at a molecular ratio of 30 at 37° C for 30 min, 1 h or 2 h. Cells were washed with PBS five times to remove free PR9/QInP complexes, followed by staining with fluorescent organelle-specific trackers, as previously described [36]. Organelle trackers, 16.2 μM of Hoechst 33342 (Invitrogen; in blue) at 37 ◦C for 40 min and 50 nM of LysoTracker DND-99 (Invitrogen; in red) at 37 ◦C for 30 min (according to the manufacturer's instructions), were used to visualize subcellular colocalization in nuclei and lysosomes, respectively. Fluorescent images were detected using a BD Pathway 435 bioimaging system (BD Biosciences) or a Leica confocal microscope system (Leica).

Cytotoxicity assay Cells were plated at a density of 1 × 104 per well in 96-well plates. Cells were treated with PBS as a negative control, treated with 100% dimethyl sulfoxide (DMSO) as a positive control, or treated with 25 nM–5 M of QInP or 500 nM of CPP/QInP complexes prepared at a molecular ratio of 30 at 37 ◦C for 1 h. The cells

were washed with PBS and cultured at 37 ◦C for 24 h. Cytotoxicity was measured by the SRB colorimetric assay [44].

Statistical analysis Results are expressed as mean ± standard deviation. Mean values and standard deviations were calculated from at least three independent experiments conducted with triplicates in each treatment group. Comparisons between the control and treated groups were performed by the Student's t-test using levels of statistical significance of $P < 0.05$ (*, †) and 0.01 (**, ††), as indicated.

RESULTS

Synthesis of carboxylated and PEGylated bifunctionalized InP/ZnS QDs

Water-soluble and carboxyl-functionalized InP/ZnS QDs were synthesized in three steps (Fig. 1A). Indium (III) acetate and tris(trimethylsilyl)phosphine were initially reacted in the presence of hexadecanoic acid and octadecane at 280 ◦C for 7 min in a simple one-step process. The resulting InP cores were protected with a ZnS shell, and then functionalized by PEG-2-PE and DSPE-PEG (2000) carboxylic acid. Water-soluble, PEGylated and carboxylated bifunctionalized InP/ZnS QDs were obtained (denoted as QInP).

Optical characterization of QInP The absorption spectra of QInP exhibited its first excitation peak in the range of 400–500 nm, depending on the reaction conditions employed (Fig. 1B). The photoluminescence spectra of QInP prepared at 10 min had a maximal emission peak wavelength at 525 nm. The maximal emission peak shifted to 550 and 580 nm when QInP prepared at 20 and 30 min, respectively. This red-shift in the photoluminescence correlates with an increase in particle size.

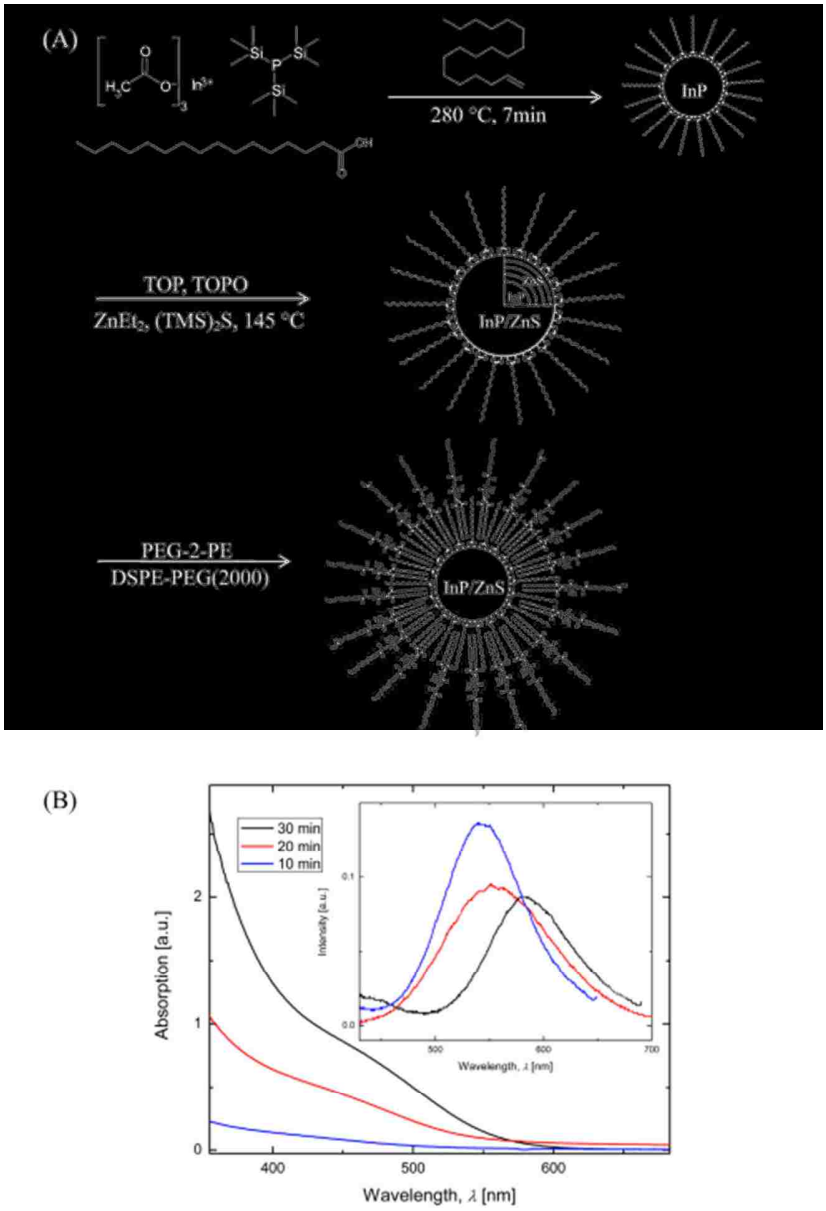

Figure. 1. Synthesis and optical characterization of carboxylated and PEGylated bifunctionalized InP/ZnS QDs (QInP). (A) Synthesis and schematic structure of QInP. TOP = trioctylphosphine, TOPO = trioctylphosphine oxide, ZnEt2 = diethylzinc, (TMS)2S = hexamethyldisilathiane, PEG-2-PE = 1,2-dipalmitoyl-sn-glycero-3-phosphoethanolamine-N-[methoxy(polyethyleneglycol)-2000], DSPE-PEG(2000) = 1,2-distearoyl-sn-glycero-3-phosphoethanolamine-N-[carboxy(polyethyleneglycol)-2000]. (B) The absorption and photoluminescence (inset) spectra of QInP synthesized at 10 (blue lines), 20 (red lines), and 30 min (black lines) of reaction time. The absorption spectra of QInP were scanned using a Beckman DU 640B UV-VIS spectrophotometer, and the photoluminescence spectra of QInP were measured using a PerkinElmer LS-5 fluorescence spectrometer. (For interpretation of the references to colour in this figure legend, the reader is referred to the web version of this article.)

Interactions between QInP and CPPs An agarose-based gel retardation assay was conducted to determine whether CPP forms stable complexes with QInP in vitro. CPPs (SR9, HR9 or PR9) were incubated with QInP at various ratios. QInP exhibited a reduced mobility when incubated with CPPs, and the mobility decreased as the concentration of CPPs increased (Fig. 2A–C). These data indicate that CPPs can interact with QInP to form stable, noncovalent complexes.

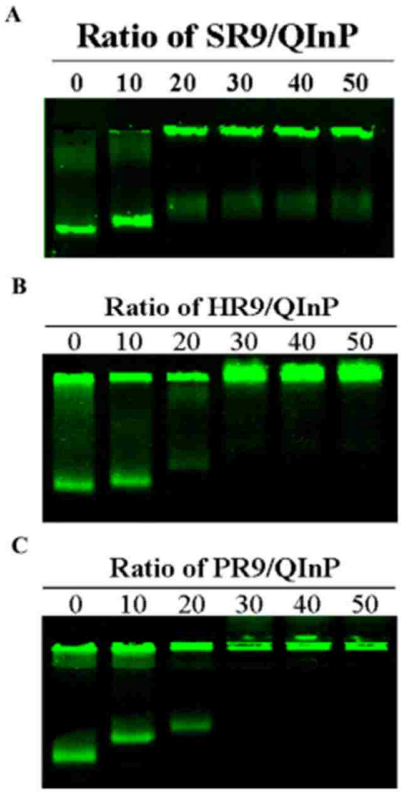

Figure 2. Noncovalent interactions between CPPs and QInP using gel retardation assay. (A) SR9/QInP complexes. (B) HR9/QInP complexes. (C) PR9/QInP complexes. CPPs (SR9, HR9 or PR9) and QInP were incubated at molecular ratios of 0 (QInP alone), 10, 20, 30, 40 and 50. After the incubation with agitation for 2 h, the complexes were analyzed by electrophoresis on a 0.5% agarose gel. QInP fluorescence was captured using a Typhoon FLA 9000 biomolecular and Typhoon Trio imagers (GE Healthcare).

CPP-mediated intracellular delivery of QInP To assess whether CPPs can deliver QInP into cells, human A549 cells were treated with CPP/QInP complexes prepared at a molecular ratio of 30. Green fluorescence was detected in cells treated with CPP/QInP complexes using a flow cytometer, when the concentration of QInP was above 500 nM (Fig. 3A). Using a fluorescent microscope, green fluorescence was observed in the cells treated with CPP/QInP complexes, but not in the cells treated with QInP alone (Fig. 5.3B). These results demonstrate that CPPs can deliver noncovalently complexed QInP into cells.

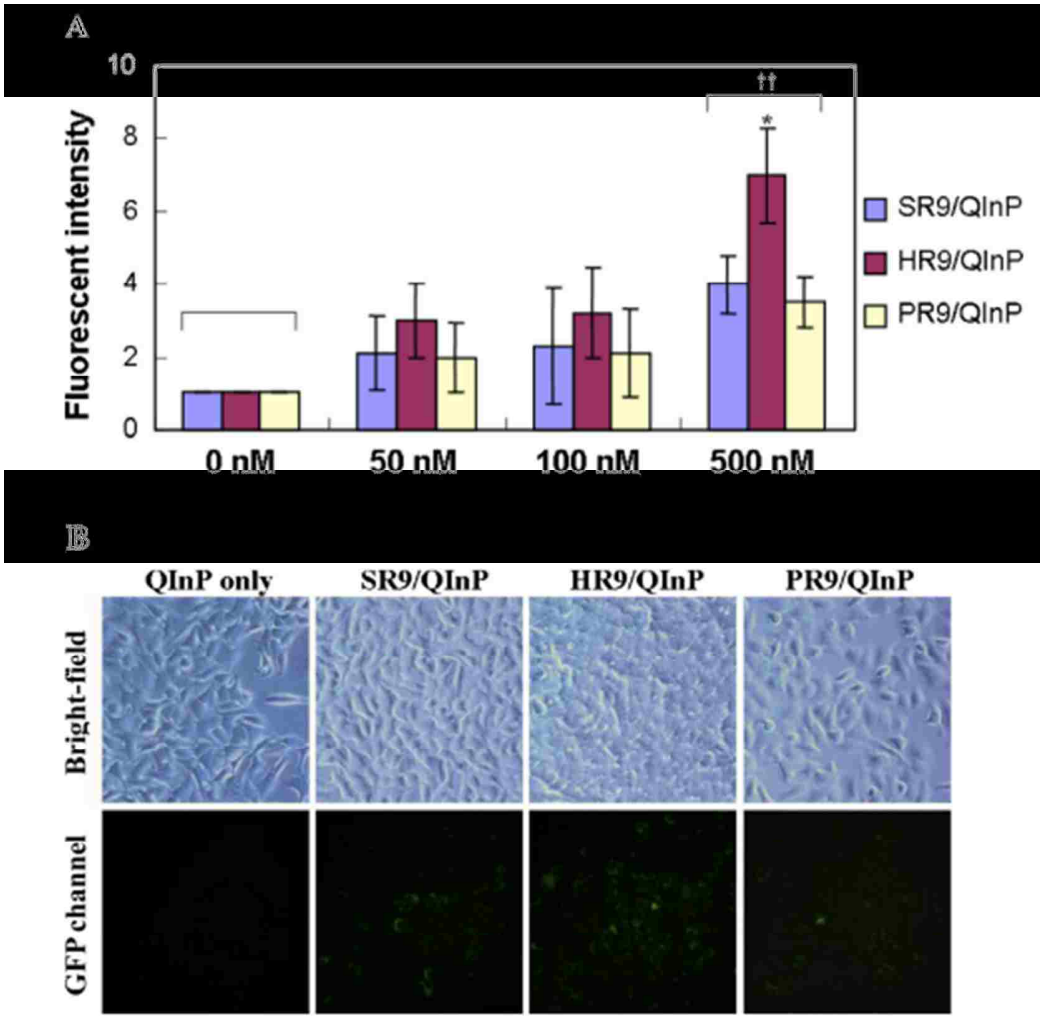

Figure 3. Intracellular delivery of CPP/QInP complexes. (A) Fluorescent intensity of cells treated with different concentrations of CPP/QInP complexes. Cells were treated with 0 (QInP alone), 50, 100 and 500 nM CPP/QInP complexes prepared at a molecular ratio of 30 for 1 h. Each CPP/QInP complex group was compared to that of the 0 nM group. Data are presented as mean ± standard deviation from five independent experiments conducted in triplicates per treatment group. Significant differences of $P < 0.05$ (*) for individual comparison within the same group and $P < 0.01$ (††) for group comparison are indicated. (B) Microscopy of CPP-mediated QInP delivery into cells. Fifteen μM CPPs (SR9, HR9 and PR9) were mixed with 500 nM QInP to form complexes. Cells were treated with QInP alone or CPP/QInP complexes for 1 h and observed using a fluorescent microscope.

To interpret the relationship between transduction efficiency and charging state of CPP/QInP complexes, cells treated with QInP and CPP/QInP complexes were characterized using a flow cytometer, and QInP and CPP/QInP complexes were determined using a zeta-potential analyzer. Using a flow cytometer, cell population fractions with green fluorescence were detected in the cells treated with CPP/QInP complexes prepared at a molecular ratio of 30 (60 for IR9/QInP complexes) (Fig. 4A). The zeta-potential of QInP was electronegative (−32.0 ± 1.7 mV) (Fig. 4B). Zeta-potentials of CPP/QInP complexes prepared at a molecular ratio of 30 (60 for IR9/QInP complexes) were more electropositive. These data indicate that charging state of CPP/QInP complexes correlate with transduction efficiency.

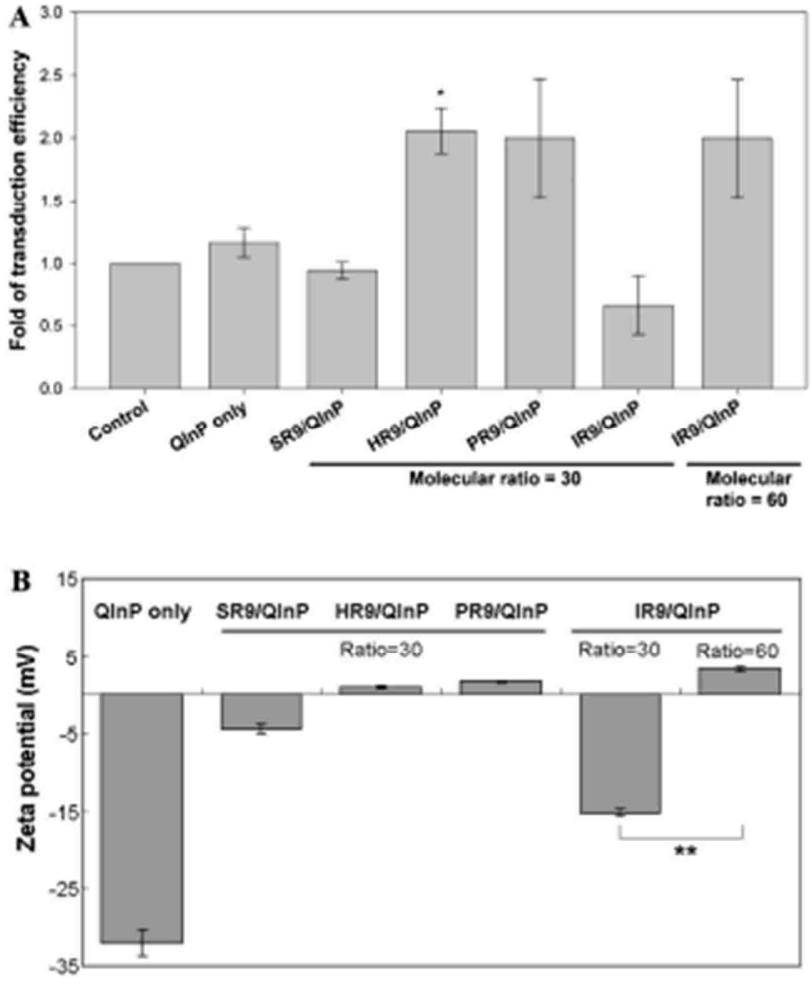

Figure 4. Intracellular delivery and physicochemical properties of CPP/QInP complexes. (A) Flow cytometric analysis of CPP-mediated QInP delivery into A549 cells.Cells were treated with QInP alone, SR9/QInP, HR9/QInP, PR9/QInP or IR9/QInP complexes prepared at a molecular ratio of 30 or 60 for IR9/QInP complexes for 24 h, as indicated. Cells without any treatment served as the control. The fluorescent intensity and population of positive cells was analyzed using a flow cytometer. Data are presented as mean ± standard deviation from three independent experiments conducted in triplicates per treatment group. (B) Surfaced-electrical charges of different CPP/QInP complexes. SR9, HR9, and PR9 were incubated with QInP at a molecular ratio of 30, while IR9 was incubated with QInP at molecular ratios of 30 and 60. Zeta potentials of QInP and CPP/QInP complexes were determined using a Zetasizer. Data are presented as mean ± standard deviation from three independent experiments conducted in triplicates per treatment group. Significant differences were determined at $P < 0.05$ (*) and $P < 0.01$ (**).

To reveal subcellular localization of CPP/QInP complexes, cells were treated with PBS, QInP or PR9/QInP complexes and stained with organelle-specific fluorescent markers LysoTracker DND-99 and Hoechst 33342 for the visualization of lysosomes and nuclei, respectively. The majority of QInP distributed evenly in the cytosol following PR9-mediated delivery (Fig. 5 A and B). The merged images revealed that QInP colocalized with lysosomes in most cells after transduction delivery. This result is consistent with our previous finding that endocytosis is the main route for intracellular delivery of PR9/cargo complexes (manuscript submitted).

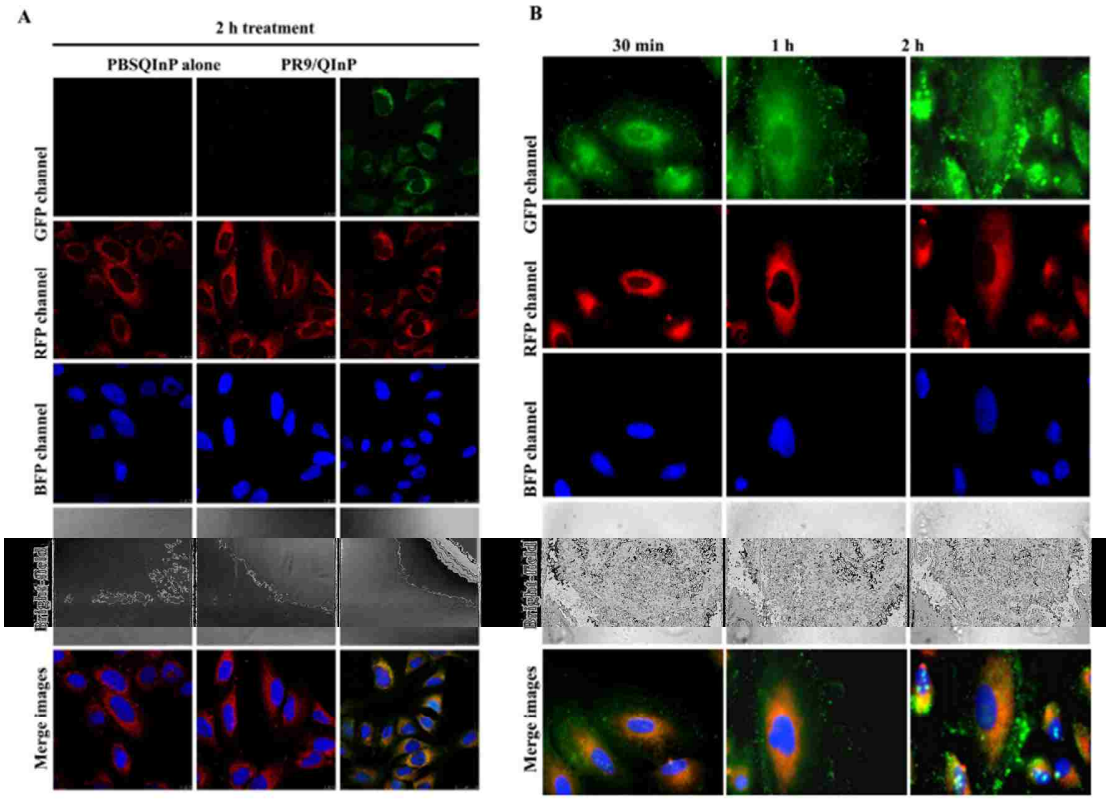

Figure 5. Subcellular colocalization of PR9/QInP complexes. (A) Subcellular colocalization of QInP alone and PR9/QInP complexes. A549 cells were treated with PBS and QInP alone as controls or PR9/QInP complexes for 2 h, stained with LysoTracker DND-99 and Hoechst 33342, and then observed using a Leica confocal microscope system at a magnification of 600×. (B) Subcellular colocalization of PR9/QInP complexes at various time periods. A549 cells were treated with PR9/QInP complexes for 30 min, 1 h or 2 h, stained with LysoTracker DND-99 and Hoechst 33342, and then observed using a BD Pathway bioimaging system at a magnification of 600×. GFP, RFP and BFP channels displayed the distribution of QInP, lysosomes and nuclei, respectively. Overlaps between QInP and lysosomes were yellow/orange color in merged GFP and RFP images. (For interpretation of the references to colour in this figure legend, the reader is referred to the web version of this article.)

Cytotoxicity of CPP/QInP complexes To determine the effect of QInP and CPP/QInP complexes on cell viability, the SRB assay was performed. QInP had no significant effect on cell viability at or below 1 M (Fig. 6A), while 500 nM of CPPs (SR9,

HR9 or PR9) complexed with QInP at a molecular ratio of 30 were not cytotoxic (Fig. 6B). We have previously demonstrated that QDs and CPP/QD complexes are not toxic to A549 cells by the SRB assay [33,36].

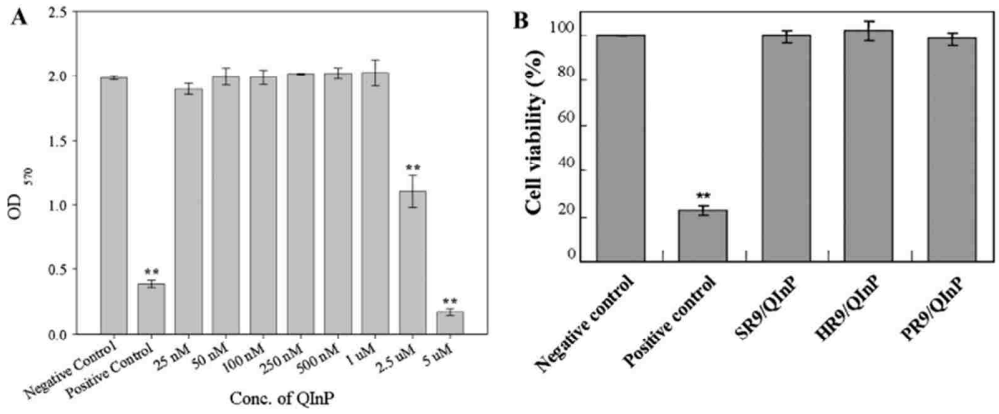

Figure. 6. Cytotoxicity of QInP and CPP/QInP complexes using the SRB assay. (A) Influence of QInP on A549 cell viability. Cells were treated with different amounts of QInP ranging from 25 nM to 5 μM. (B) Influence of CPP/QInP complexes on cell viability. Cells were treated with 500 nM CPPs (SR9, HR9 or PR9) complexed with QInP at a molecular ratio of 30. Cells without any treatment served as a negative control, and cells treated with 100% DMSO were served as a positive control. Each group is compared with the negative control, and significant differences of $P < 0.01$ (**) are indicated. Data are presented as mean ± standard deviation from three independent experiments conducted in triplicates per treatment group.

DISCUSSION

The novel physicochemical characteristics give semiconductor QDs specific advantages in certain research and medical applications [45]. Potentially the most important application of QDs is their use as diagnostic and therapeutic tools in

nanomedicine [45]. In this study, we synthesized novel water-soluble, PEGylated and carboxyl-functionalized InP/ZnS QDs. Their physicochemical properties, including optical features, morphology and charging state, and cellular internalization of QInP and CPP/QInP complexes were characterized. We found that CPPs can deliver noncovalently complexed QInP into live cells. PR9/QInP complexes were localized in lysosomes. This is consistent with the notion that endocytosis is the major route for cellular entry. Finally, cell viability assays showed that CPP/QInP complexes were not cytotoxic when 500 nM of CPP was complexed with QInP at a molecular ratio of 30, and QInP did not result in significant cytotoxicity when the concentrations were at or less than 1 μM.

Functionalized nanoparticles have become key players for enhancing the contrast of images in molecular imaging and medical diagnostics [46]. Since the late 1980s, a large number of binary III-V materials, such as gallium phosphide (GaP) and InP, exhibiting infrared bandgaps as bulk semiconductors, were prepared as solution-based nanocrystals [47]. Many research teams have been using cadmium-free QDs, such as InP, to address concerns about cadmium cytotoxicity [48]. One key advantage offered by InP QDs lies in the robustness of the covalent bond in III-V semiconductors versus the ionic bond in the II-VI semiconductors and, thus, reduced toxicity. InP QDs with promising size-tunable emission in the near infrared and visible range have emerged as a replacement for cadmium-based QDs [49]. However, reports on colloidal synthesis of InP QDs are few, and size homogeneity has been limited [49]. Nag and Sarma reported an efficient and fast solvothermal route to prepare InP QDs [50]. This method used a reaction temperature as high as 430 ◦C, accelerating the reaction.

A ZnS shell on the surface of solvothermal synthesized InP QDs could be surface-modified with hydrophilic ligands in an aqueous solution at room temperature [51]. The resulting InP/ZnS QDs exhibit enhanced luminescent efficiency relative to InP QDs. The ZnS shells serve two purposes: (1) improving the quantum yield by passivating the surface nonradiative recombination sites and (2) acting as a barrier between the inorganic core and the surrounding solvent, thereby preventing the leakage of unwanted ions [52]. Chibli et al. reported survival assays in five cell lines, and showed a distinct reduction in toxicity with the double-shell InP QDs, compared to a single ZnS shell [49]. These results indicated that InP QDs could be an effective alternative to cadmium-containing QDs. Recently, large-scale synthesis of InP/ZnS QDs was conducted in a hybrid flow reactor that combined a batch-type mixer with a flowrate furnace in a simple one-step process [53]. The same group also reported that uniform, large InP/ZnS QDs could be produced using a newly synthesized organometallic phosphorus (P) precursor, tris(tert-butyldimethylsilyl)phosphine, and a low temperature regime (210–300 ◦C) [54]. Large-area freestanding films of InP/ZnS QDs over 50 cm × 50 cm were recently reported [55].

Surface functionalization of amphipathic InP QDs with folate rendered endocytosis of folate receptor-mediated delivery of InP QDs in folate-receptor-positive KB cells [52]. Gao et al. reported that InAs/InP/ZnSe QDs functionalized with mercaptopropionic acid (MPA) accumulated in the tumor area of nude mice bearing 22B or LS174T tumors [56]. Furthermore, InAs/InP/ZnSe QDs functionalized with the arginine-glycine-aspartic acid (RGD) tripeptide could be recognized by the cell adhesion molecule integrin $\alpha v\beta 3$, a key player in tumor angiogenesis, progression and

spread [57]. Recently, dendron- and dendron-(RGD) 2-functionalized InP QDs have been introduced as translatable nanoprobes for clinical imaging applications [58]. Dendron-coated InP/ZnS QDs lacked significant toxicity at exposure doses of 1 μg InP/g mouse weight. These InP QDs exhibited important features, including high stability, biocompatibility, near-infrared emission and nontoxicity. Comparisons were also been made between doxorubicin (Dox)-functionalized gold (Au) nanoparticles and Dox functionalized InP QDs as tools for therapeutic effectiveness [59]. Our InP QDs had no effect on cell viability at or below 1 μM. In the future, QInP can be functionalized with activatable cell-penetrating peptides (ACPPs) to inhibit target gene expression by RNA interference (RNAi) for biological applications.

There have been few investigations on the use of CPPs with InP QDs. Rosenberg et al. functionalized InP/ZnS QDs with CAAKATatCPPs, forming QD-CAAKATat-DOTA-Dy, where DOTA and Dy are 1,4,7,10-tetraazacyclododecane-N,N',N'',N'''-tetra acetic acid and dysprosium3+, respectively [60]. They found that QD-CAAKATat-DOTA-Dy were located in vesicular compartments, and were not cytotoxic to Chinese hamster ovary (CHO) cells. The incorporation of Tat peptide provided effective self-transfecting properties. Stasiuk et al. reported functionalization of InP/ZnS QDs with maurocalcine (MC) CPPs from scorpion toxin [46]. Fluorescent MC-InP QDs showed cellular internalization with bright magnetic resonance imaging signal, and increased tissue retention time. Our present study reveals the utility of three additional kinds of arginine-rich CPPs to deliver QInP for biological applications.

CONCLUSIONS

We synthesized and characterized carboxylated and PEGylated bifunctionalized InP/ZnS QDs (QInP). CPPs (SR9, HR9, PR9 and IR9) were able to deliver noncovalently complexed QInP into human A549 cells. These results indicate that bifunctionalized QInP may be an excellent biocompatible tool for biomedical imaging and drug delivery applications. Notably, the present synthetic protocol of QInP could be easily extended to produce additional functionalized QDs as multimodal imaging agents in the future.

ACKNOWLEDGMENTS

We are grateful to Chia-Liang Cheng (Department of Physics, National Dong Hwa University, Taiwan) for performing the zeta potential measurements, and Core Instrument Center (National Health Research Institutes, Miaoli, Taiwan) for the Typhoon Trio imager and Leica TCS SP5 II confocal system. This work was supported by the Postdoctoral Fellowship NSC 101-2811-B-259-001 (to B.R. Liu) and the Grant Number NSC 101-2320-B-259-002-MY3 from the National Science Council of Taiwan (to H.-J. Lee).

REFERENCES

[1] A.P. Alivisatos, Semiconductor clusters, nanocrystals, and quantum dots, Science 271 (1996) 933–937.

[2] H. Mattoussi, G. Palui, H.B. Na, Luminescent quantum dots as platforms for probing in vitro and in vivo biological processes, Adv. Drug Deliv. Rev. 64 (2012) 138–166.

[3] K.T. Yong, Quantum dots for biophotonics, Theranostics 2 (2012) 629–630.

[4] M. Bruchez, M. Moronne, P. Gin, S. Weiss, A.P. Alivisatos, Semiconductor nanocrystals as fluorescent biological labels, Science 281 (1998) 2012–2016.

[5] W.C.W. Chan, S. Nie, Quantum dot bioconjugates for ultrasensitive nonisotopic detection, Science 281 (1998) 2016–2018.

[6] F. Chen, D. Gerion, Fluorescent CdSe/ZnS nanocrystal-peptide conjugates for long-term, nontoxic imaging and nuclear targeting in living cells, Nano Lett. 4 (2004) 1827–1832.

[7] X. Michalet, F.F. Pinaud, L.A. Bentolila, J.M. Tsay, S. Doose, J.J. Li, G. Sundaressan, A.M. Wu, S.S. Gambhir, S. Weiss, Quantum dots for live cells, in vivo imaging, and diagnostics, Science 307 (2005) 538–544.

[8] L. Shao, Y. Gao, F. Yan, Semiconductor quantum dots for biomedical applica-tions, Sensors 11 (2011) 11736–11751.

[9] Y. Zhang, T.H. Wang, Quantum dot enabled molecular sensing and diagnostics, Theranostics 2 (2012) 631–654.

[10] P.M. Farias, B.S. Santos, A. Fontes, Semiconductor fluorescent quantum dots:efficient biolabels in cancer diagnostics, Methods Mol. Biol. 544 (2009) 407–419.

[11] R. Hu, W.C. Law, G. Lin, L. Ye, J. Liu, J. Liu, L. Reynolds, K.T. Yong, PEGylated phospholipid micelle-encapsulated near-infrared PbS quantum dots for in vivo and in vitro bioimaging, Theranostics 2 (2012) 723–733.

[12] F. Madani, S. Lindberg, U. Langel, S. Futaki, A. Graslund, Mechanisms of cellular uptake of cell-penetrating peptides, J. Biophys. 2011 (2011) 414729.

[13] I. Mager, K. Langel, T. Lehto, E. Eiriksdottir, U. Langel, The role of endocytosis on the uptake kinetics of luciferin-conjugated cell-penetrating peptides, Biochim. Biophys. Acta 1818 (2012) 502–511.

[14] A. van den Berg, S.F. Dowdy, Protein transduction domain delivery of therapeutic macromolecules, Curr. Opin. Biotechnol. 22 (2011) 888–893.

[15] N. Schmidt, A. Mishra, G.H. Lai, G.C. Wong, Arginine-rich cell-penetrating peptides, FEBS Lett. 584 (2010) 1806–1813.

[16] M. Green, P.M. Loewenstein, Autonomous functional domains of chemically synthesized human immunodeficiency virus Tat trans-activator protein, Cell 55 (1988) 1179–1188.

[17] A.D. Frankel, C.O. Pabo, Cellular uptake of the Tat protein from human immunodeficiency virus, Cell 55 (1988) 1189–1193.

[18] K.M. Wagstff, D.A. Jans, Protein transduction: cell penetrating peptides and their therapeutic applications, Curr. Med. Chem. 13 (2006) 1371–1387.

[19] A. Gautam, H. Singh, A. Tyagi, K. Chaudhary, R. Kumar, P. Kapoor, G.P. Raghava, CPPsite: a curated database of cell penetrating peptides, Database 2012 (2012) bas015.

[20] I. Nakase, Y. Konishi, M. Ueda, H. Saji, S. Futaki, Accumulation of argininerich cell-penetrating peptides in tumors and the potential for anticancer drug delivery in vivo, J. Control. Release 159 (2012) 181–188.

[21] J.M. Gump, S.F. Dowdy, Tat transduction: the molecular mechanism and therapeutic prospects, Trends Mol. Med. 13 (2007) 443–448.

[22] J.S. Wadia, S.F. Dowdy, Protein transduction technology, Curr. Opin. Biotechnol. 13 (2002) 52–56.

[23] Y.H. Dai, B.R. Liu, H.J. Chiang, H.J. Lee, Gene transport and expression by arginine-rich cell-penetrating peptides in Paramecium, Gene 489 (2011) 89–97.

[24] Y.J. Chen, B.R. Liu, Y.H. Dai, C.Y. Lee, M.H. Chan, H.H. Chen, H.J. Chiang, H.J. Lee, A gene delivery system for insect cells mediated by arginine-rich cell-penetrating peptides, Gene 493 (2012) 201–210.

[25] B.R. Liu, M.D. Lin, H.J. Chiang, H.J. Lee, Arginine-rich cell-penetrating peptides deliver gene into living human cells, Gene 505 (2012) 37–45.

[26] G. Tunnemann, G. Ter-Avetisyan, R.M. Martin, M. Stockl, A. Herrmann, M.C. Cardoso, Live-cell analysis of cell penetration ability and toxicity of oligo-arginines, J. Pept. Sci. 14 (2008) 469–476.

[27] K. Kilk, R. Mahlapuu, U. Soomets, U. Langel, Analysis of in vitro toxicity of five cell-penetrating peptides by metabolic profiling, Toxicology 265 (2009) 87–95.

[28] J. Suhorustsenko, N. Oskolkov, P. Arukuusk, K. Kurrikoff, E. Eriste, D.M. Copolovici, U. Langel, Cell-penetrating peptides, PepFects, show no evidence of toxicity and immunogenicity in vitro and in vivo, Bioconjug. Chem. 22 (2011) 2255–2262.

[29] J.B. Delehanty, H. Mattoussi, I.L. Medintz, Delivering quantum dots into cells:strategies, progress and remaining issues, Anal. Bioanal. Chem. 393 (2009) 1091–1105.

[30] F.L. Xue, J.Y. Chen, J. Guo, C.C. Wang, W.L. Yang, P.N. Wang, D.R. Lu, Enhancement of intracellular delivery of CdTe quantum dots (QDs) to living cells by Tatconjugation, J. Fluoresc. 17 (2007) 149–154.

[31] Y.E. Koshman, S.B. Waters, L.A. Walker, T. Los, P. de Tombe, P.H. Goldspink, B. Russell, Delivery and visualization of proteins conjugated to quantum dots in cardiac myocytes, J. Mol. Cell. Cardiol. 45 (2008) 853–856.

[32] Y. Wei, N.R. Jana, S.J. Tan, J.Y. Ying, Surface coating directed cellular delivery of Tat-functionalized quantum dots, Bioconjug. Chem. 20 (2009) 1752–1758.

[33] B.R. Liu, J.F. Li, S.W. Lu, H.J. Lee, Y.W. Huang, K.B. Shannon, R.S. Aronstam, Cellular internalization of quantum dots noncovalently conjugated with arginine-rich cell-penetrating peptides, J. Nanosci. Nanotech. 10 (2010) 6534–6543.

[34] B.R. Liu, Y.W. Huang, H.J. Chiang, H.J. Lee, Cell-penetrating peptide-functionized quantum dots for intracellular delivery, J. Nanosci. Nanotechnol. 10 (2010) 7897–7905.

[35] Y. Xu, B.R. Liu, H.J. Lee, K.B. Shannon, J.G. Winiarz, T.C. Wang, H.J. Chiang, Y.W. Huang, Nona-arginine facilitates delivery of quantum dots into cells via multiple pathways, J. Biomed. Biotechnol. 2010 (2010) 948543.

[36] B.R. Liu, Y.W. Huang, J.G. Winiarz, H.J. Chiang, H.J. Lee, Intracellular delivery of quantum dots mediated by a histidine- and arginine-rich HR9 cell-penetrating peptide through the direct membrane translocation mechanism, Biomaterials 32 (2011) 3520–3537.

[37] N. Depalo, A. Mallardi, R. Comparelli, M. Striccoli, A. Agostiano, M.L. Curri, Luminescent nanocrystals in phospholipid micelles for bioconjugation: an optical and structural investigation, J. Colloid Interface Sci. 325 (2008) 558–566.

[38] Y. Shi, P. He, X. Zhu, Photoluminescence-enhanced biocompatible quantum dots by phospholipid functionalization, Mater. Res. Bull. 43 (2008) 2626–2635.

[39] J.A. Gerbec, D. Magana, A. Washington, G.F. Strouse, Microwave-enhanced reaction rates for nanoparticle synthesis, J. Am. Chem. Soc. 127 (2005) 15791–15800.

[40] B.O. Dabbousi, J. Rodriguez-Viejo, F.V. Mikulec, J.R. Heine, H. Mattoussi, R. Ober, K.F. Jensen, M.G. Bawendi, (CdSe)ZnS core-shell quantum dots: synthesis and characterization of a size series of highly luminescent nanocrystallites, J. Phys. Chem. B 101 (1997) 9463–9475.

[41] T.M. Fears, C. Anderson, J.G. Winiarz, Photorefractivity in a polymeric composite photosensitized with NiS nanocrystals, J. Chem. Phys. 129 (2008) 154704.

[42] B.R. Liu, H.J. Chiang, Y.W. Huang, M.H. Chan, H.H. Chen, H.J. Lee, Cellular internalization of quantum dots mediated by cell-penetrating peptides, Pharm. Nanotechnol. 1 (2013) 151–161.

[43] J.S. Liou, B.R. Liu, A.L. Martin, Y.W. Huang, H.J. Chiang, H.J. Lee, Protein transduction in human cells is enhanced by cell-penetrating peptides fused with an endosomolytic HA2 sequence, Peptides 37 (2012) 273–284.

[44] J.W. Hu, B.R. Liu, C.Y. Wu, S.W. Lu, H.J. Lee, Protein transport in human cells mediated by covalently and noncovalently conjugated arginine-rich intracellular delivery peptides, Peptides 30 (2009) 1669–1678.

[45] M.J.D. Clift, V. Stone, Quantum dots: an insight and perspective of their biological interaction and how this relates to their relevance for clinical use, Theranostics 2 (2012) 668–680.

[46] G.J. Stasiuk, S. Tamang, D. Imbert, C. Poillot, M. Giardiello, C. Tisseyre, E.L. Barbier, P.H. Fries, M. de Waard, P. Reiss, M. Mazzanti, Cell-permeable Ln(III) chelatefunctionalized InP quantum dots as multimodal imaging agents, ACS Nano 5 (2011) 8193–8201.

[47] A.L. Rogach, A. Eychmuller, S.G. Hickey, S.V. Kershaw, Infrared-emitting colloidal nanocrystals: synthesis, assembly, spectroscopy, and applications, Small 3 (2007) 536–557.

[48] K.T. Young, Y. Wang, I. Roy, H. Rui, M.T. Swihart, W.C. Law, S.K. Kwak, L. Ye, J. Liu, S.D. Mahajan, J.L. Reynolds, Preparation of quantum dot/drug nanoparticles formulations for traceable targeted delivery and therapy, Theranostics 2 (2012) 681–694.

[49] H. Chibli, L. Carlini, S. Park, N.M. Dimitrijevic, J.L. Nadeau, Cytotoxicity of InP/ZnS quantum dots related to reactive oxygen species generation, Nanoscale 3 (2011) 2552–2559.

[50] A. Nag, D.D. Sarma, Solvothermal synthesis of InP quantum dots, J. Nanosci. Nanotechnol. 9 (2009) 5633–5636.

[51] H.J. Byun, J.C. Lee, H. Yang, Solvothermal synthesis of InP quantum dots and their enhanced luminescent efficiency by post-synthetic treatments, J. Colloid Interface Sci. 355 (2011) 35–41.

[52] D.J. Bharali, D.W. Lucey, H. Jayakumar, H.E. Pudavar, P.N. Prasad, Folatereceptor-mediated delivery of InP quantum dots for bioimaging using confocal and two-photon microscopy, J. Am. Chem. Soc. 127 (2005) 11364–11371.

[53] K. Kim, S. Jeong, J.Y. Woo, C.S. Han, Successive and large-scale synthesis of InP/ZnS quantum dots in a hybrid reactor and their application to white LEDs, Nanotechnology 23 (2012) 065602.

[54] S. Joung, S. Yoon, C.S. Han, Y. Kim, S. Jeong, Facile synthesis of uniform large-sized InP nanocrystal quantum dots using tris(tertbutyldimethylsilyl)phosphine, Nanoscale Res. Lett. 7 (2012) 93.

[55] E. Mutlugun, P.L. Hernandez-Martinez, C. Eroglu, Y. Coskun, T. Erdem, V.K. Sharma, E. Unal, S.K. Hickey, N. Gaponik, A. Eychmuller, H.V. Demir, Large area (over 50 cm × 50 cm) freestanding films of colloidal InP/ZnS quantum dots, Nano Lett. 12 (2012) 3986–3993.

[56] J. Gao, K. Chen, R. Xie, J. Xie, S. Lee, Z. Cheng, X. Peng, X. Chen, Ultrasmall near infrared non-cadmium quantum dots for in vivo tumor imaging, Small 6 (2010) 256–261.

[57] J. Gao, K. Chen, R. Xie, J. Xie, Y. Yan, Z. Cheng, X. Peng, X. Chen, In vivo tumor targeted fluorescence imaging using near-infrared non-cadmium quantum dots, Bioconjug. Chem. 21 (2010) 604–609.

[58] J. Gao, K. Chen, R. Luong, D.M. Bouley, H. Mao, T. Qiao, S.S. Gambhir, Z. Cheng, A novel clinically translatable fluorescent nanoparticles for targeted molecular imaging of tumors in living subjects, Nano Lett. 12 (2012)281–286.

[59] X. Zhang, H. Chibli, D. Kong, J. Nadeau, Comparative cytotoxicity of gold doxorubicin and InP-doxorubicin conjugates, Nanotechnology 23 (2012) 275103.

[60] J.T. Rosenberg, J.M. Kogot, D.D. Lovingood, G.F. Strouse, S.C. Grant, Intracellular bimodal nanoparticles based on quantum dots for high-field MRI at 21.1 T, Magn. Reson. Med. 64 (2010) 871–882.

V. SPECIFIC INTRACELLULAR UPTAKE OF HERCEPTIN-CONJUGATED CdSe/ZnS QUANTUM DOTS INTO BREAST CANCER CELLS

ABSTRACT

Herceptin, a typical monoclonal antibody, was immobilized on the surface of CdSe/ZnS core-shell quantum dots (QDs) to enhance their specific interactions with breast cancer cells (SK-BR3). The mean size of the core-shell quantum dots (28 nm), as determined by dynamic light scattering, increased to 86 nm after herceptin immobilization. The in vitro cell culture experiment showed that the keratin forming cancer cells (KB) proliferated well in the presence of herceptin-conjugated QDs (QD-Her, 5 nmol/mL), whereas most of the breast cancer cells (SK-BR3) had died. To clarify the mechanism of cell death, the interaction of SK-BR3 cells with QD-Her was examined by confocal laser scanning microscopy. As a result, the QD-Her bound specifically to the membrane of SK-BR3, which almost became saturated a after 6 hours incubation. This suggests that the growth signal of breast cancer cells is inhibited completely by the specific binding of herceptin to the Her-2 receptor of SK-BR3 membrane, resulting in cell death.

INTRODUCTION

The development of noncytotoxic quantum dots (QDs) has attracted considerable interest as luminescence probes in biological and medical research because of their some unique optical and chemical properties [1], such as a tunable fluorescence wavelength according to size, a sharp and symmetrical fluorescence peak, strong and stable emission, high quantum yield, brightness, and photo stability [2–5]. QDs have several advantages

over traditional dyes and fluorescent proteins used as imaging probes, such as tunable emission from visible to infrared wavelengths, broader excitation spectra, and high resistance to photo bleaching [6, 7]. On the other hand, the potential applications of QDs in biology and medicine are limited because of their toxic effects [8]. QDs contain toxic components, such as cadmium or lead. Cd2+ and Pb2+ can be released from QDs to kill the cells [9]. Recently, a number of techniques, such as a gold outer shell [10], targeted ligand-like peptide [11], proteins [12, 13], and polymer coating [14] have been developed to minimize the cytotoxicity of Consequently, many approaches for transforming QDs from hydrophobic to hydrophilic have been developed for a range of biomedical applications. Accordingly, researchers have also used noncytotoxic materials, such as polyethylene glycol (PEG) and polymaleic anhydride salt-1-tetradecene, to coat the surfaces of QDs [15].

Thus far, a range of surface coatings of QDs have been explored including the conjugation of mercaptoacetic acid [16], mercaptopropionic acid [17], mercaptobenzoic acid [18], and biocompatible and chemically functionalizable inorganic shells, such as silica or zinc sulfide [19]. These coatings can guarantee the water solubility of QDs but cannot enhance the biocompatibility significantly. Therefore, further coatings with suitable water-soluble organic ligand/biomolecules are necessary to enhance the biocompatibility of QDs. To that end, QDs have been linked covalently with biorecognition molecules, such as biotin [20], oleic acid [21], peptides [22], bovine serum albumin [23], transferrin [24], antibodies [25], and DNA [26].

Polymeric micelles have been studied extensively for the solubilization of hydrophobic drugs and bioactive agents because of their unique properties, including

nanoscale size, high water solubility, high structural stability, high carrying capacity of hydrophobic agents, and easy introduction of functional moieties to the outer shell. The polymers generally leave the fluorescent properties of QDs unchanged but allow the introduction of other moieties to the QD surfaces [27]. CdSe/ZnS QD is a versatile core shell material with a wide band gap of 3.37 eV and a rather large exciton binding energy that makes the exciton state stable, even at room temperature. Zinc is a very important trace element in humans [28] and has been found to play an important part in many biological systems [29–32]. Therefore, CdSe/ZnS core-shell QDs are expected to be environmentally friendly and more suitable for bioimaging and cancer detection than CdSe QD.

In this study, breast cancer cells were targeted with herceptin-conjugated quantum dots for cancer therapy and diagnosis. Phospholipid-immobilized CdSe/ZnS core-shell quantum dots (QDs) were prepared by a coupling reaction of trioctylphosphine oxide-coated CdSe/ZnS core-shell quantum dots with carboxylic acid-terminated PEG and methoxy-terminated PEG. Herceptin was then introduced to the surface of the QDs (QD-Her) to enhance the antitumor effects of chemotherapeutic agents without increasing their toxicity [33–36]. The surface properties of the QDs and QD-Her were characterized by Fourier transform infrared (FT-IR) spectroscopy, electron spectroscopy for chemical analysis (ESCA), UV-Vis spectrometry, dynamic light scattering(DLS), and zeta potential measurements. To evaluate thecell compatibility and cytotoxicity of the QDs and QD-Her, human breast cancer cells (SK-BR3) were cultured in the presence of Q-dots. The intracellular uptake of QD-Her to the cells was also observed by confocal laser scanning microscopy (CLSM).

MATERIALS AND METHODS

Trioctyl phosphine oxide (TOPO), trioctyl phosphine (TOP), and hexadecylamine (HDA) were purchased from Sigma-Aldrich Co., USA. DSPE-PEG 2000 {1,2-distearoyl-sn-glycero-3-phosphoethanolamine-N-[carboxy(polyethylene glycol)-2000]} and PEG-2-PE {1,2-palmitoyl-sn-glycero-3-phosphoethanolamine-N-[methoxy(polyethylene glycol)-2000]} were purchased from Avanti Polar Lipids, USA. Herceptin was obtained from Roche Pharma Ltd. (Basel, Switzerland). Cell culture reagents, fetal bovine serum (FBS), Dulbecco's modified eagle medium (DMEM, high glucose), penicillin-streptomycin, trypsin/EDTA, and Dulbecco's phosphate buffer saline (PBS) were supplied by Gibco BRL (Carlsbad, CA), and the SK-BR3 cells (breast cancer cells) were purchased from Korean Cell Line Bank.

Synthesis of CdSe/ZnS Core/Shell QDs. The synthesis of CdSe/ZnS quantum dots was performed using recently reported methods [27, 35]. A mixture of 9 mmol of trioctylphosphine oxide (TOPO), 7 mmol of tetradecyl phosphonic acid (TDPA), and 0.2 g of cadmium oxide (CdO) was heated to 240° C for 20 minutes to obtain a clear solution. A solution containing 0.01 g of Se powder dissolved in 5 mmol of trioctylphosphine (TOP) was injected quickly into the hot solution, and the reaction mixture was allowed to cool to 100∘C for the growth of CdSe nanocrystals. To obtain the CdSe/ZnS nanoparticles, the solution was cooled to room temperature and highly luminescent CdSe nanocrystals were isolated and purified by centrifugation followed by precipitation with methanol and finally dissolved in 5 mL of toluene. To obtain the CdSe/ZnS core-shell quantum dots, the precipitated CdSe nanocrystals were dispersed in 2 mL of TOP in a three-necked ask. In addition, ZnS (0.092 g) was dissolved in 2 mmol

TOP upon gentle heating. After cooling to room temperature, the resulting mixture was injected dropwise into a reaction flask containing the core nanocrystal at 140° C for 6 hrs. After the addition was complete, the particles were annealed at 90∘C for 6 hrs. Core-shell quantum dots of various sizes were obtained by adjusting the concentration of CdO and ZnS in TOP, as well as the corresponding injection periods. The prepared CdSe/ZnS QDs were dissolved in chloroform and purified further by centrifugation and double reprecipitation from methanol.

Preparation of Hydrophilic CdSe/ZnS QDs. DSPE-PEG and PEG-2 PE (2 : 8) were dissolved in 5 mL of chloroform (CHCl3) and 1 mL of the mixture was transferred to a 250 mL three neck round-bottom ask containing CdSe/ZnS QDs in 5 mL of chloroform. The clear solution was stirred overnight under nitrogen. When the reaction was complete, the chloroform was removed by vacuum, and the residue was mixed with 4 mL of water and transferred to a centrifuge tube. Subsequently, 40 mL of water was added to the mixed solution, and the precipitated product was separated by centrifugation (3,000 rpm for 15 min) and washed with water. The precipitated product was dissolved in 10 mL of methanol, and water was then added to ensure that polymer-coated QDs were suspended.

Immobilization of Herceptin on the Surface of CdSe/ZnS QDs. The immobilization of herceptin on CdSe/ZnS (QD-Her) was carried out by a reaction of water-soluble QDs with herceptin, as shown in Figure 1. Water soluble QDs (18 mg/mL) and herceptin (108 mg/mL) were added to a two-necked round-bottom ask and dissolved in 10 mL of PBS buffer (pH 6.0). EDC (1 mmol) and NHS (1 mmol) were added to the reaction solution followed by stirring for 5 hrs at room temperature. The reaction

solution was filtered to remove the precipitate and then added to a dialysis membrane (MWCO: 100,000) in deionized water media for 24 h to remove the unreacted EDC, NHS, and herceptin. Finally, the solution was filtered through a 0.45 m membrane and dried for 24 hrs under vacuum.

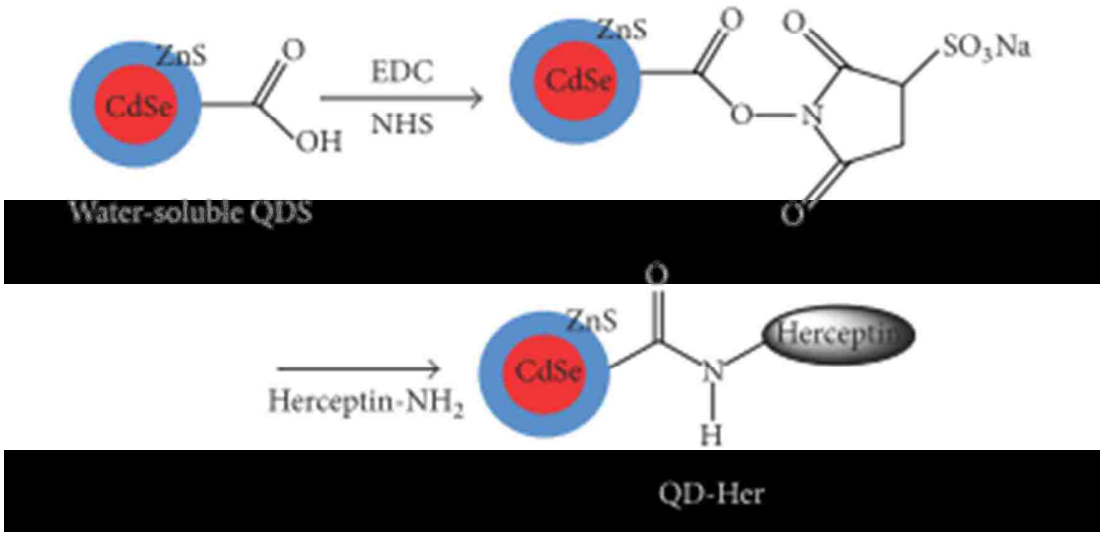

Figure 1. Schematic diagram showing the immobilization of herceptin on the CdSe/ZnS core-shell quantum dots (QD-Her).

RESULTS

Physical Characterization. Quantum dot nanoparticles were ground with KBr powder, compressed into pellets, and examined by FTIR (Jasco FTIR 300 E spectrometer) spectroscopy with a resolution of 4 cm^{-1}. Transmission electron microscopy (TEM, Philips, CM 200 TEM, applied operation voltage; 120 kV) was used

to observe the morphology of the nanoparticles. To obtain the samples for the TEM observations, the particles were diluted with distilled water and deposited on Formvar coated 400 mesh copper grids. After drying the nanoparticle-fluid thin film on the copper grid, a thin carbon film, approximately 10–30 nm in thickness, was deposited on the nanoparticles fluid film. The hydrodynamic diameter and size distribution of the quantum dots were determined by dynamic light scattering (DLS) using a standard laboratory built light scattering spectrometer using a BI90 particle sizer (Brookhaven Instruments Corp., Holtsville, NY). The system had a vertically polarized incident light of 514.5 nm supplied by an argon ion laser (Lexel laser, model 95). The UV-Vis absorption spectrum was recorded from aqueous dispersions at room temperature using a Hitachi U-3000 spectrophotometer.

Cell Culture. SK-BR3 (breast cancer cells) was used as the target cell, and KB (epithelial cancer cells) was used as the control cell line. The cells were cultured routinely at 37º C in a humidified atmosphere containing 5% CO2 in a polystyrene dish containing 10 mL of McCOY medium or DMEM medium, supplemented with 10% fetal bovine serum and 1% penicillin streptomycin G sodium (PGS). The medium was changed every third day. For subculture, the cells were washed twice with PBS and incubated with a trypsin-EDTA solution (0.25% trypsin, 1 mM EDTA) for 10 min at 37∘C to detach the cells. Complete media were then added to the polystyrene dish at room temperature to inhibit the effects of trypsin. The cells were washed twice by centrifugation and resuspended in complete media for reseeding and growing in new culture asks. To observe the morphology of cells, the cells were seeded at a concentration of 1 × 105/mL in a 10 mL Petri dish and incubated for 3 days with QDs-or

QD-Her-containing media at a concentration of 0.2 mg/mL. The morphology of adhered cells was observed by optical microscopy (Nikon Eclipse TS100, Japan).

To examine the cellular uptake of nanoparticles via fluorescence microscope and confocal laser microscope, the cells were seeded at a concentration of 1×10^5 /mL in a 10 mL Petri dish and incubated for 1 day. After 1 day, the medium was replaced with QDs and QD-Her-containing media at a particle concentration of 50 g/mL and incubated for certain time (1–6 hrs) for the internalization of the nanoparticles into the cells. The cells were then washed three times with Dulbecco's PBS (D-PBS) and images were taken using fluorescence and confocal laser microscopes. The fluorescence images were obtained using an Olympus IX70 fluorescence microscope equipped with a cooled charge-coupled device (CCD) camera. The images were processed using DVC view so ware (version 2.2.8, DVC Company). A Zeiss LSM 410 confocal laser scanning microscope (Brightness:700 cd/mm2, Zeiss, Oberkochen, Germany) was used to obtain the confocal images. e position and integrity of the internalized QD-Her conjugates were evaluated by confocal microscopy using 4,6-diamidine-2-phenylindole dihydrochloride (DAPI, blue) as a marker, which stains the nuclei of the cells. The cell nuclei were stained by the addition of DAPI solution (10 L) with proper mixing and incubated for 10 min. To track the QD-Her nanoparticles, herceptin conjugated QDs and DAPI (488 nm) were added to the cells. The stained cells were washed at least three times with 1 mL of fresh McCoy medium and images were then taken by confocal laser microscopy [37].

The comparative proliferation of SK-BR3 and KB cells in a medium containing QDs and QD-Her was determined using a MTT (3-{4,5-dimethylthiazol-2yl}-2,5-

diphenyltetrazolium bromide) assay. Briefly, the SK-BR3 and KB cells were seeded separately (1 × 105 cell/mL) on 24 well plates in the presence of a cell culture medium. A er 24 h, the culture medium was replaced with fresh medium containing QDs and QD-Her at a particle concentration of 200 μg/mL. After incubation for 1, 2, and 3 days, a 50 μL MTT solution (5 mg/mL in PBS) was added to each well and incubated in a humidified atmosphere of 5% CO2 at 37∘C for 4 h. After removing the medium, the converted dye was dissolved in acidic isopropanol (0.04 N HCl-isopropanol) and kept for 30 min in the dark at room temperature. From each sample, the medium (100 μL) was taken, transferred to a 96-well plate, and subjected to the ultraviolet measurements of the converted dye. This was achieved at a wavelength of 570 nm on a kinetic microplate reader. The experiment was repeated at least three times.

The phase contrast and fluorescence images of the cells were obtained using a combined explorer system with a motorized inverted fluorescence microscope (Carl Zeiss LSM700, Germany), using the topographic images that can be detected simultaneously. The cell proliferation experiment was performed in triplicate and the results were expressed as mean ± standard deviation (SD). Student's t-test was used to assess the statistical significant differences in the results. A P value <0.05 was considered significant.

DISCUSSIONS

Surface Characterization of Herceptin-Immobilized QDs The surface modification of QDs with herceptin was confirmed by FTIR, as shown in Figure 2. In the case of the QDs spectrum, the introduction of DSPE-PEG 2000 to the surface of the QDs was confirmed by observing the characteristic peaks at 1700 and 3500 cm^{-1}, as shown in

Figure 2(a), which was attributed to free carboxyl (–COOH) and hydroxyl (–OH) groups [38, 39]. Again, after the reaction of the QDs with herceptin, two new peaks at positions approximately 1648 cm^{-1} and 1540 cm^{-1} were observed in the spectrum of QD-Her (Figure 2(b)), which were assigned to amide I (–CO–NH–) and amide II (–CO–NH–) bonds, respectively, indicating the successful immobilization of herceptin on the surface of the QDs [29, 32].

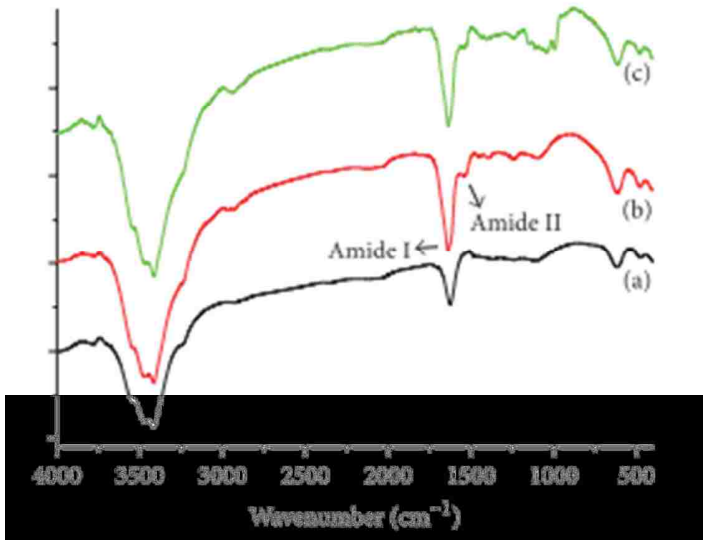

Figure 2. FT-IR spectra of the QDs (a), QD-Her (b), and Herceptin (c) measured using the KBr method.

In figures 3, (a) and (b) present TEM images of the QDs and QD-Her, respectively. The QDs have a spherical morphology with a mean diameter of ~4.1 nm. Because of the small dimensions and high surface energy of the particles, it was easy for

them to aggregate, as seen in Figure 3(a). On the other hand, in the case of QD-Her, the particles had a mean diameter of 4.5 nm, were spherical in shape, and showed significantly less aggregation (Figure 3(b)). The larger particle size and non-aggregated particles morphology was attributed to the conjugation of herceptin on the surface of the QDs.

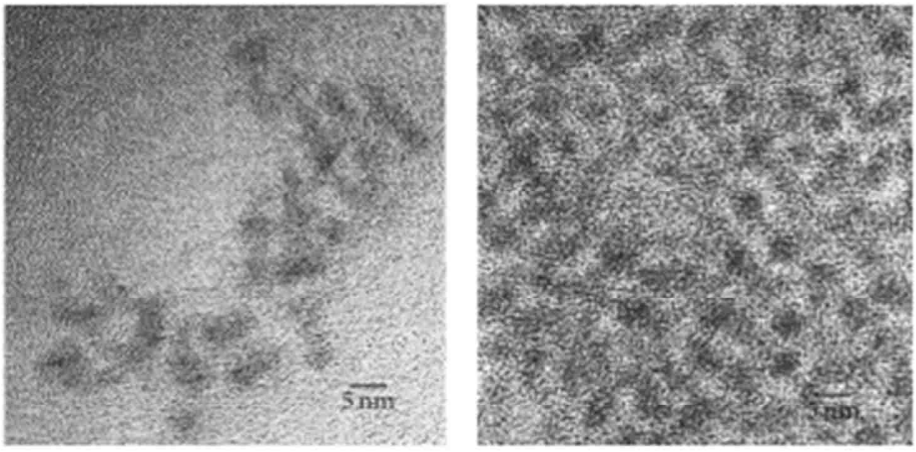

Figure 3. TEM images of the QDs (a) and QD-Her (b).

Figure 4 shows the typical size and size distribution of the synthesized QDs (Figure 4(a)) and QD-Her (Figure 4(b)) measured by DLS. The mean size of the QDs as determined by DLS was ～28 nm. On the other hand, the mean size of the QD-Her was approximately 86 nm. The particle size, as determined by DLS, was considerably larger

than that determined by TEM. This is because the DLS technique measures the mean hydrodynamic diameter of the QDs core surrounded by the organic and solvation layers, and this hydrodynamic diameter is affected by the viscosity and concentration of the solution. TEM, however, gives the diameter of the core alone [29].

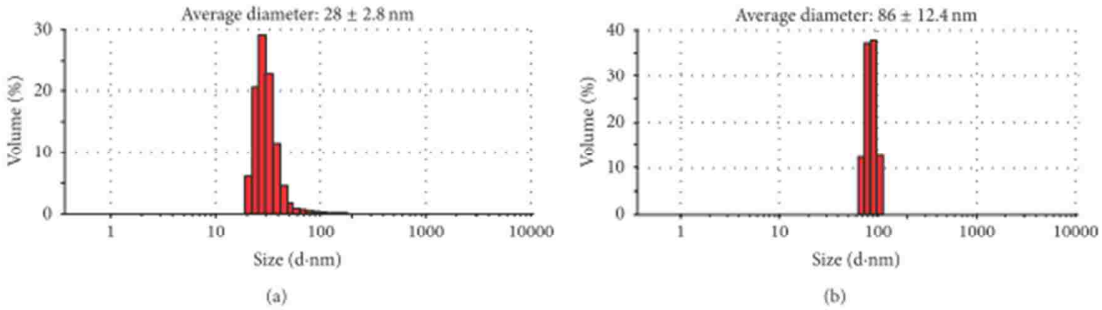

Figure 4. Particle size distribution of the QDs (a) and QD-Her (b) measured by dynamic light scattering (DLS).

The synthesis of CdSe/ZnS core-shell QDs and herceptin-immobilized QDs was also confirmed by UV-Vis absorption spectroscopy, as shown in Figure 5. The QDs showed an absorption onset at 526 nm (Figure 5(a)) and after herceptin immobilization, it exhibited a red shift to 529 nm [31]. This red shift was caused by strong quantum confinement due to the increase in particle size. In addition, the peak at 529 nm attributed to the herceptin labels on the surface of QDs, because of metal to ligand charge transfer [34].

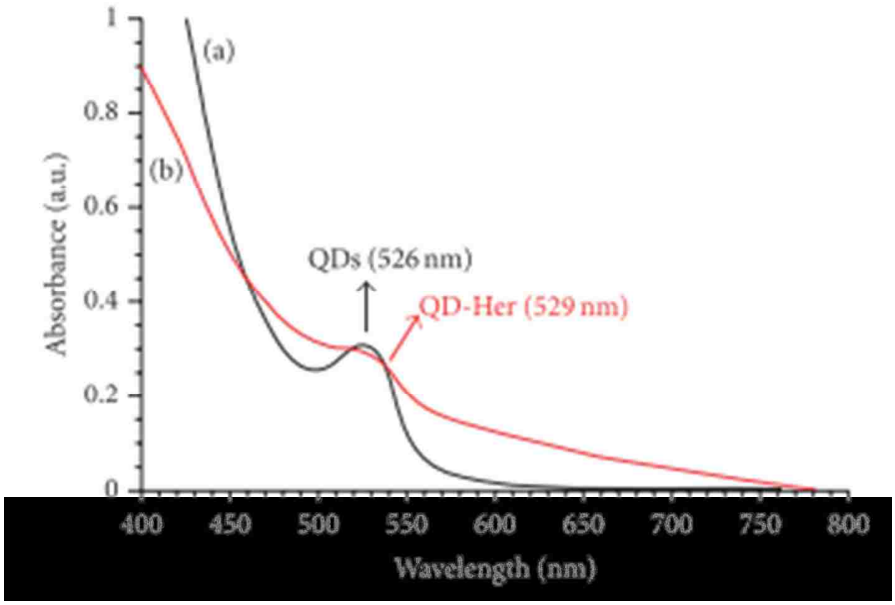

Figure 5. UV-Vis absorption spectra of the QDs (a) and QD-Her (b) in aqueous solution.

The immobilization of herceptin on the surface of QDs was confirmed by ESCA, as shown in Figure 6. The QDs showed peaks for five elements corresponding to C1s (binding energy, 284.0 eV) and O1s (binding energy, 526.5 eV), P2s, 2p (binding energy, 197.0 eV, 132 eV), and N1s (binding energy, 397.0 eV), as shown in Figure 6(a). On the other hand, after herceptin immobilization, the QD-Her showed three typical peaks corresponding to C1s, O1s, and N1s. Table 6.1 lists the chemical compositions of the QDs and QD-Her, which were calculated from the ESCA survey scan spectra. In the case of the QD-Her, the carbon content (73.1%) was higher than in the QDs (69.3%).

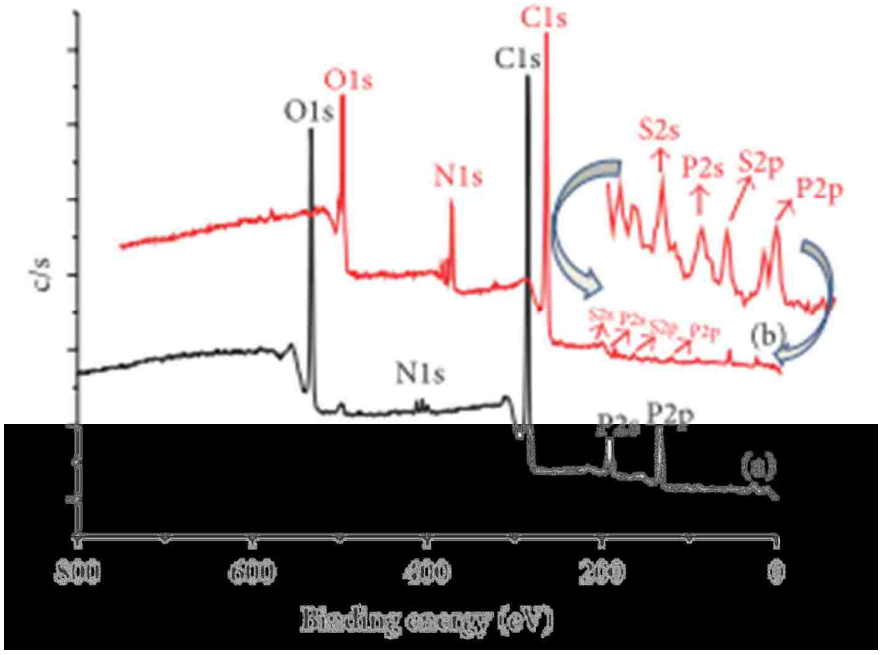

Figure 6. ESCA survey scan spectra of the QDs (a) and QD-Her (b).

Table 1. Atomic percentage of QDs and QD-Her calculated from the ESCA survey scan spectra.

Substrates	Atomic (%)			
	C	O	N	P
QDs	69.3	24.0	0.7	6.0
QD-Her	73.1	15.5	10.5	0.5

Furthermore, one new element, sulfur (0.4%), was observed on the surfaces of the QD-Her, and in the case of QD-Her, the nitrogen content increased from 0.7% to 10.5%,

indicating the successful immobilization of herceptin on the surface of the QDs. One possible explanation for the reduction in the P2s, 2p, and S2p peaks is the photoelectrons with energy loss and the increase in the binding energy during immobilization with herceptin [40].

Evaluation of Cytotoxicity. Figure 7 shows the status of the "Live/Dead" dye-stained SK-BR3 and KB cell cultured in the presence of QDs and QD-Her for 1 and 3 days of incubation. Using this qualitative method, the living and dead cells were stained in green and red under the fluorescence microscope, respectively. Figure 7 shows that all the KB cells remained viable after 3 days of incubation, irrespective of the presence or absence of nanoparticles. On the other hand, after a culture of 1 and 3 days, in the presence of QD-Her, most of the SK-BR3 cells had died, as shown in Figures 8, (e) and 8(f). On the other hand, most of the SK-BR3 cells remained viable in the presence of the QDs and in the polystyrene culture dish (Figures 7(a)–(d)), but a insignificant number of cells were dead in the QD-Her case. A possible explanation of this large decrease in cell viability in the case of QD-Her is that intracellularly delivered herceptin exhibits acute apoptotic activity by interacting with several transcription factors related to cell proliferation [39]. Previously, Bae et al. reported that degradable heparin nanogels and heparin/chitosan polyelectrolyte nanocomplexes could effectively induce apoptosis via receptor-mediated endocytosis through specific herceptin-HER2 integrin interaction [39].

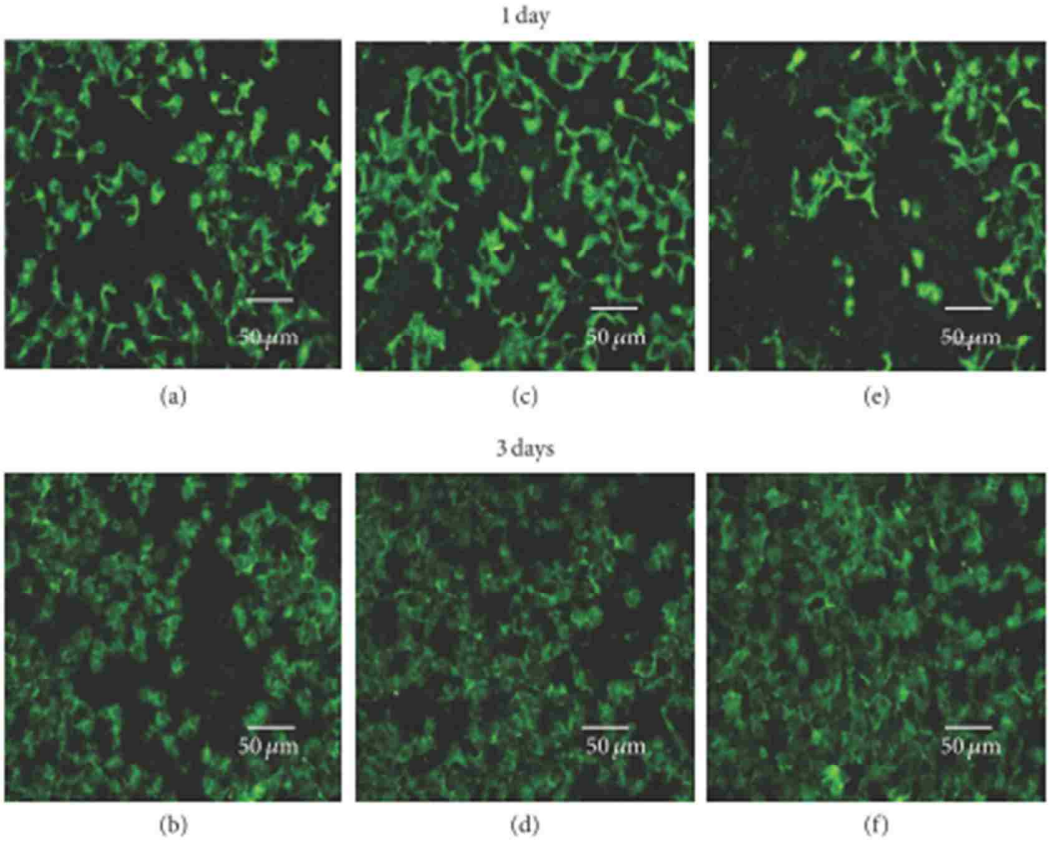

Figure 7. Fluorescence microscopy images of live and dead KB cells after culturing for 1 and 3 days in a polystyrene culture dish ((a), (b)) and in the presence of QDs ((b), (d)) and QD-Her ((e), (f)). The live and dead cells were stained and visualized in green and red, respectively, under a fluorescence microscope.

The endocytosed QD-Her within the cells would release free herceptin molecules in the cytoplasm by cleaving the QD-herceptin linkage under the reductive intracellular environment, which has 300 times higher glutathione (GSH) concentration (20 Mm) than the extracellular level [41]. GSH is the most abundant reducing agent in the cytoplasm, facilitating the detachment of herceptin from the QDs by breaking the PEG-herceptin linkage. In addition, nanoparticles are taken up by the cells through endocytosis, which

disrupts the cell membrane [32], or weak cell adhesive interactions with QDs promote apoptosis (programmed cell death). The core-shell nanoparticles conjugated with herceptin may act as cellular markers and target the receptors expressed on the cell surface with cellular internalization. The receptors are highly regulated by the cell surface proteins [37], which mediate the specific interactions between the cells and their extracellular milieu, and they are generally localized on the plasma membrane [33]. This suggests that the cytotoxicity of QDs was improved by the conjugation of DSPE-PEG and PEG-2-PE (Figures 7(c), (d)) and herceptin (Figures 7(e), (f)), as determined by the viability of KB cells (see Figure 7).

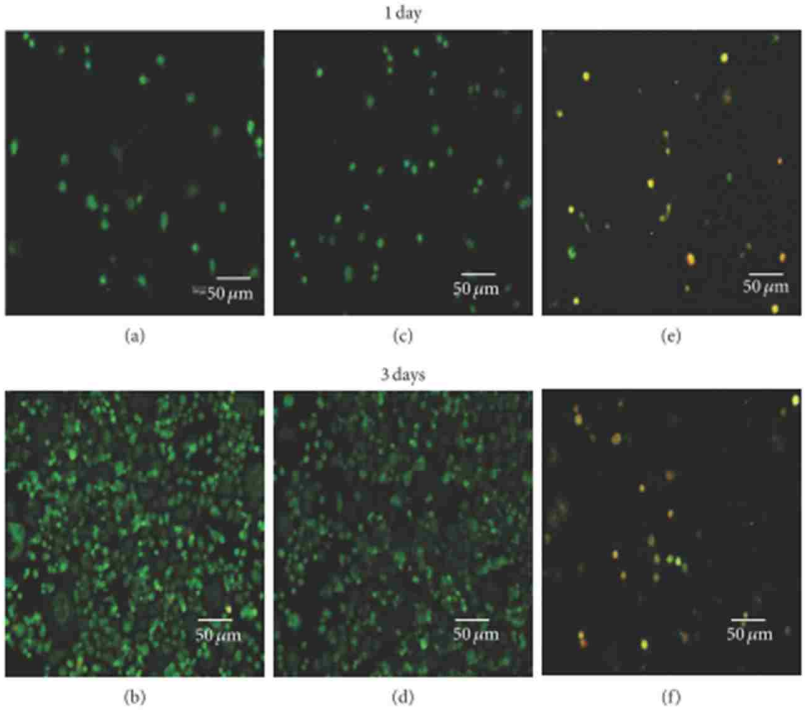

Figure 8. Fluorescence microscopy image of the live and dead SK-BR3 cells after culturing for 1 and 3 days in a polystyrene culture dish ((a), (b)) and in the presence of QDs ((b), (d)) and QD-Her ((e), (f)). Live and dead cells were stained in green and red, respectively, under a fluorescence microscope.

Figure 9 shows the viability of SK-BR3 cells cultured for 1 and 3 days in the presence of QD-Her, as determined by the MTT assay. After 1 and 3 days of incubation, the level of SK-BR3 cell proliferation in the presence of QDs was similar to that of the cells cultured in the absence of nanoparticles (PS culture dish). On the other hand, cell proliferation in the presence of QD-Her was significantly lower than that of the QDs. Therefore, the CdSe/ZnS quantum dots conjugated with herceptin could increase the death of SK-BR3 cells considerably compared to the CdSe/ZnS quantum dots without herceptin.

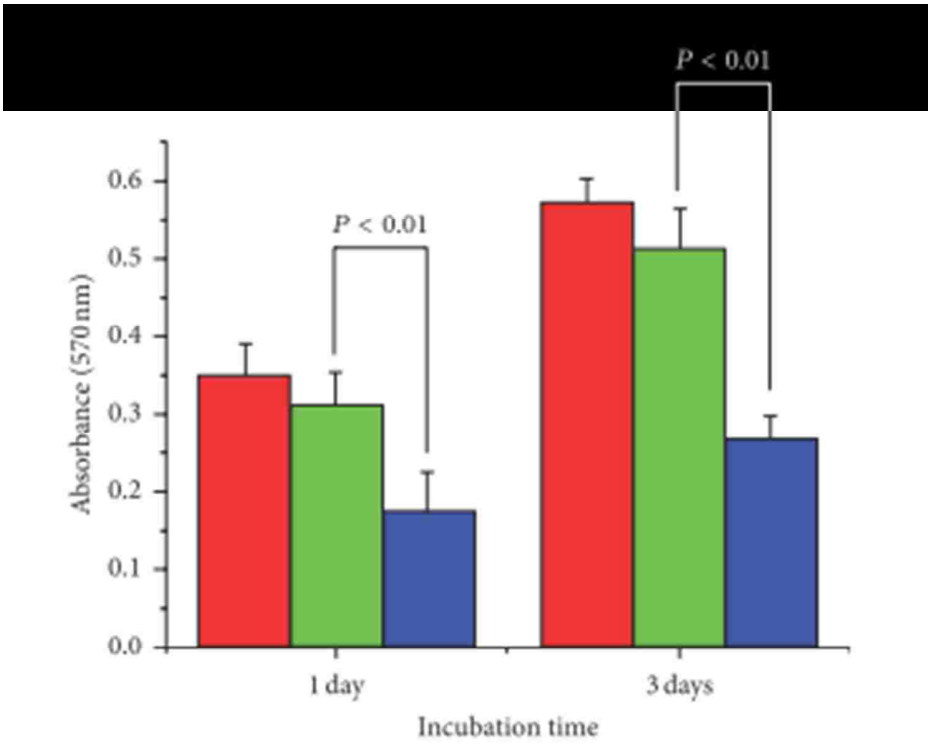

Figure 9. MTT assay, absorbance as a measure of the cell proliferation of SK-BR3 cells cultured in the PS culture dish (the red bar), in the presence of QDs (the green bar) and QD-Her (the blue bar) for different time.

Evaluation of Intracellular Uptake. The uptake of QD-Her into the target cells was visualized by fluorescence microscopy. Figure 10 shows fluorescence images obtained from the cultured SK-BR3 cells that had been incubated for up to 6 hrs in the presence QD-Her. During the cell culture in the presence of QD-Her, a significant number of nanoparticles were transported into the cells and emitted intense fluorescence. This suggests that the QDs carrying herceptin provide specific recognition signals for the nanoparticles to facilitate internalization into the target cells (SK-BR3 cells).

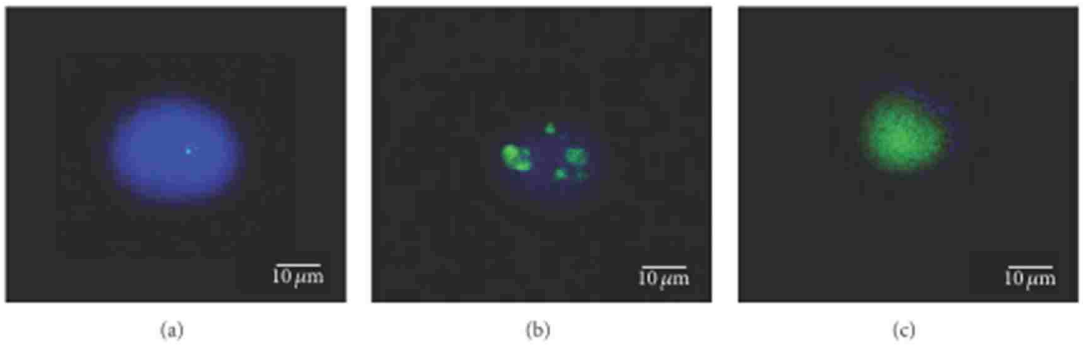

Figure 10. Fluorescence images obtained from the culture of SK-BR3 cells for 1, 3, and 6 hrs in the presence of DAPI and QD-Her.

The interaction of the herceptin from the QDs with the HER-2 receptors expressed on the membrane surface of the SK-BR3 cells might have contributed to the improvement in the internalization of QD-Her into the cells, based on receptor-mediated endocytosis [29]. Gan et al. reported similar results [42]. They introduced a hepatocarcinoma binding peptide (A54) onto the surface of the magnetite nanoparticles

and examined their interaction with hepatocellular carcinoma cells in vitro by fluorescence microscopy. Internalization of the herceptin-conjugated nanoparticles (QD-Her) into SK-BR3 occurred. Breast cancer cells expressing HER-2 receptor were quite sensitive to herceptin. Figure 6.10 shows that herceptin is an effective antibody, binding specifically to the HER-2 receptor-bearing breast cancer cells. The internalization of QD-Her into SK-BR3 cells was confirmed by confocal laser microscopy to characterize the delivery of QD-Her to the cytoplasm of the SK-BR3 cells. Figure 6.10 shows the fluorescence image derived from the nucleus of the SK-BR3 cells (DAPI, blue) and QD-Her internalized (green). The cells were cultured in the presence of QD-Her at various incubation times (Figure 10). Weak QD-Her conjugates were observed in the fluorescence image (green color) after 1 hr (Figure 6.10(a)) and slightly higher fluorescence image was observed after 3 hrs (Figure 6.10(b)). Intense fluorescence image was noted after 6 hrs (Figure 10(c)). On the other hand, the blue fluorescence image derived from the nuclei stained with DAPI was strong after 1 hr incubation but it decreased with increasing incubation time and almost disappeared after 6 hrs incubation. In particular, the interaction of SK-BR3 with QD-Her began after 1 hr incubation and was accelerated and saturated after 6 hrs. The confocal microscopy images suggest that the nanoparticle-mediated delivery of monoclonal antibodies was achieved efficiently, resulting in cell death. The mechanism of internalization involves endocytosis followed by the release of herceptin-conjugated nanoparticles to the cytoplasm [37]. This suggests that the growth signal of breast cancer cells is inhibited completely by the specific binding of the herceptin to the Her-2 receptor of SK-BR3 membrane, resulting in cell death [38].

CONCLUSIONS

DSPE-PEG-coated CdSe/ZnS core-shell quantum dots (QDs) were conjugated successfully with the herceptin antibody. Herceptin immobilized QDs (QD-Her) were confirmed by FTIR and XPS. The QD-Her size determined by DLS was ~86 nm. The QD-Her had no cytotoxicity on the control cells (KB) compared to the target cells (SK-BR3). QD-Her was internalized selectively into the target cells (SK-BR3), and free herceptin was released in the cytoplasm, which induced acute apoptosis. The QD-Her nanoparticles were endocytosed by breast cancer cells (SK-BR3) to a large extent via a receptor-mediated mechanism, where herceptin conjugated on the nanoparticles targets the HER-2 receptor expressed on the membrane of the cancer cells [39]. Therefore, QD-Her has a potential use in optical imaging and the treatment of breast cancer cells.

ACKNOWLEDGEMENTS

This study was supported by the Basic Research Laboratory Program (no. 2011-0020264) and the General Research Program (2013 RIA 2005148) from the Ministry of Education, Science and Technology of Korea.

REFERENCES

[1] J. Pan, Y. Wang, and S.-S. Feng, “Formulation, characterization, and in vitro evaluation of quantum dots loaded in poly(Lactide)-Vitamin E TPGS nanoparticles for cellular and molecular imaging,” Biotechnology and Bioengineering, vol. 101, no. 3, pp. 622–633, 2008.

[2] F. Pinaud, X. Michalet, L. A. Bentolila et al., “Advances in fluorescence imaging with quantum dot bio-probes,” Biomaterials, vol. 27, no. 9, pp. 1679–1687, 2006.

[3] J. Pan and S.-S. Feng, "Targeting and imaging cancer cells by Folate-decorated, quantum dots (QDs)-loaded nanoparticles of biodegradable polymers," Biomaterials, vol. 30, no. 6, pp. 1176–1183, 2009.

[4] K. S. Soppimath, T. M. Aminabhavi, A. R. Kulkarni, and W. E. Rudzinski, "Biodegradable polymeric nanoparticles as drug delivery devices," Journal of Controlled Release, vol. 70, no. 1-2, pp. 1679–1687, 2001.

[5] T. Jamieson, R. Bakhshi, D. Petrova, R. Pocock, M. Imani, and A. M. Seifalian, "Biological applications of quantum dots," Biomaterials, vol. 28, no. 31, pp. 4717–4732, 2007.

[6] A. P. Alivisatos, W. Gu, and C. Larabell, "Quantum dots as cellular probes," Annual Review of Biomedical Engineering, vol. 7, pp. 55–76, 2005.

[7] X. Michalet, F. F. Pinaud, L. A. Bentolila et al., "Quantum dots for live cells, in vivo imaging, and diagnostics," Science, vol. 307, no. 5709, pp. 538–544, 2005.

[8] A. M. Derfus, W. C. W. Chan, and S. N. Bhatia, "Probing the cytotoxicity of semiconductor quantum dots," Nano Letters, vol. 4, no. 1, pp. 11–18, 2004.

[9] E. T. Ben-Ari, "Nanoscale quantum dots hold promise for cancer applications," Journal of the National Cancer Institute, vol. 95, no. 7, pp. 502–504, 2003.

[10] H. Mattoussi, J. Matthew Mauro, E. R. Goldman et al., "Self-assembly of CdSe-ZnS quantum dot bioconjugates using an engineered recombinant protein," Journal of the American Chemical Society, vol. 122, no. 49, pp. 12142–12150, 2000.

[11] A. M. Smith, H. Duan, A. M. Mohs, and S. Nie, "Bioconjugated quantum dots for in vivo molecular and cellular imaging," Advanced Drug Delivery Reviews, vol. 60, no. 11, pp. 1226–1240, 2008.

[12] M. T. Fern´andez-Arguelles, A. Yakovlev, R. A. Sperling et al., "Synthesis and characterization of polymer-coated quantum dots with integrated acceptor dyes as FRET-based nanoprobes," Nano Letters, vol. 7, no. 9, pp. 2613–2617, 2007.

[13] Z. Chen, H. Chen, H. Meng et al., "Bio-distribution and metabolic paths of silica coated CdSeS quantum dots," Toxicology and Applied Pharmacology, vol. 230, no. 3, pp. 364–371, 2008.

[14] J. G. Rouse, C. M. Haslauer, E. G. Loboa, and N. A. Monteiro-Riviere, "Cyclic tensile strain increases interactions between human epidermal keratinocytes and quantum dot nanoparticles," Toxicology In Vitro, vol. 22, no. 2, pp. 491–497, 2008.

[15] W. C. Chan, D. J. Maxwell, X. Gao, R. E. Bailey, M. Han, and S. Nie, "Luminescent quantum dots for multiplexed biological detection and imaging," Current Opinion in Biotechnology, vol. 13, no. 2, pp. 40–47, 2002.

[16] H. M. Chen, X. F. Huang, L. Xu, J. Xu, K. J. Chen, and D. Feng, "Surface-defect-states photoluminescence in CdS nanocrystals prepared by one-step aqueous synthesis method," Superletter Microstructure, vol. 27, no. 3, pp. 1–5, 2000.

[17] X. Gao, W. C. W. Chan, and S. Nie, "Quantum-dot nanocrystals for ultrasensitive biological labeling and multicolor optical encoding," Journal of Biomedical Optics, vol. 7, no. 4, pp. 532–537, 2002.

[18] C.-C. Chen, C.-P. Yet, H.-N. Wang, and C.-Y. Chao, "Self-assembly of monolayers of cadmium selenide nanocrystals with dual color emission," Langmuir, vol. 15, no. 20, pp. 6845–6850, 1999.

[19] F. Chen and D. Gerion, “Fluorescent CdSe/ZnS nanocrystal-peptide conjugates for long-term, nontoxic imaging and nuclear targeting in living cells,” Nano Letters, vol. 4, no. 10, pp. 1827–1832, 2004.

[20] M. Bruchez Jr., M. Moronne, P. Gin, S. Weiss, and A. P. Alivisatos, “Semiconductor nanocrystals as fluorescent biological labels,” Science, vol. 281, no. 5385, pp. 2013–2016, 1998.

[21] W. C. W. Chan, D. J. Maxwell, X. Gao, R. E. Bailey, M. Han, and S. Nie, “Luminescent quantum dots for multiplexed biological detection and imaging,” Current Opinion in Biotechnology, vol. 13, no. 1, pp. 40–46, 2002.

[22] F. Pinaud, D. King, H.-P. Moore, and S. Weiss, “Bioactivation and cell targeting of semiconductor CdSe/ZnS nanocrystals with phytochelatin-related peptides,” Journal of the American Chemical Society, vol. 126, no. 19, pp. 6115–6123, 2004.

[23] K.-I. Hanaki, A. Momo, T. Oku et al., “Semiconductor quantum dot/albumin complex is a long-life and highly photostable endosome marker,” Biochemical and Biophysical Research Communications, vol. 302, no. 3, pp. 496–501, 2003.

[24] W. C. W. Chan and S. Nie, “Quantum dot bioconjugates for ultrasensitive nonisotopic detection,” Science, vol. 281, no. 5385, pp. 2016–2018, 1998.

[25] E. R. Goldman, G. P. Anderson, P. T. Tran, H. Mattoussi, P. T. Charles, and J. M. Mauro, “Conjugation of luminescent quantum dots with antibodies using an engineered adaptor protein to provide new reagents for fluoroimmunoassays,” Analytical Chemistry, vol. 74, no. 4, pp. 841–847, 2002.

[26] D. Gerion, W. J. Parak, S. C. Williams, D. Zanchet, C. M. Micheel, and A. P. Alivisatos, “Sorting fluorescent nanocrystals with DNA,” Journal of the American Chemical Society, vol. 124, no. 24, pp. 7070–7074, 2002.

[27] M. Nurunnabi, K. J. Cho, J. S. Choi, K. M. Huh, and Y.-K. Lee, “Targeted near-IR QDs-loaded micelles for cancer therapy and imaging,” Biomaterials, vol. 31, no. 20, pp. 5436–5444, 2010.

[28] Y.-K. Lee, S. M. Hong, J. S. Kim et al., “Encapsulation of CdSe/ZnS quantum dots in poly(ethylene glycol)-poly(D,L-lactide) micelle for biomedical imaging and detection,” Macromolecular Research, vol. 15, no. 4, pp. 330–336, 2007.

[29] Z.-C. Xing, M.-J. Park, S.-J. Han et al., “Intracellular uptake of magnetite nanoparticles conjugated with RGDS-peptide,” Macromolecular Research, vol. 19, no. 9, pp. 897–903, 2011.

[30] Y. L. Wu, C. S. Lim, S. Fu et al., “Surface modifications of ZnO quantum dots for bio-imaging,” Nanotechnology, vol. 18, no. 21, Article ID 215604, 2007.

[31] Y. Zhang, N. Kohler, and M. Zhang, “Surface modification of superparamagnetic magnetite nanoparticles and their intracellular uptake,” Biomaterials, vol. 23, no. 7, pp. 1553–1561, 2002.

[32] K. M. K. Selim, Z.-C. Xing, M.-J. Choi, Y. Chang, H. Guo, and I.-K. Kang, “Reduced cytotoxicity of insulin-immobilized CdS quantum dots using PEG as a spacer,” Nanoscale Research Letters, vol. 6, article 528, pp. 1–9, 2011.

[33] A. K. Gupta and M. Gupta, “Cytotoxicity suppression and cellular uptake enhancement of surface modified magnetic nanoparticles,” Biomaterials, vol. 26, no. 13, pp. 1565–1573, 2005.

[34] M. Yamaura, R. L. Camilo, L. C. Sampaio, M. A. Macˆedo, M. Nakamura, and H. E. Toma, “Preparation and characterization of (3-aminopropyl)triethoxysilane-coated magnetite nanoparticles,” Journal of Magnetism and Magnetic Materials, vol. 279, no. 2-3, pp. 210–217, 2004.

[35] M. Protiere and P. Reiss, “Highly luminescent Cd–ZnSe/ZnS Core/Shell nanocrystal emitting in the blue-green spectral range,” Small, vol. 3, no. 3, pp. 468–473, 2007.

[36] W. B. Tan and Y. Zhang, “Multifunctional quantum-dot-based magnetic chitosan nanobeads,” Advanced Materials, vol. 17, no. 19, pp. 2375–2380, 2005.

[37] S. S. Bale, S. J. Kwon, D. A. Shah, A. Banerjee, J. S. Dordick, and R. S. Kane, “Nanoparticle-mediated cytoplasmic delivery of proteins to target cellular machinery,” ACS Nano, vol. 4, no. 3, pp. 1493–1500, 2010.

[38] K. H. Bae, H. Mok, and T. G. Park, “Synthesis, characterization, and intracellular delivery of reducible heparin nanogels for apoptotic cell death,” Biomaterials, vol. 29, no. 23, pp. 3376–3383, 2008.

[39] K. H. Bae, C. W. Moon, Y. Lee, and T. G. Park, “Intracellular delivery of heparin complexed with chitosan-g-poly(ethylene glycol) for inducing apoptosis,” Pharmaceutical Research, vol. 26, no. 1, pp. 93–100, 2009.

[40] P. F. Gomes, M. P. F. Godoy, A. B. Veloso et al., “Exciton binding energy in type II quantum dots,” Physica Status Solidi B, vol. 4, no. 2, pp. 385–388, 2007.

[41] R. Hong, G. Han, J. M. Fern´andez, B.-J. Kim, N. S. Forbes, and V. M. Rotello, "Glutathione-mediated delivery and release using monolayer protected nanoparticle carriers," Journal of the American Chemical Society, vol. 128, no. 4, pp. 1078–1079, 2006.

[42] Z.-F. Gan, J.-S. Jiang, and Y. Yang, "Immobilization of homing peptide on magnetite nanoparticles and its specicity in vitro," Journal of Biomedical Materials Research A, vol. 27, no. 1, pp. 468–476, 2008.

SECTION

2. EXECUTIVE SUMMARY

1. QPbS is used as an efficient photosensitizer in polymeric PR material.

   - Off-resonance approach with an arbitrary choice of QPbS results in easy application of Q-dots in PR materials.

   - The best result of organic PR composite photosensitized with Q-dots η_{int} = 82.7 %, Γ = 211 cm^{-1} and τ_f = 33.9 ± 0.4 ms were obtained.

2. QPbS is used as a charge-carrier material in polymeric PR material in CW condition.

   - Novel composition of PR composite of C_{60}, QPbS, TPD, PVK, and 7-DCST was demonstrated.

   - The fastest response time ever, τ_f = 400 μs, was recorded with any loss of efficiency with η_{int} = 72% and Γ = 500 cm^{-1}.

3. The emission wavelength in tunable water soluble InGaP and InP Q-dots using the thermal synthesis method was investigated.

   - Quantum yield loss of lipidized quantum dot is greatly diminished.

   - Double step etching shows the effective tuning in emission wavelength and improvement of PL intensity.

4. Water soluble InP/ZnS and CdSe/ZnS Q-dots were used as bio-maker to trace cancer cells.

   - Cell viability was optimized in both approaches with SRB colormetric and MTT assay.

   - Water soluble InP/ZnS and CdSe/ZnS Q-dots combined with CPPs and Herceptin showed excellent potential as bio-imaging application.

VITA

Jong-Sik Moon was born in 1976 in Deagu, South Korea. In 1995, he joined department of Polymer Engineering, Kyoungbuk National University, South Korea, and in 2002, he graduated with Bachelor of Engineering in Polymer Engineering. During this period, from 1996 to 1999, he served as a Sergeant in Korea Air Force. He joined the graduated school in the same university in 2002 and graduated with Master of Engineering in 2004. He worked at Tokyo Institute of Technology as a researcher in the same year.

In 2009, Jong-Sik joined Dr. Jeffrey G. Winiarz's research group at Missouri University of Science and Technology, Rolla, Missouri for his PhD in Physical Chemistry. During his time as a graduate student, he worked both as a graduate research assistant and a graduate teaching assistant at the chemistry department. His research was mainly focused on investigating quantum dots as a component of organic PR materials. His PhD in Chemistry was awarded in July, 2014.